Biological Applications of Confocal Fluorescence Polarization Microscopy

by

Chad E. Bigelow

Submitted in Partial Fulfillment
of the
Requirements for the Degree
Doctor of Philosophy

Supervised by
Professor Thomas H. Foster

The Institute of Optics
The College
School of Engineering and Applied Sciences

University of Rochester
Rochester, New York

2005

To Kaylyn and my parents. . .

Curriculum Vitae

Chad Eric Bigelow was born in Traverse City, Michigan, on November 7th, 1974. He graduated from Traverse City Senior High in 1993 where his interest in science was further advanced by two excellent teachers in Mr. Al Garwold and Mr. Keith Forton.

In September of 1993 he enrolled at the University of Michigan where he was eventually destined for the College of Engineering. As an undergraduate he spent a summer in the National Science Foundation's Research Experience for Undergraduates (REU) program with the Center for Ultrafast Optical Science at the University of Michigan. Through that program he joined the laboratory of Professor Philip Bucksbaum where he remained an active member of the group for the remainder of his time in Ann Arbor. In 1997 he graduated Magna cum Laude with a Bachelor of Science in Engineering in Engineering Physics. While at the University of Michigan, a mutual friend and a mutual love for college hockey brought Bigelow and his future wife Kaylyn Makins together.

After graduating from the University of Michigan, Bigelow moved to Rochester, New York in 1998 to attend The Institute of Optics at the University of Rochester. At the end of his first year he decided to pursue his interest

in biomedical optics in the laboratory of Professor Thomas Foster. His work as a graduate student in Rochester focused on new applications for confocal fluorescence polarization microscopy with a particular emphasis on cancer therapy and diagnosis.

Publications

J. D. Wilson, C. E. Bigelow, D. J. Calkins, and T. H. Foster, "Light scattering from intact cells reports oxidative-stress-induced mitochondrial swelling," Biophys. J. (in press)

C. E. Bigelow, H. D. Vishwasrao, J. G. Frelinger, and T. H. Foster, "Imaging enzyme activity with polarization-sensitive confocal fluorescence microscopy," J. Microsc. **215**, 24-33 (2004).

J. M. Bliss, C. E. Bigelow, T. H. Foster, and C. G. Haidaris, "Susceptibility of *Candida* species to photodynamic effects of Photofrin," Antimicrob. Agents Chemother. **48**, 2000-2006 (2004).

C. E. Bigelow, D. L. Conover, and T. H. Foster, "Confocal fluorescence spectroscopy and anisotropy imaging system," Opt. Lett. **28**, 695-697 (2003).

C. E. Bigelow, C. J. Harkrider, D. L. Conover, T. H. Foster, I. Georgakoudi, S. Mitra, M. G. Nichols, and M. Rajadhyaksha, "Retrofitted confocal laser scanner for a commercial inverted fluorescence microscope," Rev. Sci. Instrum. **72**, 3407-3410 (2001).

C. E. Bigelow, S. Mitra, R. Knuechel, and T. H. Foster, "ALA- and ALA-hexylester-induced protoporphyrin IX fluorescence and distribution in multicell tumour spheroids," Br. J. Cancer **85**, 727-734 (2001).

Presentations

C. E. Bigelow and T. H. Foster, "Biological applications of confocal fluorescence anisotropy imaging," presented at the Optical Society of America Frontiers in Optics, Rochester, NY, 10-14 October, 2004.

C. E. Bigelow and T. H. Foster, "Effects of light scattering on fluorescence polarization images in turbid media," presented at the Optical Society of America Frontiers in Optics, Rochester, NY, 10-14 October, 2004.

C. E. Bigelow, J. G. Frelinger, and T. H. Foster, "Enzyme activity imaging with confocal fluorescence polarization microscopy," presented at the Optical Society of America Biomedical Optics Topical Meeting, Miami Beach, FL, 14-17 April, 2004.

J. D. Wilson, C. E. Bigelow, D. J. Calkins, and T. H. Foster, "Early mitochondrial responses to photodynamic therapy are reported by angularly resolved light scattering," presented at the Optical Society of America Biomedical Optics Topical Meeting, Miami Beach, FL, 14-17 April, 2004.

C. E. Bigelow, J. G. Frelinger, and T. H. Foster, "Enzyme activity imaging based on confocal fluorescence anisotropy microscopy," presented at the Engineering Conferences International Advances in Optics for Biotechnology, Medicine and Surgery, Banff, Canada, 3-7 August, 2003.

C. E. Bigelow, D. L. Conover, and T. H. Foster, "A custom laser scanning confocal fluorescence microscope with simultaneous multi-wavelength imaging, spectroscopy and anisotropy capabilities," presented at the American Society for Photobiology 30th Annual Meeting, Quebec City, Canada, 13-17 July, 2002.

C. E. Bigelow, D. L. Conover, and T. H. Foster, "Commercial inverted microscope retrofitted for confocal scanning with multi-wavelength detection, spatially resolved spectroscopy, and fluorescence anisotropy," presented at the Optical Society of America Biomedical Optics Topical Meeting, Miami Beach, FL, 7-10 April, 2002.

C. E. Bigelow, S. Mitra, and T. H. Foster, "Comparison of ALA- and ALA-ester-induced PpIX fluorescence and distribution in multicell tumor spheroids," presented at the 13th International Congress on Photobiology, San Francisco, CA, 1-6 July, 2000.

Acknowledgments

This thesis is the result of several years of work and invaluable assistance from many people to whom I am indebted. Their support and encouragement has made the conception and completion of this document possible.

The person with the most direct influence on this document and all my work in Rochester was my thesis advisor, Professor Thomas Foster. His daily advice and encouragement were invaluable to my development in all aspects as a scientist, and I consider myself fortunate to have been a member of his group. His willingness to allow me to pursue areas I found interesting has been extraordinary, and in fact led to the topic of this thesis. To him I express my sincere gratitude.

I would like to thank David Conover for his mechanical and electrical skills as well as his seemingly endless willingness to help. Much of the development of the confocal microscope that is central to the work presented here was a product of his ingenuity and expertise.

I would also like to thank my fellow graduate students Jarod Finlay, Soumya Mitra, William Cottrell, Jeremy Wilson, Ken Wang and Ben Pearson with whom I have shared an office, a lab, or both. Soumya, Jarod and I shared an office for several years, and they were a source of many interesting and valuable conversa-

tions. Soumya introduced me to the confocal microscope upon my arrival in the lab and taught me the essentials of tissue culture. Jarod was the source of many scientific and inevitably philosophical conversations about light scattering that benefited me a great deal. Bill's expertise in the machine shop has been invaluable to me, especially in the closing months of hectic experiments that required special equipment that he always seemed to have. Jeremy was the source of many discussions about light scattering, and many of the insights he had were useful in development of my Monte Carlo code. Ben and Ken are recent additions to the group, and their help has been quite valuable in the past several months. Ben has been instrumental in advancing some of the newest ideas for anisotropy imaging and taking it from model systems to tissue.

David Niles and Evan Goren were two undergraduates that contributed to the daily operation of the lab as they performed cell culture and other various duties in their time in the medical center. Maxim Khimich was a rotation student that assisted with the depth-dependent anisotropy measurements in Chapter 2.

Several people from other groups at the University of Rochester deserve mention as their expertise was invaluable. Scott Gibson in the laboratory of Professor Russell Hilf provided crucial information regarding tissue culture and other related techniques. Dr. Hironao Wakabayashi in the laboratory of Professor Philip Fay assisted with fluorometer measurements that were the basis for microscope calibration. Dave Simon in the laboratory of Professor John Frelinger was a valuable source of biological expertise as well as the lung tissue presented in Chapter 6. Scott Gerber in the laboratory of Professor Edith Lord assisted with several experiments and with use of the conventional fluorescence microscope. I also wish

No mention of my time in Rochester would be complete without acknowledging my friends and fellow Institute of Optics students Dan Sykora, Ben Brown, and Gary Miller. From day one they have been great friends, and I certainly owe them a fraction of the sanity I have left after the long hard road of classes. I am lucky to have found such a great group of friends.

And, finally, I owe a great deal of gratitude to my parents, Dennis and Rebecca

Bigelow, and my fiancée, Kaylyn Makins, without whom this document would never have been written. My parents have been a constant source of love and encouragement throughout the long road of my academic career, and any successes I have had were by following their example. Kaylyn has been my daily source of inspiration and motivation, and is the reason why I was able to keep going the last few difficult months of writing. Her patience and support throughout the entire process have been truly amazing.

Abstract

Fluorescence polarization microscopy is a powerful modality capable of sensing changes in the physical properties and local environment of fluorophores. In this thesis we present new applications for the technique in cancer diagnosis and treatment and explore the limits of the modality in scattering media.

We describe modifications to our custom-built confocal fluorescence microscope that enable dual-color imaging, optical fiber-based confocal spectroscopy and fluorescence polarization imaging. Experiments are presented that indicate the performance of the instrument for all three modalities.

The limits of confocal fluorescence polarization imaging in scattering media are explored and the microscope parameters necessary for accurate polarization images in this regime are determined. A Monte Carlo routine is developed to model the effect of scattering on images. Included in it are routines to track the polarization state of light using the Mueller-Stokes formalism and a model for fluorescence generation that includes sampling the excitation light polarization ellipse, Brownian motion of excited-state fluorophores in solution, and dipole fluorophore emission. Results from this model are compared to experiments performed on a

fluorophore-embedded polymer rod in a turbid medium consisting of polystyrene microspheres in aqueous suspension.

We demonstrate the utility of the fluorescence polarization imaging technique for removal of contaminating autofluorescence and for imaging photodynamic therapy drugs in cell monolayers. Images of cells expressing green fluorescent protein are extracted from contaminating fluorescein emission. The distribution of meta-tetrahydroxyphenylchlorin in an EMT6 cell monolayer is also presented.

A new technique for imaging enzyme activity is presented that is based on observing changes in the anisotropy of fluorescently-labeled substrates. Proof-of-principle studies are performed in a model system consisting of fluorescently labeled bovine serum albumin attached to sepharose beads. The action of trypsin and proteinase K on the albumin is monitored to demonstrate validity of the technique. Images of the processing of the albumin in J774 murine macrophages are also presented indicating large intercellular differences in enzyme activity. Future directions for the technique are also presented, including the design of enzyme probes specific for prostate specific antigen based on fluorescently-labeled dendrimers. A technique for enzyme imaging based on extracellular autofluorescence is also proposed.

Table of Contents

List of Tables

List of Figures

Chapter 1

Introduction

This thesis is devoted to developing new applications of confocal fluorescence polarization microscopy for use in biology and medicine. In order to better understand the fundamental principles of imaging in an environment like tissue, this introduction will cover the basic diffraction-limited aspects of confocal fluorescence microscopy and provide a brief overview of tissue optical properties. Since the applications covered here all deal with measurements of polarized fluorescence, an introduction to the fundamentals of fluorescence anisotropy is also provided.

1.1 Fundamentals of confocal microscopy

Confocal microscopy is a widely used imaging modality with a long history that can be traced back to Minsky's 1961 patent [1]. It has uses in fields as disparate as materials science and biological imaging in both reflectance and fluorescence imaging modes. Implementation of confocal microscopy has exploded in the past 15 years due in large part to advances made in confocal fluorescence microscopy. These have been driven by the necessity in biomedical imaging to localize flu-

orescent sources in three dimensions. The various endogenous and exogenous fluorescent probes available thus give the ability to generate images that yield information on intra- and extracellular structure as well as cellular function.

Confocal imaging is achieved rather simply as shown in Figure 1.1. Excitation light enters the system and is focused onto the sample of interest to generate fluorescence. A fraction of the fluorescence signal is collected by the objective and relayed to the detector. In the most basic form, confocality is achieved by insertion of a pinhole in front of the detector. The aperture is optically conjugate with the excitation beam focus, and as a result preferentially passes light originating from the focus (solid line) while rejecting the majority of the light from outside the focal volume (dotted/dashed lines). The presence of the pinhole improves in-plane resolution by about a factor of 1.4 over conventional microscopy for optimal pinholes, but more importantly it gives the ability to "optically section" *i.e.* discriminate objects along the optical axis. By acquiring a series of images spaced along the optical axis, confocal microscopy gives the ability to measure the relative position of objects in three dimensions through sequential image observation or sophisticated reconstruction algorithms.

The disadvantage to intentionally restricting the region of observation to an extremely small volume near the focus is that the entire field of view is not simultaneously visible as it is with conventional microscopy. In practice the image must be built up on a per-pixel basis by employing a scanning mechanism. Numerous approaches are employed to accomplish this task, including the Nipkow spinning disk [2], object scanning, and beam scanning [3]. Our microscope em-
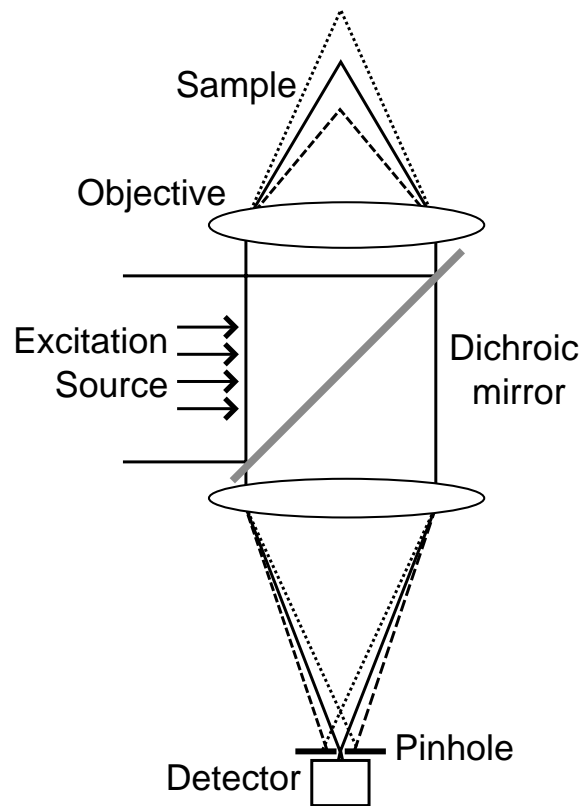
Figure 1.1: Basic setup of a confocal microscope. Excitation light excites fluorescence in the sample which passes through the dichroic mirror to the detector. Optical sectioning is achieved by insertion of a pinhole immediately in front of the detector. Out of focus light (indicated by dotted lines) is rejected by the pinhole and only that light originating at the focus is detected.

ploys beam scanning as it minimizes sample movement, especially for imaging objects immersed in liquid.

1.2 Fourier optics of confocal microscopy

Confocal fluorescence microscopy is an incoherent imaging technique that can be described in Fourier optics terms by the relation [4]

$$I_{image} = |h_1 \, h_{2eff}|^2 \otimes f, \tag{1.1}$$

where I_{image} is the image intensity, f is the spatial distribution of fluorescence, h_1 is the amplitude point spread function (psf) of the excitation optics, and h_{2eff} is the effective psf of the fluorescence collection optics. Since these include the pinhole, h_{2eff} is

$$|h_{2eff}|^2 = |h_2|^2 \otimes D, \tag{1.2}$$

where h_2 is the amplitude psf of the detection optics and D is the sensitivity function of the detector, which in the case of a pinhole is its spatial extent. A very large pinhole corresponding to a large D reduces the imaging to that of a conventional microscope. At the other extreme with an arbitrarily small detector, D becomes δ-like, h_{2eff} reduces to h_2, and the imaging can be described by [4–6]

$$I_{image} = |h_1(u, v) \, h_2(u/\kappa, v/\kappa)|^2 \otimes f. \tag{1.3}$$

Here the term κ is the ratio of the emission to excitation wavelengths ($\kappa =$

$\lambda_{em}/\lambda_{ex}$), and the excitation and detection psfs are expressed in terms of the normalized optical coordinates u and v. These in turn are related to the physical object radial and axial distances, ρ and z, by

$$v = \frac{2\pi}{\lambda_{ex}}\rho\sin\alpha \qquad \text{and} \qquad u = \frac{8\pi}{\lambda_{ex}}z\sin^2\left(\frac{\alpha}{2}\right), \qquad (1.4)$$

where $\sin\alpha$ is the numerical aperture of the objective. One consequence of fluorescence imaging is shown by the presence of κ in Equation 1.3. Involvement of a second, longer wavelength in the imaging process adversely affects the resolution in a manner directly proportional to the Stokes shift. Optimal performance is achieved as $\lambda_{em} \to \lambda_{ex}$, while as $\lambda_{em} \to \infty$ optical sectioning ability degrades.

Discrimination of point objects in-plane and axially is described by [7]

$$\Delta r_{conf} = \frac{0.32\lambda_{gm}}{NA} \qquad \text{and} \qquad \Delta z_{conf} = \frac{1.26n\lambda_{gm}}{NA^2}. \qquad (1.5)$$

In these expressions, Δr_{conf} and Δz_{conf} are the full width at half maximum (FWHM) resolution values in the lateral and axial directions and λ_{gm} is the *geometric* mean of the excitation (λ_{ex}) and emission (λ_{em}) wavelengths ($\lambda_{gm} = \sqrt{\lambda_{ex}\lambda_{em}}$). This arises because the excitation and fluorescence point spread functions multiply in confocal microscopy and are necessarily based upon different wavelengths. Note that the considerations outlined here are all approximate as fluorescence emission possesses a band of emission wavelengths. Typically these equations are evaluated at the peak of the emission and the spectral extent of the emission is not considered.

Since confocality relies on the placement of a pinhole in front of the detector, pinhole radius is the most important free parameter of a confocal system. Typically the size of the pinhole is calculated in terms of a normalized pinhole radius, v_p, defined as [4]

$$v_p = \frac{2\pi\rho}{\lambda_{ex}m_s}NA.$$ (1.6)

Here ρ is the physical pinhole diameter, m_s is the total magnification of the system, and NA is the numerical aperture of the microscope objective. The inclusion of m_s in the equation is necessary because the normalized coordinates in Equation 1.4 are calculated with respect to the object plane. The pinhole is located at the detector plane, and as a result the coordinates at the object must be multiplied by the total system magnification to yield the correct pinhole size.

There is a body of literature devoted to the proper selection of pinhole size based on several criteria [8–12]. Some of the first work in this area was performed by Wilson & Carlini, who looked at the effects of pinhole size in confocal reflectance imaging systems [8]. They found that the in-plane resolution is more susceptible to changes in pinhole size than is the axial resolution. Since axial resolution is the primary motivation for using confocal microscopy, relaxing the requirement that $v_p = 0.5$ for optimal in-plane imaging to $v_p \sim 2.5$ still allows reasonable optical sectioning to occur while increasing signal levels. Wilson found the same criterion to be valid for confocal fluorescence microscopy by investigating the axial response as a function of pinhole radius [6]. Kimura & Munakata also considered fluorescence confocal microscopy, but they examined the 3-D optical transfer function as a whole [9]. From these considerations, it was found

that $v_p < 1$ was almost equivalent to the infinitely small pinhole case, with plots indicating that the loss in detail was not dramatic for sizes as large as $v_p = 2$. From these papers, and in particular the work of Wilson, it is common to select a pinhole size that corresponds to $v_p = 2.5$ to yield appreciable signal levels while nearly preserving the axial section thickness provided by a smaller pinhole.

1.3 Image artifacts in confocal microscopy

While imaging deep into intact tissue sections is highly desirable from a biological standpoint, it presents significant optical problems. Most microscope objectives are optimized for imaging of thin, transparent samples located immediately adjacent to the coverslip. When imaging deep into a tissue sample, however, bulk tissue scattering and absorption degrade signal strength and compromise the diffraction-limited nature of the optics. Even in the absence of absorption and scattering there may be severe image degradations from monochromatic and chromatic aberrations.

1.3.1 Influence of optical aberrations

Spherical aberration is the most prevalent monochromatic aberration encountered in confocal microscopy performed at depth [13]. Refractive index mismatches between the objective immersion medium and the sample lead to spherical aberration that is more prevalent for higher numerical aperture objectives. The most commonly used immersion media for microscope objectives are air ($n = 1.00$), water ($n = 1.33$), glycerol ($n = 1.47$), and oil ($n = 1.515$). Unfortunately, it is impossible to match the refractive index of the immersion medium to that of all

cellular components as there is a range of subcellular targets with indices from 1.34-1.41 [14, 15]. As a result of the induced spherical aberration in cases with large discrepancies in refractive index, there is a dramatic loss in returned signal strength and resolution that can severely limit the depth to which images can be acquired. In going from an oil immersion objective (NA 1.3) into water, for example, intensity of the returned signal can be reduced by over 90% in moving the excitation beam focus from the sample surface to a depth of 50 μm. Under the same conditions, the FWHM of the axial and lateral psfs increase by a factor of 3 and 1.5, respectively [16].

1.3.2   Influence of light scattering

Image degradation due to scattering can be the dominant form of image quality reduction in confocal microscopy of biological samples. In the case of single-photon fluorescence imaging, the depth of penetration is limited by the reduction in image contrast and resolution due to fluorescence generated by scattered excitation photons [17–19]. Rejection of scattered light can be achieved by changing the NA, but the most effective means of discrimination is the use of a pinhole. When imaging deep into samples, however, the pinhole is no longer able to limit the collected light to just the focal region. Contribution from scattered light to the signal gradually increases with depth until eventually nearly all of the signal is scattered light. In some cases in highly scattering environments, the primary signal can originate from a region that is shallower than the focal zone with little signal from the ballistic light originating at the focus [20].

1.4 Review of tissue optical properties

Transmission of unscattered light through tissue decreases exponentially in accordance with Beer's Law. In the common language of tissue optics, this is described as

$$\frac{I_t}{I_0} = e^{-\mu_t \ell},\tag{1.7}$$

where I_t and I_0 are the transmitted and incident intensities, ℓ is the thickness of the tissue, and μ_t is the total attenuation coefficient. Absorption and scattering coefficients (μ_a and μ_s) are both accounted for in μ_t as

$$\mu_t = \mu_s + \mu_a = \frac{1}{\ell_s} + \frac{1}{\ell_a}.\tag{1.8}$$

In this equation μ_a and μ_s have been recast in terms of the absorption length, ℓ_a, and the scattering mean free path length in tissue, ℓ_s. For scattering in homogenous media, ℓ_s can be found from the scattering cross section, σ_s, and the number density of scattering particles, N, according to

$$\ell_s = \frac{1}{\sigma_s N}.\tag{1.9}$$

In addition to scattering and absorption coefficients, the other important physical property of tissue is the phase function, p. The phase function describes the probability of scattering into a given direction from the incident direction and is

normalized over all solid angles, Ω, according to

$$\int_{4\pi} p \, d\Omega = 1. \tag{1.10}$$

Typically in tissue optics an asymmetry parameter, g, is reported to describe the complicated nature of tissue scattering. It is the average cosine of the scattering angle, θ, defined by

$$g = \langle \cos \theta \rangle = \int_{4\pi} p \, \cos \theta \, d\Omega. \tag{1.11}$$

For distributions wherein the light scattering is completely isotropic or is symmetric about a scattering angle of 90°, $g=0$. Highly forward scattering or backscattering particles approach $g=1$ and $g=-1$, respectively.

Values for tissue optical coefficients vary widely depending on the tissue type and preparation. A summary of absorption, scattering, and anisotropy coefficients of dozens of tissue types is contained in a review by Cheong *et al.* and the references contained therein [21]. Typically for wavelengths in the range from 600 - 1000 nm, scattering dominates absorption as a mechanism of attenuation. In this range known as the "therapeutic window," μ_s is approximately 2 - 3 orders of magnitude greater than μ_a [22, 23]. For wavelengths less than 600 nm, hemoglobin and melanin absorption become large and it is no longer valid to assume $\mu_s \gg \mu_a$. The same holds true beyond 1000 nm where the near IR absorption of water is comparable to hemoglobin absorption for wavelengths in the visible less than 600 nm [24].

1.4.1 Scattering properties of cells and tissue

The origins of light scattering in tissue are well explored but not perfectly understood due to the highly complex nature of the index of refraction variations that lead to scattering [25]. What is clear, however, is that cells, cellular organelles, and the surrounding extracellular matrix all scatter light to varying degrees.

Light scattering measurements indicate that, even in the absence of extracellular matrix, cells and cellular organelles scatter light in a complicated fashion. Perelman *et al.* showed that scattering from nuclei is an observable effect in spectrally-resolved backscattering experiments [26]. They found that nuclear size distributions derived from analysis of backscattered light matched well with results from microscopy for two cell lines. Mitochondria are another important light scattering component of the cell, a fact that is supported by numerous studies. Bartlett *et al.* used an approach similar to that of Perelman *et al.* with polarized light spectroscopy to investigate the distribution of particles contributing to light scattering from Siha and MCF7 cell lines [27]. They found the most prominent source of scattering was from particles near 2 μm in size, which is consistent with typical mitochondrial dimensions [28]. We have also performed angularly resolved light scattering measurements of EMT6 cell suspensions and found that Mie theory fits to cellular scattering yield a distribution of particle diameters with a peak near 1 μm. We interpret this peak as representing mitochondria, and this is supported by electron microscopy studies. Data from this study are shown in Figure 1.2.

Another important source of scattering is the extracellular matrix, where it has
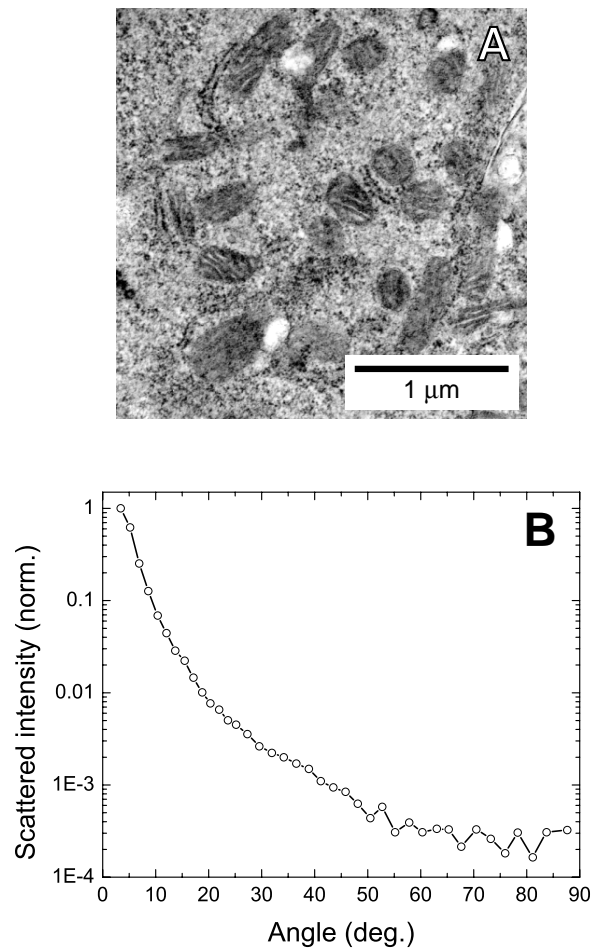
Figure 1.2: Intracellular morphology and angularly dependent light scattering. Panel A shows a transmission electron micrograph of an EMT6 cell monolayer. A region of interest is shown containing several mitochondria and a scale bar for reference. Panel B is a plot of the normalized angularly-resolved light scattering from an EMT6 cell suspension illuminated with 633 nm light from a helium-neon laser. As is the case in many tissue types, the scattering is highly peaked in the forward direction. This distribution can be interpreted as contributions from cellular organelles, and in particular from mitochondria like those shown in A.

been shown that collagen is an important source of tissue turbidity. Saidi *et al.*
found that scattering in neonatal skin was described well by cylindrical Mie scat-
tering combined with a Rayleigh-type scattering term for short wavelengths [29].
They attributed the majority of the scattering to collagen fibers, a conclusion that
was supported by histology and with measured age-dependent changes in collagen
fiber diameter. Nickell *et al.* concluded that collagen orientation was responsible
for the anisotropic propagation of light in human skin [30]. These results were
verified *via* Monte Carlo simulations and measurements of the anisotropic nature
of the scattered light distribution at the tissue surface from different parts of the
body. Incidentally, it has also been shown that the structure of collagen leads to
it exhibiting birefringence. This property has been exploited in optical coherence
tomography studies for quantifying burn severity in human skin by measuring the
temperature-induced changes in collagen birefringence [31].

Equations 1.7 and 1.8 indicate the importance of the magnitude of μ_s as it
relates to μ_t, but they do not account for the contribution of the asymmetry
parameter, g. The angular distribution of scattering is quite important, especially
in cases where detected light is dominated by a very small number of scattering
events [32]. Since most tissues are very forward scattering, g tends toward 1.
Marchesini *et al.* found g to range from 0.68 to 0.75 for several human tissues,
while Ghosh *et al.* found g to be 0.88 and 0.96 for normal and malignant breast
tissue, respectively [23, 33]. The highly forward directed nature of the scattering
indicates that the size of the important scatterers in biology is most likely on
the order of the wavelength of light or larger. However, fits to scattering data

from both Marchesini *et al.* and Ghosh *et al.* required the inclusion of a term to account for Rayleigh-like scattering from very small particles at large angles.

1.4.2 Absorption properties of cells and tissue

Although $\mu_s \gg \mu_a$ in the red and near IR regions of the spectrum, quite often measurements are made at wavelengths less than 600 nm or greater than 1000 nm where absorption plays a more important role in attenuation. There are several important endogenous tissue absorbers including cytochromes [34], melanin [35], water [36, 37], and hemoglobin [38, 39]. The most important of these absorbers in the visible range is hemoglobin, whose absorption is shown in Figure 1.3. The most important features to notice are the double-peaked spectral features near 550 nm and the large difference between oxy- and deoxyhemoglobin (HbO$_2$ and Hb) absorption from 600-700 nm. The large magnitude of hemoglobin absorption and its oxygen-dependent spectral features make it an ideal candidate for monitoring tissue oxygenation and manipulating tissue optical properties. Along those lines, a recent paper from Mitra and Foster in our group showed that carbogen breathing enhances light penetration by increasing HbO$_2$ *in vivo* at the photodynamic therapy (PDT)-relevant wavelengths of 630 and 650 nm [40]. In this case, carbogen breathing has the dual benefit of increasing oxygen availability for PDT while simultaneously decreasing μ_a and allowing greater light penetration.
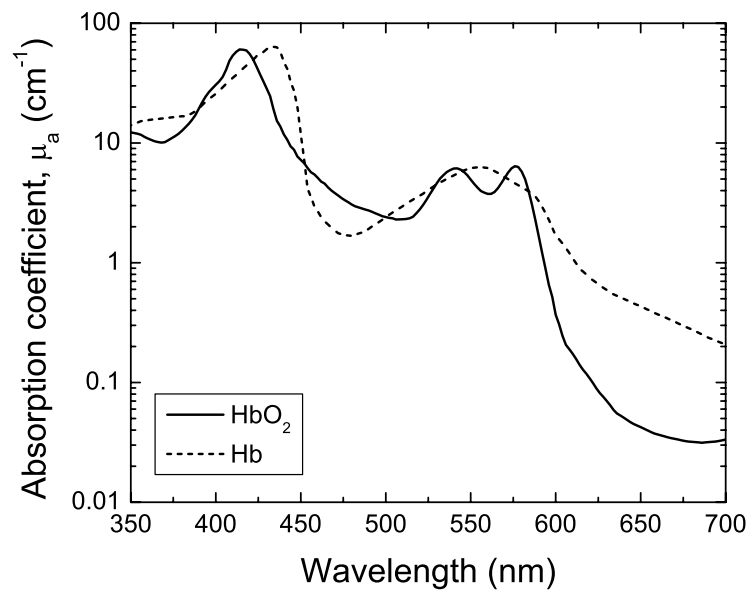
Figure 1.3: Absorption spectrum of 50 μM oxy- (HbO$_2$) and deoxyhemoglobin (Hb). Data plotted is a tabulation by Scott Prahl that is available on the website `omlc.ogi.edu`.

1.5 Fluorescence Anisotropy

Fluorescence anisotropy measurements are used in fluorometers for applications such as binding studies and enzyme assays, but they have been much less developed in the context of imaging. Measures of anisotropy, r, can separate signals from fluorophores with overlapping spectra but different rotational correlation times [41, 42], image membrane fluidity and the orientation of fluorophores in biological membranes [43], and image the binding and/or cleaving of fluorophores to or from larger molecules [44, 45]. Sensitivity to this polarization through proper selection of excitation light and detection parameters yields information about the molecule of interest and the environment in which it resides.

In this section a brief overview of fluorescence anisotropy is presented in anticipation of steady-state measurements detailed in this thesis. For other overviews of fluorescence polarization in much more detail, the reader is referred to excellent reviews by Lakowicz [46], Kawski [47], Cantor & Schimmel [48], and Weber [49].

1.5.1 Principles of fluorescence emission and polarization

The technique for measuring r is based on the property that fluorescence emission is polarized with respect to a linearly polarized excitation beam. Fluorescence emitted from the sample is collected and split into two orthogonal polarizations, one parallel ($I_{\parallel}$) and one perpendicular ($I_{\perp}$) to the incident polarization vector. The two intensities can then be analyzed to yield the anisotropy according to [46]

$$r = \frac{I_{\parallel} - I_{\perp}}{I_{\parallel} + 2I_{\perp}}. \tag{1.12}$$

Anisotropy is therefore a measure of the polarization state of the fluorescence emission found using the difference between two polarization components normalized by the total intensity emitted by the fluorophore into 4π steradians.

In principle r can be measured to be unity if $I_\perp = 0$, *i.e.* the molecule emits fluorescence that is polarized strictly parallel to the excitation beam vector. In practice this does not occur, as there are several factors that reduce the highest expected anisotropy.

1.5.2 Intrinsic sources of depolarization

In general measured anisotropies are seldom equal to 1 due to a number of factors influencing the fluorescence process. The first class of these factors is considered intrinsic as it involves the details of the energy transfer inside the molecule or depends fundamentally on photoselection. These processes can be better understood by first considering a single excited fluorescent molecule [46, 47]. Figure 1.4 is a representation of a molecule that has been excited with light polarized along the z axis [46]. It is assumed that the emission dipole is aligned with the axis of the molecule. The intensity of light passing through a polarizer located parallel ($I_\parallel$) or perpendicular ($I_\perp$) to the z axis will depend on $\cos^2 \psi$ or $\sin^2 \psi \sin^2 \phi$, respectively.

For fluorophore concentrations relevant to confocal microscopy, anisotropy measurements are made on ensembles rather than individual molecules. In a region containing a collection of randomly oriented molecules as occurs in fluid solution, the intensities will depend on the average orientation of all the molecules excited by the incident beam decomposed into intensities along each axis. $I_\parallel$ and
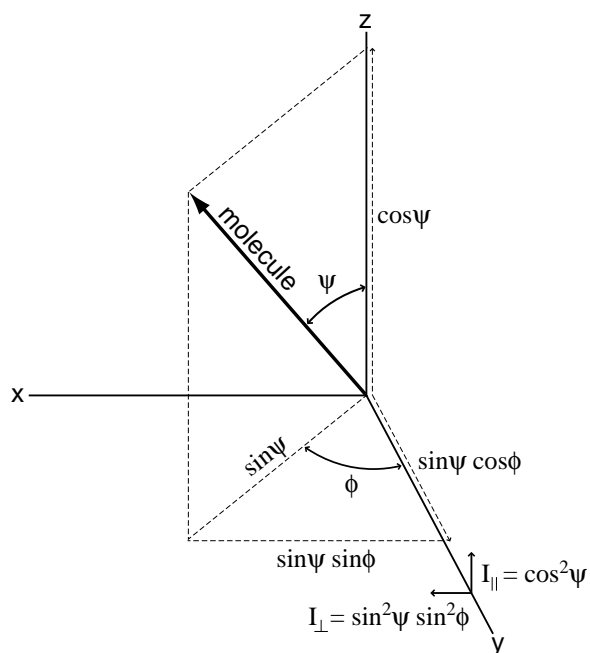
Figure 1.4: Orientation of a single molecule and the resulting projection of the polarization onto each axis. In this figure the input polarization is assumed to be parallel to the z-axis.

$I_\perp$ therefore depend on the average values $\langle \cos^2 \psi \rangle$ and $\langle \sin^2 \psi \rangle$. This behavior coupled with equation 1.12 gives a value for r according to

$$r = \frac{3 \langle \cos^2 \psi \rangle - 1}{2}. \tag{1.13}$$

The value of $\langle \cos^2 \psi \rangle$ due to photoselection therefore determines the fundamental anisotropy, r_0, the maximum value expected from a measurement in the absence of other depolarization factors. As indicated by the form of $\langle \cos^2 \psi \rangle$,

$$\langle \cos^2 \psi \rangle = \frac{\int\limits_0^{\pi/2} \cos^2 \psi \, f(\psi) \, d\psi}{\int\limits_0^{\pi/2} f(\psi) \, d\psi}, \tag{1.14}$$

the form of the probability of photon absorption, $f(\psi)$, determines r_0. In a random distribution of molecules the single photon excitation probability is azimuthally symmetric and depends on the angle between the polarization vector and the molecule according to $f(\psi) = \cos^2 \psi \sin \psi \, d\psi$. Insertion of this expression into equations 1.13 and 1.14 yields a maximum of $r_0 = 0.4$.

The relative orientation of the absorption and emission transition moments is another intrinsic factor influencing the measured anisotropy. In the derivation above it was assumed that the angle between the absorption and emission dipole moments, β, was zero. This is not the case in general as different molecules possess different values for β, and even in a single molecule β may change with excitation wavelength [49]. The net effect of depolarization on r_0 is similar to the form from

photoselection, namely

$$r_0 = \frac{2}{5} \left(\frac{3 \cos^2 \beta - 1}{2} \right).$$ (1.15)

In this equation it is assumed that r_0 from photoselection yields 0.4, which is the origin of the $\frac{2}{5}$ preceding the term in parentheses.

1.5.3 Extrinsic sources of depolarization

While intrinsic factors contribute to depolarization of fluorescence signals, they are of limited practical interest for the purposes of the research presented here. However, extrinsic factors modify the fluorescence in ways that give information about the local environment, molecular mass, and even fluorescence lifetime. In steady-state measurements these effects are intertwined and lead to changes in polarization that make the technique useful by allowing manipulation of parameters of interest and measuring the effects *via* r measurements. For example, in Chapter 5 we present a technique in which we monitor enzyme activity through changes in molecular weight and fluorescence lifetime.

One of the most important extrinsic sources of depolarization is the rotational motion of fluorophores in solution. Even for molecules in which ideal orientations of the emission and absorption dipoles yield $r_0 = 0.4$, the effects of molecular tumbling in solution lead to $r < r_0$ for steady-state measurements. The ease with which molecules tumble in solution is described by the rotational correlation time, τ_r, which is dependent on a number of physical parameters. For example, τ_r for a

globular protein can be estimated using

$$\tau_r = \frac{\eta V}{RT} = \frac{\eta M}{RT}\left(\bar{\nu} + h\right),\tag{1.16}$$

where T is the temperature in degrees Kelvin, R is the universal gas constant, η is the viscosity, $\bar{\nu}$ is the specific volume of the protein, M is the mass, and h is the hydration. In steady-state anisotropy measurements on spherical rotators the effect of rotation and fluorescence lifetime, τ, on anisotropy is given by the Perrin equation [50],

$$\frac{r_0}{r} = 1 + \frac{\tau}{\tau_r}.\tag{1.17}$$

The net effect of both intrinsic and extrinsic depolarization factors is to reduce r in a multiplicative manner according to Soleillet's Rule [46]. For the case where r is affected by photoselection, non-parallel transition dipoles, and rotational depolarization, respectively, this takes the form

$$r = \frac{2}{5}\left(\frac{3\cos^2\beta - 1}{2}\right)\left(1 + \frac{\tau}{\tau_r}\right)^{-1},\tag{1.18}$$

which can be seen to collapse back to $r = 0.4$ in the case where $\beta = 0$ and there is no rotational molecular motion, $i.e.$, $\tau_r \to \infty$.

1.5.4   Optical sources of depolarization

The nature of high NA objectives complicates the measurement of fluorescence polarization. High NA lenses necessary for visualization of small targets drive the measured anisotropy artificially toward zero. This arises from both the excitation

and collection geometries [51]. Excitation light delivered to the sample by high NA objectives contains polarization components that are not oriented strictly along the direction of that in the beam incident on the objective lens [52, 53]. These components tend to be small for propagation vectors near the optical axis, but farther away they can be comparable in magnitude to the component along the incident polarization vector. Detection of fluorescence also introduces errors in the measured anisotropy. High numerical apertures allow the objective to sample polarization components along all three cartesian coordinates in object space [54]. This effect on its own can reduce the anisotropy by nearly 25% as the NA (in unit index medium) approaches one. These two effects lead to measured values for the anisotropy that can be significantly lower than the actual value, with the effect being more pronounced for higher numerical apertures. The use of confocal microscopy tends to alleviate the problem somewhat as optimal pinholes discriminate against some of the components distorted by high aperture focusing [55].

Scattering of light by small particles in the sample also reduces the measured anisotropy. This problem is widely recognized and observed in the measurement of anisotropy in conventional fluorometers containing cell suspensions [56–58]. A single scattering event can reduce the anisotropy by a factor of 0.7 [59], so detection of light scattered even a small number times will adversely affect the performance of a microscope. Gan *et al.* found that 0.202 μm polystyrene beads ($n = 1.59$) in water reduced the degree of polarization of 633 nm light markedly [60]. The effect was so strong, in fact, that the degree of polarization monotonically decreased as a function of depth and was reduced to nearly zero at a depth of 5 mean free

scattering depths. Small particles in cells such as mitochondria are on the order of this size, so scattering in tissue has much the same effect on polarization.

1.6   Review of the r imaging literature

The combination of fluorescence anisotropy and imaging has not been widely exploited, and confocal anisotropy imaging in particular has been quite seldomly used. Several groups have used the confocal arrangement to limit a spatial area of sampling to perform time-resolved anisotropy at specific regions in individual cells and monolayers. These studies looked at torsional dynamics of DNA [61], the design of a two-photon multi-functional microscope for time resolved anisotropy measurements [62] and homo-FRET in cells to look at monomer-dimer transitions of GFP fusion proteins [63]. These investigations were not designed to image wide fields of view using confocal microscopy, however. The technique of mapping r throughout an entire cell has been used to a limited degree in recent years. Wu *et al.* used imaging of steady-state fluorescence anisotropy to monitor membrane changes in human astrocytoma cells induced by ATP depletion [64]. They were looking at the effects of the antioxidants gossypol and tirilazad on cell membranes undergoing stress from iodoacetic acid-induced ATP depletion. Confocal fluorescence polarization imaging has also been shown to be useful in imaging orientational order in liquid crystals [65]. By doping the liquid crystals with *n,n'-bis*(2,5-di-tert-butylphenyl)-3,4,9,10-perylenedicarboximide (BTBP), the three-dimensional order throughout the samples was obtained by noting changes in the direction-dependent fluorescence polarization. Blackman *et*

al. looked at orientation of eosin-5-maleimide on the erythrocyte anion channel protein band 3 in erythrocyte ghosts by measuring confocal fluorescence anisotropy [43]. They found evidence for three rotational species that could account for several uniaxial rotational diffusion times. The work most relevant to that described here was performed by Entwistle & Noble [66, 67]. They used confocal fluorescence polarization microscopy as a means to find the concentration of fluorophore at which the response to incident light becomes nonlinear in intensity. Energy transfer between adjacent fluorophores gave a decrease in fluorescence polarization at a concentration slightly below that which leads to collisional quenching of fluorescence. This has obvious applications in antibody labeling of biological samples where local concentrations of fluorophores can be very high.

1.7   Thesis overview

In Chapter 2 the details of our custom-built attachment for confocal microscopy and spectroscopy are presented. The chapter focuses on the optics necessary to enable fluorescence polarization imaging and confocal fluorescence spectroscopy. The details of the original design and construction of the scanning optics were covered previously in Irene Georgakoudi's thesis [68]. Chapter 2 concludes with some representative cases demonstrating the utility of the setup. Most of Chapter 2 has been published in either our 2001 *Review of Scientific Instruments* paper or our 2003 *Optics Letter* [69, 70]. Joint authorship on these papers is gratefully

acknowledged with Thomas H. Foster, Curtis J. Harkrider, David L. Conover, Irene Georgakoudi, Soumya Mitra, Michael G. Nichols, and Milind Rajadyaksha.

A Monte Carlo routine developed for modeling confocal fluorescence polarization imaging is the focus of Chapter 3. The chapter starts with a brief overview of Monte Carlo methods as an introduction to the specific approaches used in simulations of fluorescence polarization. Background theory and Monte Carlo algorithms are presented for routines that are not widely used, deserve special mention, or that are being presented here for the first time in the context of confocal fluorescence imaging.

Chapter 4 presents results from experiments designed to quantify the effects of scattering on fluorescence polarization imaging. Monodisperse polystyrene microsphere suspensions are used as the model turbid medium in order to compare experiments directly with Mie theory calculations included in the Monte Carlo routines. The effects at depth in scattering media are probed by imaging a fluorophore-embedded polymer bar in solutions containing various bead sizes. The chapter concludes by determining which optical parameters can best increase the efficacy of confocal fluorescence polarization imaging in turbid media.

Chapter 5 presents the background proof-of-principle experiments for a new technique that allows enzyme activity imaging by measuring fluorescence anisotropy on a per-pixel basis. Results from a model system comprised of sepharose beads with the enzymes proteinase K and trypsin are shown, which demonstrate the feasibility of the method. Studies are also shown that extend the imaging modality to J774 murine macrophages acting on bodipy-labeled bovine serum albumin. Finally, a set of experiments are presented that outline an ap-

proach to imaging enzyme activity with constructs developed containing the substrate for prostate specific antigen. The proof-of-principle sections of the chapter have been published previously, and co-authorship with Thomas H. Foster, John G. Frelinger, and Harshad D. Vishwasrao is gratefully acknowledged.

Chapter 6 concludes the thesis by covering some other promising applications of fluorescence polarization imaging and looking toward the future of anisotropy-based enzyme activity imaging. The promise of discriminating two spectrally similar fluorophores on the basis of different fluorescence anisotropies is discussed. The technique is shown to be practical on cellular length scales and shows promise in discriminating a target signal immersed in contaminating autofluorescence. Fluorescence polarization imaging is also applied to the localization of photosensitizers in cell monolayers. A set of images of cells incubated with the PDT drug mTHPC is shown that exhibits some potentially interesting drug properties. Future directions for confocal fluorescence polarization microscopy are also presented.

References

[1] M. Minsky, "Microscopy apparatus," United States Patent 3,013,467, (Filed Nov. 7, 1957) (1961).

[2] M. Egger and M. Petráň, "New reflected-light microscope for viewing unstained brain and ganglion cells," Science **157,** 305–307 (1967).

[3] *Handbook of Biological Confocal Microscopy*, J. Pawley, ed., (Plenum Press, New York, 1990).

[4] *Confocal Microscopy*, T. Wilson, ed., (Academic Press, London, 1990).

[5] T. Wilson and C. Sheppard, *Theory and Practice of Scanning Optical Microscopy* (Academic Press, London, 1984).

[6] T. Wilson, "Optical sectioning in confocal fluorescent microscopes," J. Microsc. **154,** 143–156 (1989).

[7] R. H. Webb, "Theoretical basis of confocal microscopy," Methods Enzymol. **307,** 3–20 (1999).

[8] T. Wilson and A. R. Carlini, "Size of the detector in confocal imaging systems," Opt. Lett. **12,** 227–229 (1987).

[9] S. Kimura and C. Munakata, "Dependence of 3-D optical transfer functions on the pinhole radius in a fluorescent confocal optical microscope," Appl. Optics **29,** 3007–3011 (1990).

[10] J. Schmitt, A. Knuttel, and M. Yadlowsky, "Confocal microscopy in turbid media," J. Opt. Soc. Am. A **11,** 2226–2235 (1994).

[11] X. Gan, S. Schilders, and M. Gu, "Image formation in turbid media under a microscope," J. Opt. Soc. Am. A **15,** 2052–2058 (1998).

[12] C. Smithpeter, A. Dunn, A. Welch, and R. Richards-Kortum, "Penetration depth limits of *in vivo* confocal reflectance imaging," Appl. Optics **37,** 2749–2754 (1998).

[13] S. Hell, G. Reiner, C. Cremer, and E. Stelzer, "Aberrations in confocal fluorescence microscopy induced by mismatches in refractive index," J. Microsc. **169,** 391–405 (1993).

[14] G. Tearney, M. Brezinski, J. Southern, B. Bouma, M. Hee, and J. Fujimoto, "Determination of the refractive index of highly scattering human tissue by optical coherence tomography," Opt. Lett. **20,** 2258–2260 (1995).

[15] R. Drezek, A. Dunn, and R. Richards-Kortum, "Light scattering from cells: finite-difference time-domain simulations and goniometric measurements," Appl. Optics **38,** 3651–3661 (1999).

[16] H. Jacobsen and S. Hell, "Effect of the specimen refractive index on the imaging of a confocal fluorescence microscope employing high aperture oil immersion lenses," Bioimaging **3,** 39–47 (1995).

[17] M. Gu, S. Schilders, and X. Gan, "Two-photon fluorescence imaging of microspheres embedded in turbid media," J. Mod. Opt. **47,** 959–965 (2000).

[18] X. Gan and M. Gu, "Fluorescence microscopic imaging through tissue-like turbid media," J. Appl. Phys. **87,** 3214–3221 (2000).

[19] S. Schilders and M. Gu, "Limiting factors on image quality in imaging through turbid media under single-photon and two-photon excitation," Microsc. Microanal. **6,** 156–160 (2000).

[20] X. Gan and M. Gu, "Spatial distribution of single-photon and two-photon fluorescence light in scattering media: Monte Carlo simulation," Appl. Optics **39,** 1575–1579 (2000).

[21] W.-F. Cheong, S. A. Prahl, and A. J. Welch, "A review of the optical properties of biological tissues," IEEE J. Quantum Elect. **26,** 2166–2185 (1990).

[22] S. L. Jacques, C. A. Alter, and S. A. Prahl, "Angular dependence of HeNe laser light scattering by human dermis," Lasers Med. Sci. **1,** 309–333 (1987).

[23] R. Marchesini, A. Bertoni, S. Andreola, E. Melloni, and A. E. Sichirollo, "Extinction and absorption coefficients and scattering phase functions of human tissues *in vitro*," Appl. Opt. **28,** 2318–2324 (1989).

[24] R. Richards-Kortum and E. Sevick-Muraca, "Quantitative optical spectroscopy for tissue diagnosis," Annu. Rev. Phys. Chem. **47,** 555–606 (1996).

[25] J. M. Schmitt and G. Kumar, "Turbulent nature of refractive-index variations in biological tissue," Opt. Lett. **21,** 1310–1312 (1996).

[26] L. Perelman *et al.*, "Observation of periodic fine structure in reflectance from biological tissue: a new technique for measuring nuclear size distribution," Phys. Rev. Lett. **80,** 627–630 (1998).

[27] M. Bartlett, G. Huang, L. Larcom, and H. Jiang, "Measurement of particle size distribution in mammalian cells *in vitro* by use of polarized light spectroscopy," Appl. Optics **43,** 1296–1307 (2004).

[28] G. E. Palade, "An electron microscopy study of the mitochondrial structure," J. Histochem. Cytochem. **1,** 188–211 (1953).

[29] I. S. Saidi, S. L. Jacques, and F. K. Tittel, "Mie and Rayleigh modeling of visible-light scattering in neonatal skin," Appl. Optics **34,** 7410–7418 (1995).

[30] S. Nickell, M. Hermann, M. Essenpreis, T. J. Farrell, U. Krämer, and M. S. Patterson, "Anisotropy of light propagation in human skin," Phys. Med. Biol. **45,** 2873–2886 (2000).

[31] M. Pierce, R. L. Sheridan, B. H. Park, B. Cense, and J. F. de Boer, "Collagen denaturation can be quantified in burned human skin using polarization-sensitive optical coherence tomography," Burns **30,** 511–517 (2004).

[32] J. R. Mourant, J. Boyer, A. H. Hielscher, and I. J. Bigio, "Influence of the scattering phase function on light transport measurements in turbid media performed with small source-detector separations," Opt. Lett. **21,** 546–548 (1996).

[33] N. Ghosh, S. K. Mohanty, S. K. Majumder, and P. K. Gupta, "Measurement of optical transport properties of normal and malignant human breast tissue," Appl. Optics **40,** 176–184 (2001).

[34] E. L. Hull and T. H. Foster, "Cytochrome spectroscopy in scattering suspensions containing mitochondria and red blood cells," Appl. Spectrosc. **55,** 149–154 (2001).

[35] S. L. Jacques and D. J. McAuliffe, "The melanosome: threshold temperature for explosive vaporization and internal absorption coefficient during pulsed laser irradiation," Photochem. Photobiol. **53,** 769–775 (1991).

[36] L. Kou, D. Labrie, and P. Chylek, "Refractive indices of water and ice in the 0.65- to 2.5-μm spectral range," Appl. Optics **32,** 3531–3540 (1993).

[37] R. M. Pope and E. S. Fry, "Absorption spectrum (380-700 nm) of pure water. II. Integrating cavity measurements," Appl. Optics **36,** 8710–8723 (1997).

[38] S. Wray, M. Cope, D. T. Delpy, J. S. Wyatt, and E. O. R. Reynolds, "Characterization of the near-infrared absorption spectra of cytochrome aa$_3$ and hemoglobin for the noninvasive monitoring of cerebral oxygenation," Biochim. Biophys. Acta **933,** 184–192 (1988).

[39] W. G. Zijlstra, A. Buursma, and W. P. M. van der Roest, "Absorption spectra of human fetal and adult oxyhemoglobin, de-oxyhemoglobin, carboxyhemoglobin, and methemoglobin," Clin. Chem. **37,** 1633–1638 (1991).

[40] S. Mitra and T. H. Foster, "Carbogen breathing significantly enhances the penetration of red light in murine tumors *in vivo*," Phys. Med. Biol. **49,** 1891–1904 (2004).

[41] A. Knight, N. Goddard, P. Fielden, M. Barker, N. Billinton, and R. Walmsley, "Fluorescence polarisation of green fluorescent protein (GFP). A strategy for improved wavelength discrimination for GFP determinations," Anal. Commun. **36,** 113–117 (1999).

[42] A. Knight, N. Goddard, N. Billinton, P. Cahill, and R. Walmsley, "Fluorescence polarization discriminates green fluorescent protein from interfering autofluorescence in a microplate assay for genotoxicity," J. Biochem. Biophys. Methods **51,** 165–177 (2002).

[43] S. Blackman, C. Cobb, A. Beth, and D. Piston, "The orientation of eosin-5-maleimide on human erythrocyte band 3 measured by fluorescence polarization microscopy," Biophys. J. **71,** 194–208 (1996).

[44] P. Wu, M. Brasseur, and U. Schindler, "A high-throughput STAT binding assay using fluorescence polarization," Anal. Biochem. 1 **249,** 29–36 (1997).

[45] C. E. Bigelow, H. D. Vishwasrao, J. G. Frelinger, and T. H. Foster, "Imaging enzyme activity with polarization-sensitive confocal fluorescence microscopy," J. Microsc. **215,** 24–33 (2004).

[46] J. R. Lakowicz, *Principles of Fluorescence Spectroscopy*, 2nd ed. (Kluwer Academic/Plenum Publishers, New York, 1999).

[47] A. Kawski, "Fluorescence Anisotropy - Theory and applications of rotational depolarization," Crit. Rev. Anal. Chem. **23,** 459–529 (1993).

[48] C. R. Cantor and P. R. Schimmel, *Biophysical Chemistry Part II: Techniques for the study of biological structure and function* (W.H. Freeman and Company, New York, 1980).

[49] G. Weber, in *Fluorescence and Phosphorescence Analysis*, D. Hercules, ed., (John Wiley & Sons, New York, 1966), pp. 217–240.

[50] J. R. Lakowicz, F. G. Prendergast, and D. Hogen, "Differential polarized phase fluorometric investigations of diphenylhexatriene in lipid bilayers. Quantitation of hindered depolarizing rotations," Biochemistry **18,** 508–519 (1979).

[51] D. Axelrod, "Fluorescence polarization microscopy," Methods Cell Biol. **30,** 333–352 (1989).

[52] B. Richards and E. Wolf, "Electromagnetic diffraction in optical systems II. Structure of the image field in an aplanatic system," Proc. R. Soc. Lon. Ser. A **253,** 358–379 (1959).

[53] A. Yoshida and T. Asakura, "Electromagnetic field near the focus of gaussian beams," Optik **41,** 281–292 (1974).

[54] D. Axelrod, "Carbocyanine dye orientation in red cell membrane studied by microscopic fluorescence polarization," Biophys. J. **26,** 557–573 (1979).

[55] W. Inami and Y. Kawata, "Three-dimensional imaging analysis of confocal and conventional microscopes by use of Mie scattering theory," Appl. Optics **39,** 6369–6373 (2000).

[56] B. Dickens, T. Snow, V. Green, and W. Weglicki, "The effect of erythrocyte associated light scattering on membrane fluorescence polarization," Mol. Cell. Biochem. **79,** 91–94 (1988).

[57] H. Kutchai, V. Huxley, and L. Chandler, "Determination of fluorescence polarization of membrane probes in intact erythrocytes. Possible scattering artifacts," Biophys. J. **39,** 229–232 (1982).

[58] B. Lentz, B. Moore, and D. Barrow, "Light-scattering effects in the measurement of membrane microviscosity with diphenylhexatriene," Biophys. J. **25,** 489–494 (1979).

[59] F. Teale, "Fluorescence depolarization by light-scattering in turbid solutions," Photochem. Photobiol. **10,** 363–374 (1969).

[60] X. Gan, S. Schilders, and M. Gu, "Image enhancement through turbid media under a microscope by use of polarization gating methods," J. Opt. Soc. Am. A **16,** 2177–2184 (1999).

[61] M. Tramier, K. Kemnitz, C. Durieux, J. Coppey, P. Denjean, R. Pansu, and M. Coppey-Moisan, "Restrained torsional dynamics of nuclear DNA in living proliferative mammalian cells," Biophys. J. **78,** 2614–2627 (2000).

[62] A. Diaspro, G. Chirico, F. Federici, F. Cannone, S. Beretta, and M. Robello, "Two-photon microscopy and spectroscopy based on a compact confocal scanning head," J. Biomed. Opt. **6,** 300–310 (2001).

[63] I. Gautier, M. Tramier, C. Durieux, J. Coppey, R. Pansu, J.-C. Nicolas, K. Kemnitz, and M. Coppey-Moisan, "Homo-FRET microscopy in living cells to measure monomer-dimer transition of GFP-tagged proteins," Biophys. J. **80,** 3000–3008 (2001).

[64] Y. Wu, F. Sun, D. Tong, and B. Taylor, "Changes in membrane properties during energy depletion-induced cell injury studied with fluorescence microscopy," Biophys. J. **71,** 91–100 (1996).

[65] I. Smalyukh, S. Shiyanovskii, and O. Lavrentovich, "Three-dimensional imaging of orientational order by fluorescence confocal polarizing microscopy," Chem. Phys. Lett. **336,** 88–96 (2001).

[66] A. Entwistle and M. Noble, "The use of polarization analysis in the quantification of fluorescent emission: general principles," J. Microsc. **165,** 331–346 (1992).

[67] A. Entwistle and M. Noble, "The quantification of fluorescent emission from biological samples using analysis of polarization," J. Microsc. **165,** 347–365 (1992).

[68] I. Georgakoudi, Ph.D. thesis, University of Rochester, 1998.

[69] C. E. Bigelow, C. J. Harkrider, D. L. Conover, T. H. Foster, I. Georgakoudi, S. Mitra, M. G. Nichols, and M. Rajadhyaksha, "Retrofitted confocal laser scanner for a commercial inverted fluorescence microscope," Rev. Sci. Instrum. **72,** 3407–3410 (2001).

[70] C. E. Bigelow, D. L. Conover, and T. H. Foster, "Confocal fluorescence spectroscopy and anisotropy imaging system," Opt. Lett. **28,** 695–697 (2003).

Chapter 2

Development of Microscope Attachments for Confocal Fluorescence Spectroscopy and Anisotropy Imaging

2.1 Introduction

In this chapter, we report the design and implementation of attachments to our custom-built laser scanning confocal fluorescence system to allow spectroscopy and anisotropy imaging capabilities. In its original configuration, the confocal microscope was based around the Nikon Diaphot TMD and only required single channel detection of fluorescence emission [1, 2]. We have since expanded the capabilities of the system in response to the demands of photosensitizer photobleaching studies [3, 4] and fluorescence polarization imaging requirements [5]. Modifications to that system are outlined in detail here as well as in a recent paper from our group [6].

Objective	Description	Pinhole diameters	
		Optimal	Actual
4×, 0.13 NA	Air, Plan Fluor	120 μm	100 μm
10×, 0.45 NA	Air, Plan Apo	87 μm	75 μm
20×, 0.75 NA	Oil/glycerol/water, Plan Fluor	104 μm	100 μm
40×, 0.95 NA	Air, Plan Apo	165 μm	150 μm
60×, 1.4 NA	Oil, Plan Apo	168 μm	150 μm

Table 2.1: Pinhole sizes required for the Nikon TE2000 microscope with each objective at 600 nm excitation. Specifications are listed along with the optimal normalized pinhole diameter and pinhole diameter to be used from the discrete diameters commercially available. All objectives listed are from the CFI60 infinity corrected series with the exception of the 60× objective which is a 160mm tube length lens requiring an adaptor for use with the TE2000.

2.2 Microscope modifications

The original design and implementation of our custom built confocal microscope is outlined exhaustively in the Ph.D. thesis of Irene Georgakoudi [1] as well in our 2001 *Review of Scientific Instruments* paper [2]. The details of the optics excluding the detectors and the commercial microscope platform remain unchanged from the setup described therein, so the reader is referred to those sources for the relevant details. Two significant upgrades are worth mentioning, however. Since the initial implementation, we have upgraded to a Nikon TE2000-U platform (Nikon Instruments Inc., Melville, NY), which allows access to the CFI60 series infinity corrected objectives and enables conventional digital photography to be implemented simultaneously with laser scanning confocal imaging. This change did not modify the overall system magnification, however, as the magnification to the side port intermediate image plane is still that of the objective just as it was with the Diaphot. As a result, the total magnification from sample to pinhole is still 8.2 times the objective magnification. Pinhole diameters necessary for confocality based on $v_p = 2.5$ with this new set of lenses are listed in Table 2.1. Data acquisition has also been upgraded with the addition of a 16-bit, 200 kHz data acquisition board that increases our dynamic range in intensity images (DaqBoard/2000, IOtech Inc., Cleveland, OH).

A schematic diagram of the system is shown in Figure 2.1, and a list of all new parts added to the system is included in Table 2.2. An argon-ion laser (Ion Laser Technology, Salt Lake City, UT), helium-neon laser (Melles Griot Inc., Irvine, CA) and a dye laser (Model 599, Coherent Inc., Santa Clara, CA) equipped with two

dye reservoirs provide 488 nm, 514 nm, 633 nm, and continuously tunable light from approximately 530 - 680 nm. These sources are all coupled into a single-mode optical fiber to allow source portability, decrease optical table vibrations, and to yield the optimal single transverse mode output for the excitation beam. Output of the fiber is collimated by a microscope objective yielding a beam diameter of approximately 4 mm.

After collimation, the excitation light passes into the scanning optics consisting of the train from M1 to L5. Images are generated on a per-pixel basis by raster scanning the beam using the combination of the galvanometer scanning mirrors (M1 and M2) and the relay lenses (L1 to L3). Excitation light then passes through the scan lenses (L4 and L5) and is relayed to the stage. The resulting sample fluorescence is descanned to the pinhole aperture and ultimately to the detectors for intensity and anisotropy imaging. Implementation of confocal fluorescence spectroscopy is accomplished by flipping a mirror (FM) into the detection path downstream of the dichroic mirror (DM1) that separates the fluorescence from backscattered excitation light. Following a scheme implemented in a non-imaging context by Richards-Kortum *et al.* [7], fluorescence is reflected toward and focused by lens L6 into the 50 μm core of a multimode fiber, which serves as the confocal aperture. The output of this fiber is lens-coupled to the entrance of a grating spectrograph and dispersed onto a cooled CCD that gives approximately 340 nm of spectral coverage.
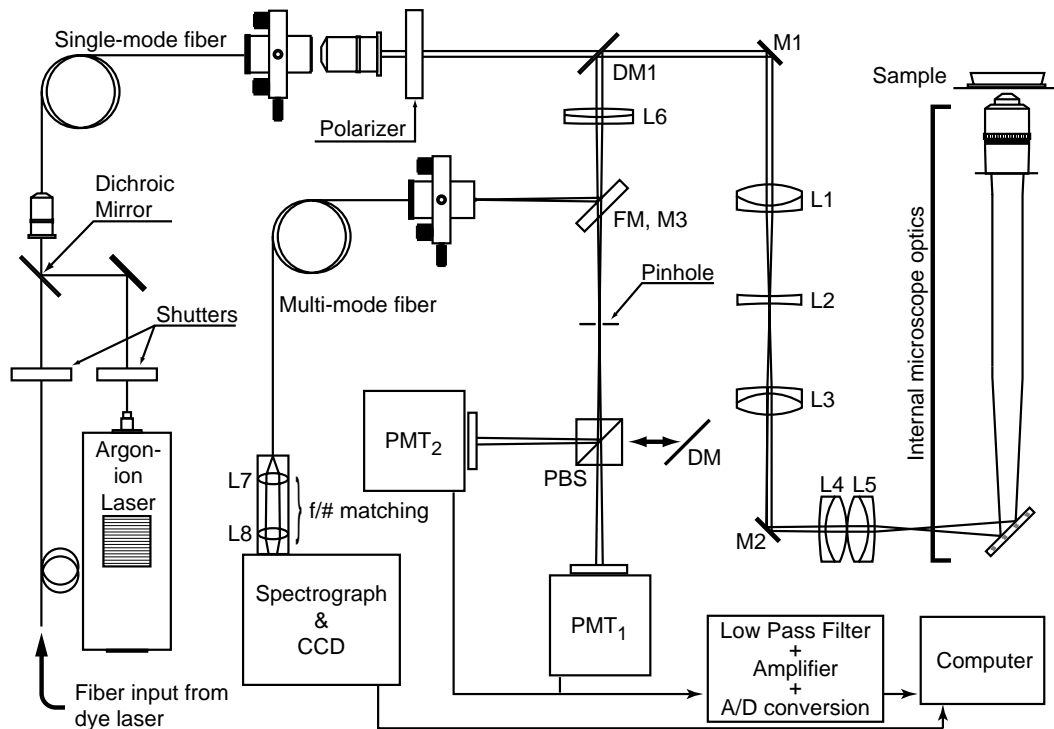
Figure 2.1: Confocal fluorescence spectroscopy and anisotropy imaging system. For spectroscopy, mirror FM is flipped into the detection path. Sample fluorescence is descanned, reflected by dichroic mirror DM1, and focused by lens L6 into the 50 μm core of a multi-mode fiber acting as the confocal limiting aperture. Fiber output is imaged through a grating spectrograph onto a cooled CCD. For polarization-sensitive imaging, a polarizing beam splitting cube (PBS) is placed in the detection path post-pinhole. Fluorescence parallel and perpendicular to the polarized excitation beam is directed simultaneously to two balanced photomultiplier tubes (PMT$_1$, PMT$_2$). For conventional simultaneous two-color fluorescence imaging, a dichroic mirror (DM) replaces PBS.

Component	Description	Model number	Manufacturer
Single-mode fiber	Step index patch cable (single mode, 488/514 nm)	F-SA-C	Newport
Polarizer	Linear sheet polarizer	5511	New Focus
FM	Flip-up mirror mount	9891	New Focus
M3	Spectroscopy mirror	10D510.ER2	Newport
Multi-mode fiber	Step index patch cable (50 μm core diameter)	M14L05	Thorlabs
L7	F-matching collimating lens ($f = 30$ mm, 25 mm diam.)	L45-211	Edmund Scientific
L8	F-matching focusing lens ($f = 60$ mm, 25 mm diam.)	L32-724	Edmund Scientific
Spectrograph	1/4 m imaging spectrograph	MS260i	Oriel
CCD	Back illuminated CCD	DU420-BV	Andor
PBS	Polarizing beamsplitter cube	5811	New Focus
DM	Dichroic mirror	various	Chroma
$PMT_{1,2}$	Photomultiplier tubes	HC120-07MOD (R6357 tube)	Hamamatsu

Table 2.2: Parts list for confocal attachments enabling two-color imaging, fluorescence polarization imaging, and fluorescence spectroscopy.

In order to match the f-number ($f/\#$) of the optical fiber ($f/2.3$) to that of the spectrograph ($f/3.9$), the $f/\#$ matcher indicated in Figure 2.1 is required. Without this addition the spectroscopy setup experiences unacceptable amounts of stray light reaching the detector plane as the fiber overfills the spectrograph acceptance angle. The matcher consists of two lenses in a light-tight tube that increase the $f/\#$ by a factor of two by collimating with lens L7 and focusing onto the spectrograph input slit with lens L8. Lens L8 has a focal length that is twice that of L7, thus yielding a two-fold $f/\#$ increase from $f/2.3$ to $f/4.6$. This results in a slight underfill of the spectrograph optics yielding excellent results with minimal stray light and an increase in throughput over the overfilled case. A consequence of the change in $f/\#$ is a decrease in spectral resolution, however. Since etendue is conserved passing through the $f/\#$ matching optics, the lowering of the divergence angle by a factor of two must be accompanied by a matched increase in magnification [8]. The image of the 50 μm fiber on the spectrograph slit must therefore be 100 μm. In order to allow all of the input light to pass into the spectrograph, this increase in size also requires that the input slit be set to at least 100 μm. In practice this does not cause any problems acquiring spectra since the resulting 3 nm resolution (FWHM) is still much narrower than the spectral width of typical fluorophores encountered in our research.

Dual-color imaging is implemented by placing a dichroic mirror (DM) after the pinhole between the two PMTs. The beam divergence after the pinhole is approximately 0.5°, which yields an insignificant spectral shift for measurements on the spectrally broad fluorophores that we typically use. With the dichroic in place, PMT_2 typically measures the short wavelength reflected light while PMT_1 detects

the long-wavelength fluorescence. This setup has been used quite successfully with multiply-labelled samples with acceptable amounts of spectral bleed-through.

Fluorescence anisotropy imaging is implemented by placing a linear polarizer in the excitation beam (Polarizer) and a corresponding polarizing beamsplitter cube (PBS) just after the pinhole. The 3.5° half acceptance angle of the cube readily accomodates the relatively small divergence of the post-pinhole beam. With the simultaneous detection of orthogonal polarizations in place in this manner, anisotropy images are readily acquired by post-processing of the images on a per-pixel basis as described later in Chapter 5.

2.3 Verification of spectroscopy and anisotropy capabilities

2.3.1 Validation of confocal fluorescence spectroscopy

The axial sectioning capability of the confocal spectroscopy system is illustrated in Figure 2.2. A fluorescein solution was placed in a cover slip dish on the stage of the inverted microscope (see Figure 2.1). A 2-mm-diameter polystyrene rod embedded with a red fluorophore (Turner Designs, Inc., Sunnyvale, CA) was fixed on a micropositioning device and lowered into the solution to a depth of approximately 50 μm above the cover slip surface, establishing an interface separating two distinct emission spectra. A series of fluorescence spectra was acquired ($\lambda_{ex} = 488$ nm) as a 10×, 0.5 NA objective was scanned axially from the bottom of the fluid solution up into the fluorescent rod. The sharp spectral transition

into the rod is shown in Figure 2.2A. Fluorescence edge responses extracted from the series of axially-resolved spectra are shown in Figure 2.2B. These signal intensities *vs.* axial position are from single pixels along the wavelength axis of the CCD corresponding to 516 and 599 nm. The dotted line shows the proximal and distal edge responses of the fluorescein solution (516 nm), with the distal edge determined by the polymer rod. Derivatives of these responses give FWHM measures of the axial resolution equal to 4.5 and 5.1 μm, respectively. In the axial regions corresponding to the solution, the approximately constant signal arises from the long wavelength tail of the fluorescein emission. The edge response from the surface of the polymer rod gives an axial resolution of 4.0 μm. Attenuation of the 599 nm signal with increasing depth into the rod arises from inner filtering as evidenced by depth-dependent spectral distortion (not shown).

2.3.2   Validation of fluorescence anisotropy imaging

Effects of image depth and field of view on anisotropy

An experiment was performed to check the fidelity of the anisotropy across the entire field of view and as a function of depth into a sample. This test was performed with the 10$\times$ (0.5 NA) and 20$\times$ (0.75 NA) objectives imaging a homogeneous solution of 4 μg/mL fluorescein in a 1:1 mixture of water and glycerol. With both objectives we used a 400 $\times$ 400 μm field of view divided into a 500 $\times$ 500 pixel array. An initial image was acquired just inside the coverslip, and subsequent images were acquired every 30 μm axially into the solution.

The results of the two validation experiments are shown in Fig. 2.3. Figure 2.3A shows the depth dependence of the measured value of r in the center and at
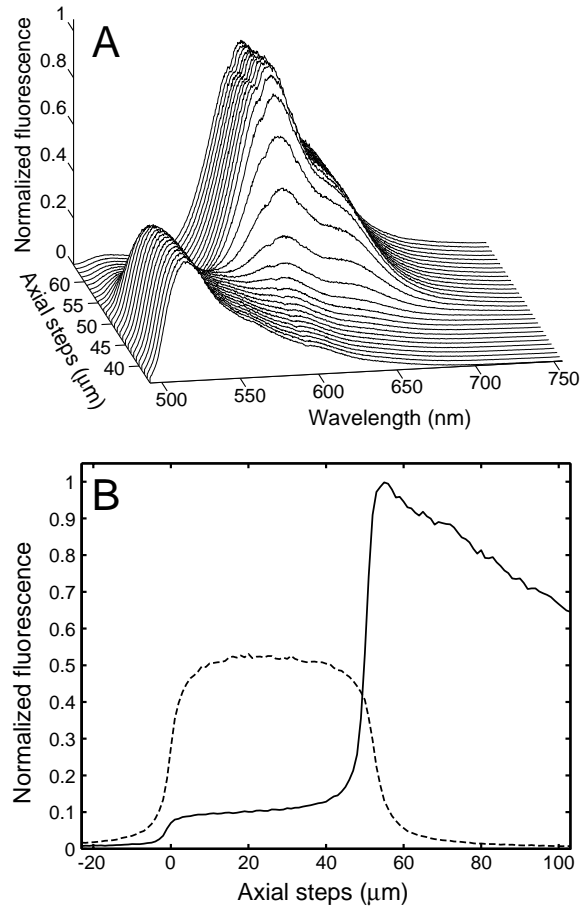
Figure 2.2: Validation of confocal fluorescence spectroscopy. A red fluorophore-embedded poly-mer rod was lowered into fluorescein solution in a cover slip dish. Fluorescence spectra were acquired as the focus was advanced axially from the cover slip through the fluid solution and into the bottom of the rod. (A) shows the sequence of individual fluorescence spectra *vs.* depth into the sample. In (B) the wavelength-resolved (516 and 599 nm) fluorescence edge responses are plotted for the fluorescein in solution (dotted line) and for the fluorophore-embedded polymer rod (solid line). Derivatives of these edge responses yield axial resolutions of 4.0 - 5.1 μm.

the edge of the field of view for two objectives. Both on- and off-axis the objectives perform well at depth, with a maximum error of only 7% in the anisotropy for the off-axis case with the 10× objective at a depth of 210 μm. Although it has the higher NA, the 20× Plan Apo objective performed better than the 10× Fluor objective, possibly due to a higher level of correction for optical aberrations.

Effects of numerical aperture on anisotropy accuracy

It was important to measure r for all of our objectives to account for the depolarizing effects of high numerical apertures, which can yield artificially low anisotropy values [9, 10]. We ensured that our confocal microscope was reporting accurate values for anisotropy by measuring reference standards on our microscope and comparing the anisotropy values to those obtained from a commercial fluorometer (AMINCO-Bowman Series 2 Luminescence Spectrometer, Thermo Spectronic, Madison, WI). Reference standards were prepared by making a series of 1 μg/mL fluorescein solutions in a mix of water and glycerol ranging from 100% water to 25/75% water/glycerol. Measurements were made with microscope objectives spanning the entire NA range available coupled with appropriate pinhole sizes. These included 4× (0.13 NA), 10× (0.5 NA), 20× (0.75 NA), and 60× (1.4 NA) objectives.

Fig. 2.3B shows the results of the experiments comparing the confocal microscope to values measured on a commercial fluorometer. The 4×, 10×, and 20× objectives all performed well and returned anisotropies that agreed with the fluorometer measurements. Anisotropy was systematically underestimated with the 60×, 1.4 NA objective as a result of its extremely high numerical aperture
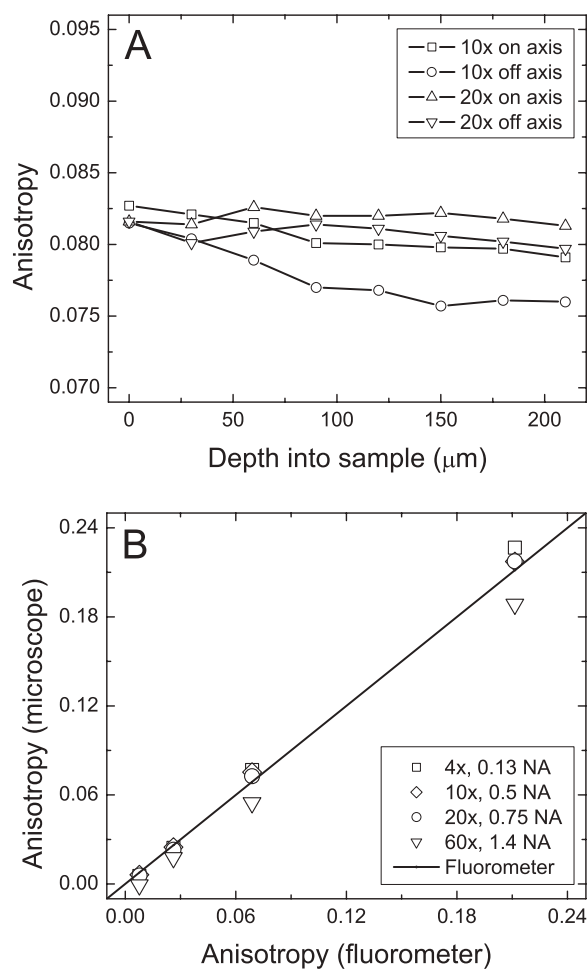
Figure 2.3: Effects of objective numerical aperture, image depth, and field of view on anisotropy measurements in homogeneous solution. (A) Measured fluorescein anisotropies with $10\times$, 0.5 NA and $20\times$, 0.75 NA objectives on and off the optical axis at various depths into a fluid sample. The effect on anisotropy was small in all cases with a maximum error of approximately 7% for the $10\times$ objective off-axis at 210 μm into the sample. (B) The effect of NA on the anisotropy measured just inside the coverslip with the microscope vs. fluorometer measurements of the same samples. All objectives up to NA 0.75 performed well, while the 1.4 NA oil immersion objective returned values systematically low as compared to the fluorometer and lower NA objectives. The four samples corresponded to 100/0, 75/25, 50/50, and 25/75% water/glycerol.

[9]. Typically the $10\times$ objective is used, as the anisotropies it returns at all glycerol concentrations are statistically indistinguishable from those measured on the fluorometer.

The results presented in Figure 2.3 place some limits on the applicability of high numerical apertures for fluorescence polarization imaging. Constraints imposed on objective lens numerical aperture by depolarization necessarily limit the available optical resolution. In our case, we were able to use a 0.75 NA objective with no detectable anisotropy degradation. This NA yields a lateral resolution of approximately 0.3 μm and an axial resolution of approximately 1.7 μm. It is possible that an even higher NA would have yielded accurate anisotropies, but we did not evaluate objectives with numerical apertures between 0.75 and 1.4.

Signal-to-noise evaluation

The effect of detector signal-to-noise ratio (SNR) on the uncertainty of anisotropy measurements was quantified by acquiring images in a 1:1 mixture of water to glycerol solution containing 4 μg/mL fluorescein. All images were 400×400 μm square fields of view with 500 pixels per axis acquired with the $10\times$, 0.5 NA microscope objective. To achieve a range of intensities in the fluorescence output, the laser source was attenuated with neutral density filters. Mean anisotropy and a histogram of anisotropies in a region of interest were acquired for each laser power. The effects of SNR on the measured anisotropy are shown in Figure 2.4. Figure 2.4A shows three representative examples from a series of anisotropy histograms. Histograms were derived from a 45 μm square region of interest (56×56 pixels) in the center of the 400 μm field of view as the excitation intensity was varied.
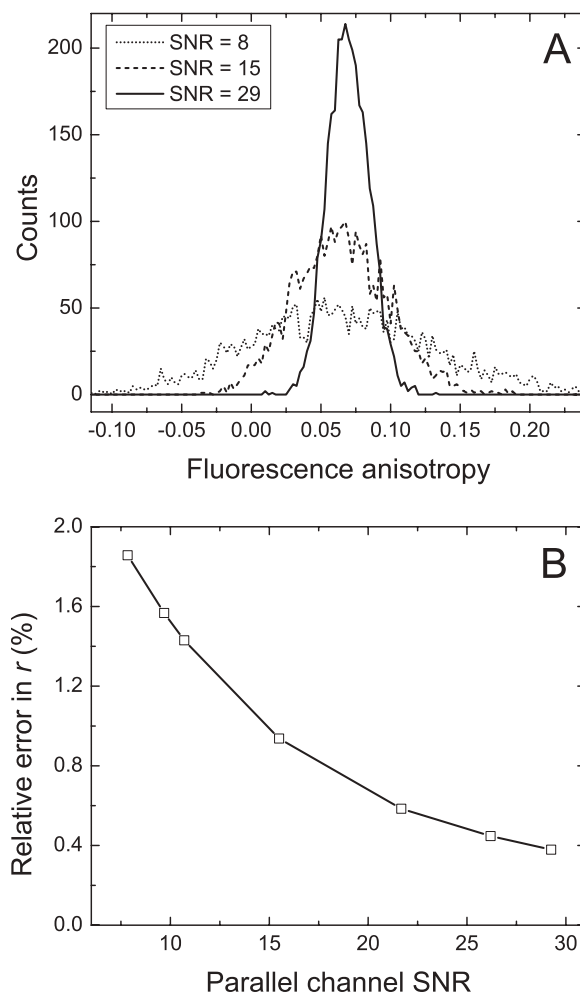
Figure 2.4: Uncertainty in anisotropy measurements as a function of signal-to-noise ratio. (A) The effect of detector SNR on histograms of anisotropy from a solution of 50/50 water/glycerol containing 4 μg/mL fluorescein. Histograms of anisotropy acquired from 45 μm square regions of interest in the center of the field are shown for three values of the parallel channel SNR. (B) The relative error in the same regions of interest as a function of the parallel polarization channel intensity SNR. Relative error is defined as the ratio of the standard error of the mean to the measured r value.

Changing the excitation intensity altered the intensity SNR in the photomultiplier tubes and therefore the width of the measured anisotropy distribution. Histograms are distributed about the mean value of $r = 0.07$ with high intensities giving narrower distributions and low intensities wider distributions. A summary of the influence of excitation intensity on the width of the anisotropy histograms is shown in Figure 2.4B, where the relative error in the anisotropy measurement is plotted *vs.* the intensity SNR of the parallel polarization channel. The relative error in this case was defined to be the ratio of the standard error of the histogram (Δr) to the mean of the anisotropy distribution (*i.e.* $\Delta r/r$). We chose standard error in this case because our ability to determine the mean anisotropy was the important measure in this example. The maximum relative error we observed ranged from under 2% for a SNR of 8 to less than 0.4% for a SNR of 29. Measurements were made for lower signals, but at these low intensities system-specific noise artifacts dominate. This effect arises from PMT_1 exhibiting slightly more noise than PMT_2, leading to artificially low anisotropies at low intensities.

2.4 Applications of multi-modality imaging

Photosensitizer photobleaching in multicell tumor spheroids

As mentioned earlier, one of the motivations for adding confocal fluorescence spectroscopy capabilities was the need to study photosensitizers that generate fluorescent photoproducts upon exposure to light. One such example is protoporphyrin IX (PpIX), an endogenous photodynamic therapy (PDT) agent that is produced in cells in excess *via* addition of the prodrug aminolevulinic acid (ALA) or one of

its esterified derivatives [11, 12]. Our group has shown that PpIX photobleaching is irradiance dependent *in vivo* in normal rat skin [13], but in order to test the bleaching mechanisms more rigorously we can use the multicellular tumor spheroid model. This model allows us to set up PDT-induced oxygen gradients in spheroids that mimic the effects of different fluence rates without the need for additional exposure time to reach the same total fluence. This decouples the oxygen dependence from any time-dependent build up of photoproducts. We therefore undertook a pilot study to quantify the effects of oxygen availability on the accumulation of fluorescent photoproducts in ALA-PDT.

A representative example image acquired with the $10\times$, 0.5 NA objective and marked with regions of spectroscopic acquisition appears in Figure 2.5. Three spectra are presented that show the results of PDT on an EMT6 multicell tumor spheroid incubated with 0.05 mM aminolevulinic acid hexylester (h-ALA) for 3 hours in serum-free media. This incubation concentration is informed by previous studies, and it was chosen because it results in a nearly uniform distribution of PpIX throughout the spheroid [14]. Spectral fitting was performed using a singular value decomposition algorithm developed in our group and covered in detail in the *in vivo* photobleaching paper of Finlay *et al.* [13]. Data were fit with basis spectra for PpIX, uroporphyrin, coproporphyrin, two photoproducts modeled as gaussians (photoproducts I & II), and 61 fourier terms to fit sections of the data not accounted for by the aforementioned basis spectra. The pre-PDT spectrum of PpIX is shown, as are spectra from the spheroid interior and periphery after PDT. A clear radial dependence to the photobleaching and photoproduct formation is observed when comparing the interior to peripheral spectra after PDT. The
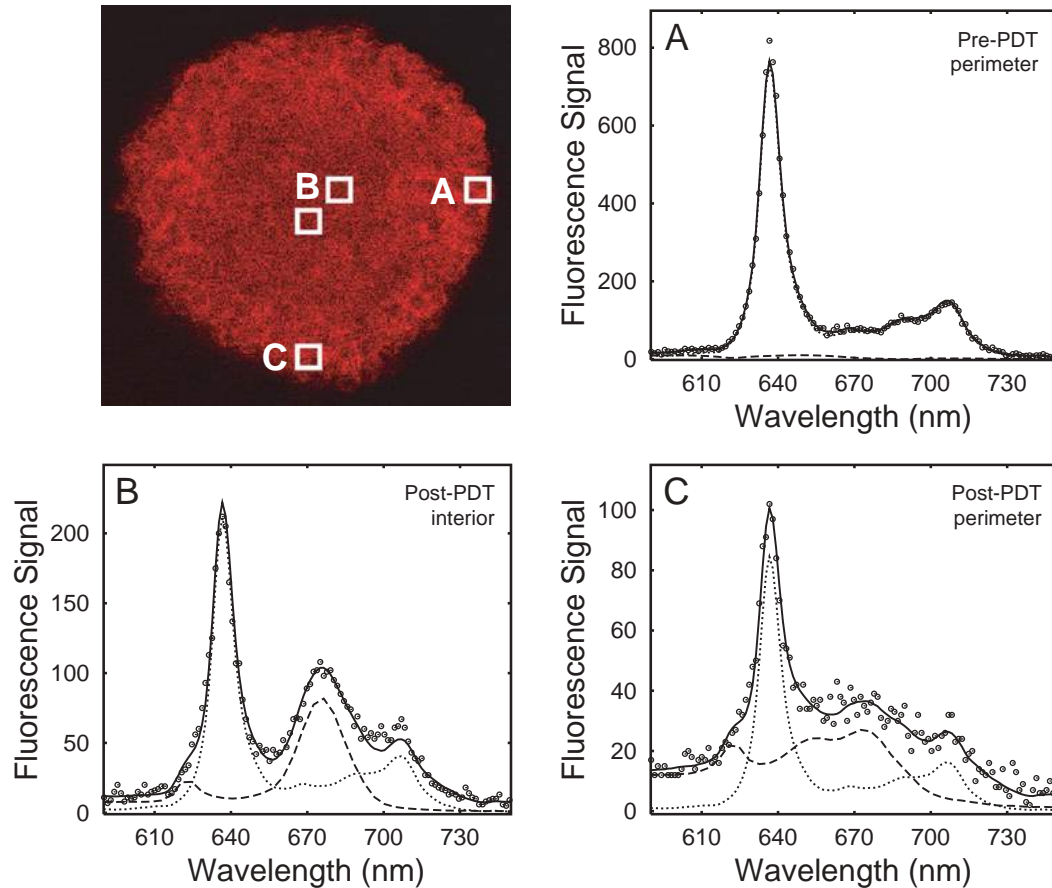
Figure 2.5: Photobleaching of PpIX in a 0.05 mM h-ALA-incubated EMT6 multicell tumor spheroid before and after PDT. $20\times 20\times 4$ μm regions of spectral acquisition are indicated in the spheroid image, and the corresponding spectra from 0.5 second integrations are shown. Raw data ($\odot$) and spectral fits (solid line) from our singular-value-decomposition-based fitting algorithm are shown on the plots. Contributions from PpIX (dotted line) as well as contributions from the sum of autofluorescence, uroporphyrin, coproporphyrin, and two photoproducts (dashed line) are plotted. Spatially dependent PpIX bleaching and photoproduct formation apparent from spectral analysis is consistent with different regimes of oxygen availability induced by PDT. Treatment and imaging were both performed with 514 nm light. Spheroid was treated with a fluence rate of 200 mW/cm^2 (60 J/cm^2).

spheroid interior exhibits appreciable accumulation of primarily photoproduct I, and the PpIX fluorescence decreases by about a factor of 4 compared to initial values. Spheroid peripheral regions exhibit appreciable accumulation of both photoproducts, and the PpIX fluorescence is a factor of 2 lower than in the interior. These results are consistent with a $^1O_2$-mediated bleaching mechanism and different degrees of oxygen dependence in the accumulation of the two photoproducts. In the normal rat skin, higher irradiances led to greater accumulation of photoproduct I and less PpIX photobleaching, analogous to the spheroid interior. The spheroid periphery matches well with the results in rat skin at low irradiances, as the spheroid exterior has more access to oxygen just as the tissue exposed to a lower fluence rate tends to preserve the local oxygen concentration. Future studies are needed to examine the similarities in detail, but this pilot experiment matches well with the *in vivo* data and motivates further study.

Dual-color imaging of GFP and mTHPC

In order to demonstrate the capabilities of the system to simultaneously detect two fluorophores, we imaged green fluorescent protein (GFP) expressing EMT6 cells that had been incubated overnight in 5 μg/mL of the PDT drug meta-tetrahydroxyphenylchlorin (mTHPC). Images were acquired with a 488 nm excitation wavelength, and the emission of the GFP (λ_{peak} =510 nm) and mTHPC (λ_{peak} =655 nm) were easily separated with a 560dcxr dichroic mirror (Chroma, Rockingham, VT) as shown in Figure 2.6. With appropriate choices of filters and an additional detector, this setup could be readily modified to allow 3 or more simultaneous colors.
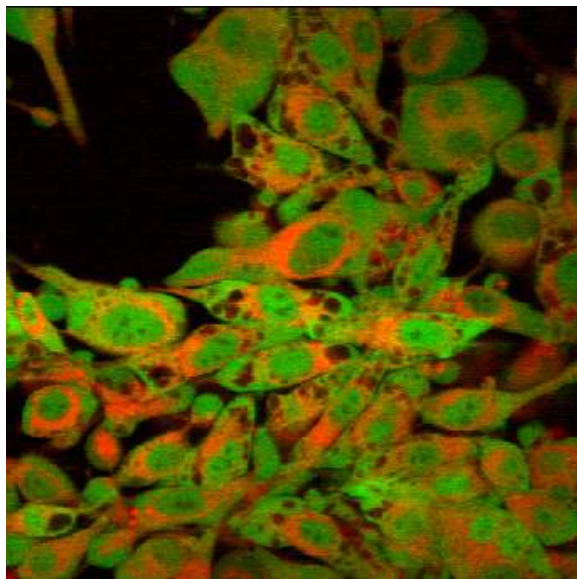
Figure 2.6: Simultaneous dual-color confocal imaging of GFP-expressing EMT6 cells incubated with 5 μg/mL mTHPC overnight. GFP signal is displayed in green while mTHPC is shown in red. The image was acquired over a 200 μm field of view distributed into a 500$\times$ 500 pixel array with a 20$\times$, 0.75 NA objective. In this case, the dichroic mirror (DM) used was a 560dcxr from Chroma.

Anisotropy images of GFP-expressing cells

In order to establish the fluorescence anisotropy in the GFP-expressing EMT6 cells, a cell monolayer was imaged simultaneously in both polarization channels, and anisotropy and intensity images were acquired. The result of that set of images is shown in Figure 2.7. The GFP anisotropy we recover from the images ($r \sim 0.3$) agrees with the values of 0.275-0.325 reported in the literature [15–17].
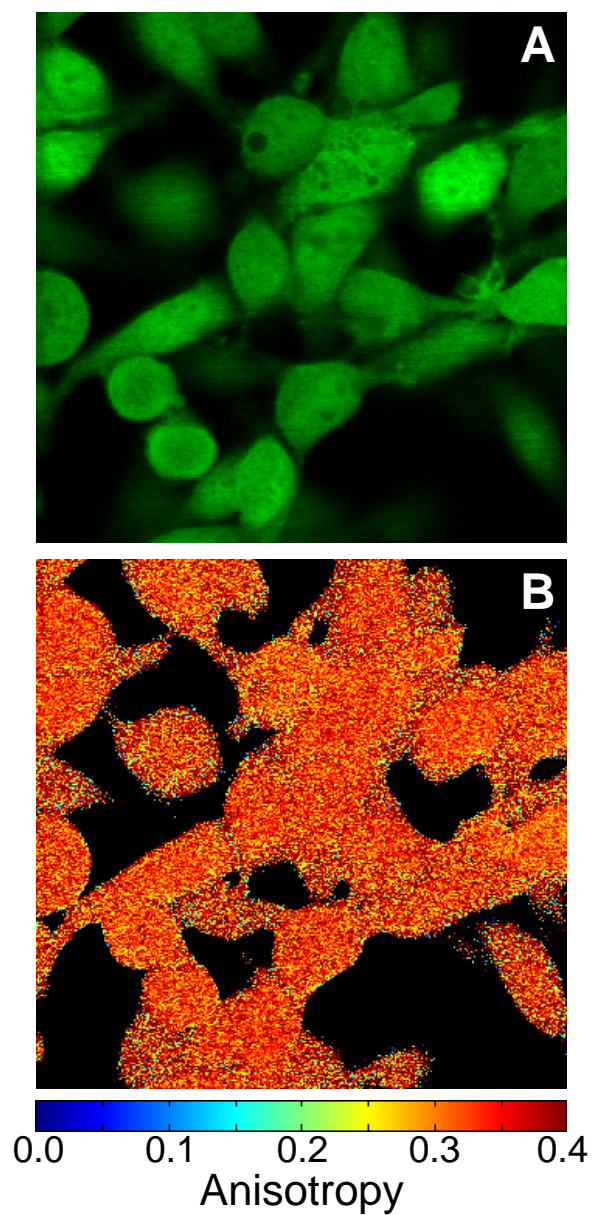
Figure 2.7: Intensity (A) and anisotropy (B) confocal images of a 100 μm field of view containing a GFP expressing EMT6 cell monolayer. Anisotropy is quite constant throughout the entire cell ($r \sim 0.3$) and agrees with published values in the literature.

References

[1] I. Georgakoudi, Ph.D. thesis, University of Rochester, 1998.

[2] C. E. Bigelow, C. J. Harkrider, D. L. Conover, T. H. Foster, I. Georgakoudi, S. Mitra, M. G. Nichols, and M. Rajadhyaksha, "Retrofitted confocal laser scanner for a commercial inverted fluorescence microscope," Rev. Sci. Instrum. **72,** 3407–3410 (2001).

[3] S. Mitra, Ph.D. thesis, University of Rochester, 2004.

[4] J. C. Finlay, S. Mitra, M. S. Patterson, and T. H. Foster, "Photobleaching kinetics of Photofrin *in vivo* and in multicell tumour spheroids indicate two simultaneous bleaching mechanisms," Phys. Med. Biol. **49,** 4837–4860 (2004).

[5] C. E. Bigelow, H. D. Vishwasrao, J. G. Frelinger, and T. H. Foster, "Imaging enzyme activity with polarization-sensitive confocal fluorescence microscopy," J. Microsc. **215,** 24–33 (2004).

[6] C. E. Bigelow, D. L. Conover, and T. H. Foster, "Confocal fluorescence spectroscopy and anisotropy imaging system," Opt. Lett. **28,** 695–697 (2003).

[7] R. Richards-Kortum, A. Durkin, and J. Zeng, "Description and performance of a fiber-optic confocal fluorescence spectrometer," Appl. Spectrosc. **48,** 350–355 (1994).

[8] J. Lerner and A. Thevenon, "The optics of spectroscopy," Technical report, Jobin Yvon Optical Systems (1988) .

[9] D. Axelrod, "Fluorescence polarization microscopy," Methods Cell Biol. **30,** 333–352 (1989).

[10] B. Richards and E. Wolf, "Electromagnetic diffraction in optical systems II. Structure of the image field in an aplanatic system," Proc. R. Soc. Lon. Ser. A **253,** 358–379 (1959).

[11] Q. Peng, K. Berg, J. Moan, M. Kongshaug, and J. Nesland, "5-aminolevulinic acid-based photodynamic therapy: principles and experimental research," Photochem. Photobiol. **65,** 235–251 (1997).

[12] Q. Peng, J. Moan, T. Warloe, V. Iani, H. B. Steen, A. Bjørseth, and J. M. Nesland, "Build-up of esterified aminolevulinic-acid-derivative-induced porphyrin fluorescence in normal mouse skin," J. Photochem. Photobiol. B: Biol. **34,** 95–96 (1996).

[13] J. C. Finlay, D. L. Conover, E. L. Hull, and T. H. Foster, "Porphyrin bleaching and PDT-induced spectral changes are irradiance dependent in ALA-sensitized normal rat skin *in vivo*," Photochem. Photobiol. **73,** 54–63 (2001).

[14] C. E. Bigelow, S. Mitra, R. Knuechel, and T. H. Foster, "ALA- and ALA-hexylester-induced protoporphyrin IX fluorescence and distribution in multi-cell tumour spheroids," Br. J. Cancer **85,** 727–734 (2001).

[15] A. Knight, N. Goddard, P. Fielden, M. Barker, N. Billinton, and R. Walmsley, "Fluorescence polarisation of green fluorescent protein (GFP). A strategy for improved wavelength discrimination for GFP determinations," Anal. Commun. **36,** 113–117 (1999).

[16] A. Knight, N. Goddard, N. Billinton, P. Cahill, and R. Walmsley, "Fluorescence polarization discriminates green fluorescent protein from interfering autofluorescence in a microplate assay for genotoxicity," J. Biochem. Biophys. Methods **51,** 165–177 (2002).

[17] R. Swaminathan, C. Hoang, and A. Verkman, "Photobleaching recovery and anisotropy decay of green fluorescent protein GFP-S65T in solution and cells: cytoplasmic viscosity probed by green fluorescent protein translational and rotational diffusion," Biophys. J. **72,** 1900–1907 (1997).

Chapter 3

Monte Carlo Routine for Modeling Fluorescence Polarization Imaging

3.1 Introduction

As shown in Chapter 1, there has been a large body of work devoted to determining the optical performance of confocal microscopes. For samples that are thin and for which scattering can be neglected, imaging is described well by electromagnetic theory in the form of Fourier optics [1, 2]. Confocal microscopy is also useful for imaging thick biological samples for which scattering cannot be neglected and in which it is difficult to model optical performance. In this case it is no longer useful to consider point spread functions in the traditional sense that depend only on the optics. In turbid media the sample becomes an integral part of the optical train, and its effect on the point spread function must be accounted for when analyzing the system [3].

Confocal microscopy in turbid media forms images from both unscattered (bal-

listic) light and light that has experienced scattering [4]. Since modeling imaging in this regime is very difficult and requires alternatives to closed form solutions, hybrid Monte Carlo routines have been developed. These models use electromagnetic theory (Mie scattering) or the Henyey-Greenstein phase function [5] to simulate single scattering events as if they were completely independent. Photon propagation, however, relies on bulk tissue optical properties.

Monte Carlo methods have been applied to confocal microscopy in turbid media since their introduction in the context of reflection imaging by Schmitt *et al.* [4]. In the years following, the simulations have seen progressive evolution in complexity and efficiency. Schmitt & Ben-Letaief increased the efficiency by introducing several variance reduction techniques [6]. Simulation efficiency is always important in Monte Carlo routines, but in the case of confocal microscopy the situation is exacerbated by the fact that the vast majority of photons that reach the tissue surface do not pass through the pinhole and are therefore not detected. Other routines have been developed to examine depth penetration limits [7], effects of number of scattering events on image resolution [8], and to quantify the effects of polarization state on confocal imaging [9–12]. Several authors have extended the technique further to include confocal fluorescence imaging by performing simulations with optical properties at two wavelengths corresponding to the excitation and fluorophore emission [13–17]. In an attempt to extend the utility of the approach further, Daria *et al.* have developed an approach that preserves some of the wavefront information by combining wave and particle properties in the propagating photon packets [18].

The Monte Carlo approach described here extends the capability of these

methods to include the generation and tracking of polarized fluorescence. Enabling fluorescence polarization capability requires a much more thorough model of fluorescence generation than previously used. It requires sampling of elliptically polarized excitation light, incorporating fluorescence lifetime and rotational Brownian motion, and sampling dipole radiation for fluorescence emission. This additional complexity allows the exploration of the effects of multiply scattered light on confocal fluorescence polarization images and helps indicate the optical countermeasures useful for maximum polarization preservation.

3.1.1 Introduction to Monte Carlo methods

The fundamental algorithm of Monte Carlo simulations samples a random variable representing a physical phenomenon, s, by mapping its statistical distribution into a uniformly distributed random number, ξ [19]. In the case of tissue optics with fluorescence polarization, the random variable sampled is typically a quantity such as photon step length between scattering events, fluorescence lifetime, scattering angle, or polarization azimuthal angle.

Knowledge of the probability density functions (PDFs) for each of the physical parameters of interest makes sampling possible. The probability density function for s, $p(s)$, is defined over an interval such that

$$\int_a^b p(s)\, ds = 1. \tag{3.1}$$

By integrating $p(s)$ over an arbitrary interval (a, s_1) the cumulative distribution

function (CDF),

$$P\{a \leq s \leq s_1\} = \int_a^{s_1} p(s)\, ds, \tag{3.2}$$

gives the probability that s lies between a and s_1. By equating the CDFs for s and ξ according to

$$P\{a \leq s \leq s_1\} = P\{0 \leq \xi \leq \xi_1\}, \tag{3.3}$$

s is mapped into ξ and can therefore be numerically sampled with a random number generator. For a uniformly distributed random number on the interval $(0,\ 1)$, $P\{0 \leq \xi \leq \xi_1\} = \xi_1$ and consequently

$$\int_a^{s_1} p(s)\, ds = \xi_1. \tag{3.4}$$

By solving this for a function such that $s_1 = f(\xi_1)$, the probability distribution function for the physical variable of interest can be sampled computationally with ξ_1. In cases for which the solution to equation 3.4 is not invertible or execution of the solution is unacceptably slow, the use of pre-calculated lookup tables is possible. In the routines presented here, this approach is used for most events other than simple photon propagation. Details of this approach are given later in the chapter, and an example of the technique is shown graphically in Figure 3.3.

3.2   Fluorescence polarization Monte Carlo

We have developed a Monte Carlo routine for modeling the propagation and generation of polarized light in turbid media including generation of polarized flu-

orescence in multi-layered turbid media (FPML). Our approach for generating fluorescence is similar to one presented by Harvey & Cheung for time-resolved fluorescence depolarization, but the method they used is not relevant to our simulations [20]. The overall structure of the code is modeled after the well known multi-layered Monte Carlo routine MCML, and all relevant photon transport and variance reduction techniques used in MCML were applied to FPML [21]. Routines for sampling common quantities such as photon step path length and scattering are all outlined in an excellent review by Prahl *et al.* [22] and will therefore not be covered in detail here.

3.2.1   Model confocal microscope

Modeling confocal microscopy requires combining geometrical optics ray tracing with Monte Carlo tissue optics routines. Since the system presented here requires high numerical aperture objectives as well as polarization ray tracing, a model confocal microscope has been assembled in OSLO® (Lambda Research Corporation). The system is used to propagate photons from the polarized excitation source to the tissue interface as well as to collect photons exiting the tissue surface and trace them to the pinhole plane. Photon packets are launched into the system by uniformly illuminating the pupil of the objective lens and tracking their positions to the coverslip-tissue interface. Photons exiting the tissue are traced through the microscope optics to determine those that pass though the pinhole.

Our confocal system is modeled after the setup described by Schmitt & Ben-Letaief [6]. It consists of two lenses arranged to form a $4f$ system with unit magnification from the sample to the pinhole plane as shown in Figure 3.1. Glass
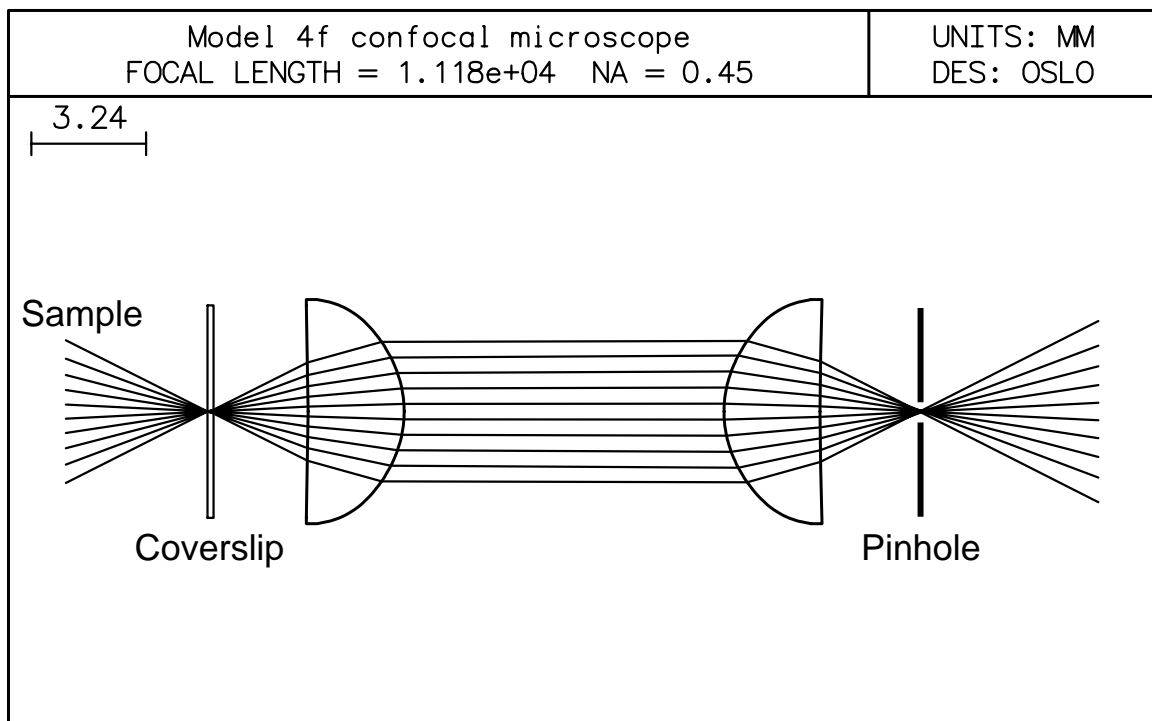
Figure 3.1: Model confocal microscope setup from OSLO®. The system consists of two Kodak A438 aspheric lenses separated by two times the focal length to yield a $4f$ optical setup. Light originates from the Monte Carlo simulation at the far left side of the coverslip and is traced through the optical system to the pinhole.

aspheric lenses were chosen (A438, Eastman Kodak Company, Rochester, NY) to minimize spherical aberration for physically realizable microscopy spot sizes without necessitating detailed knowledge of the construction of a particular microscope objective. A 170 μm thick coverslip is added as is a pinhole aperture at the back focal plane of one of the lenses.

3.2.2 Propagating polarized light

Propagation of polarized photon packets is accomplished using the Mueller-Stokes formalism, wherein light polarization is described by Stokes vectors and events that modify the polarization state are described by Mueller matrices [23]. The Stokes vector after an event, S_{output}, is given by the product of the Mueller matrix, M, and the incoming Stokes vector, S_{input}, according to

$$S_{output} = M \cdot S_{input}. \tag{3.5}$$

Stokes vectors are 4-element matrices defined as

$$S = \begin{bmatrix} I \\ Q \\ U \\ V \end{bmatrix}, \tag{3.6}$$

where the terms I, Q, U, and V are measurable quantities based on intensities in two orthogonal polarization channels. A description of the calculation of each of these parameters is given in Appendix A.

Interactions that modify the polarization state are given by their 4×4 Mueller matrices in the form

$$M = \begin{bmatrix} m_{11} & m_{12} & m_{13} & m_{14} \\ m_{21} & m_{22} & m_{23} & m_{24} \\ m_{31} & m_{32} & m_{33} & m_{34} \\ m_{41} & m_{42} & m_{43} & m_{44} \end{bmatrix}. \tag{3.7}$$

Mueller matrices can represent optical elements such as lenses, polarizers, and waveplates, but in the context of this simulation they describe the passage of light through interfaces and the modification of polarization due to scattering.

Tracking the local coordinate system

Typically in Monte Carlo routines for tissue optics, the position, weight, and direction cosines of a photon packet are sufficient to completely describe propagation. Modeling polarization effects additionally requires the orientation of the local coordinate system (x,y,z) that follows with the propagating photon packets relative to the global coordinate system (X,Y,Z) in which the optical system is oriented. Stokes vectors are always cast in terms of components parallel and perpendicular to a plane defined by the local coordinate system, so evolution of the polarization state requires knowledge of the orientation of these axes.

FPML quantifies polarization following the approach of Bartel & Hielscher [24] using equations from a text by Ginsberg [25]. Tracking the local coordinate system at each event that modifies the polarization state is accomplished by passing the relevant azimuthal angle, ϕ, and polar angle, θ, to standard rotation matrices.
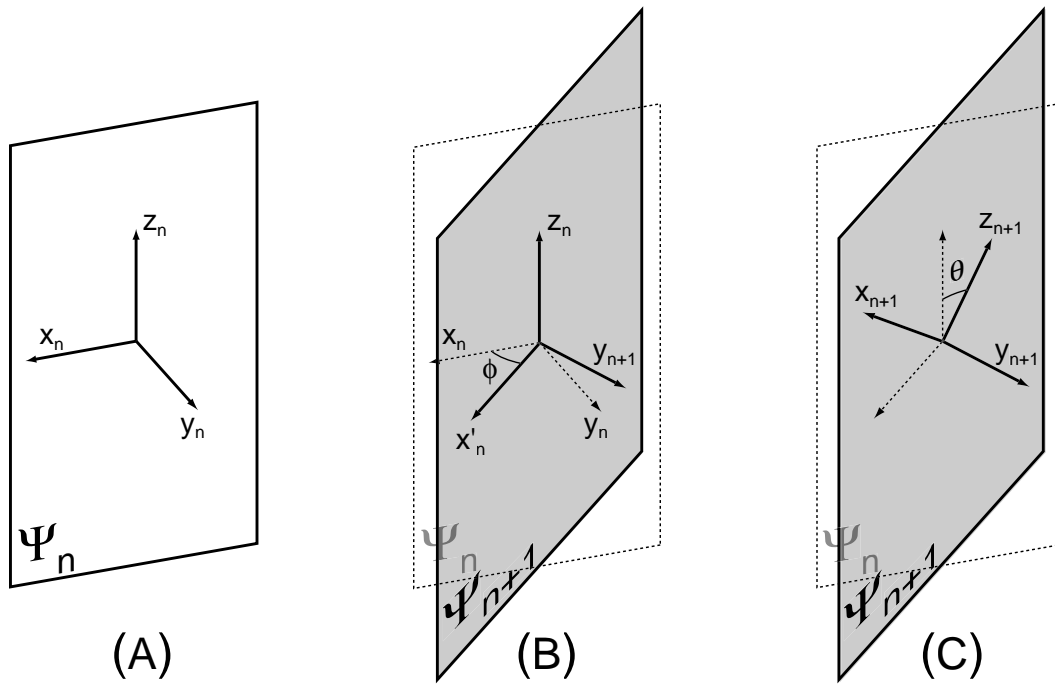
Figure 3.2: Mechanics of body-fixed coordinate system rotation. (A) Light incident on a scattering particle is defined relative to the initial coordinate system (x_n, y_n, z_n) and the scattering plane, Ψ_n, which contains the x_n and z_n axes. (B) An intermediate coordinate system is found by rotating by ϕ about z_n to yield the orientation of the new scattering plane Ψ_{n+1}. (C) The final local coordinate system of the outgoing photon packet $(x_{n+1}, y_{n+1}, z_{n+1})$ is determined by rotating by θ about the y_{n+1} axis.

The rotations presented here are body-fixed, meaning that the first rotation occurs about one axis of the original local coordinate system, and the second rotation occurs about one of the resulting local axes. This process is illustrated graphically in Figure 3.2. Specifically, the axes are always rotated first about the direction of propagation (z axis) by ϕ, and then about the resulting local y axis by θ to give the local coordinate system of the Stokes vector. The standard rotation matrices are given by [25]

$$R_y = R_\theta = \begin{bmatrix} \cos\theta & 0 & -\sin\theta \\ 0 & 1 & 0 \\ \sin\theta & 0 & \cos\theta \end{bmatrix} \text{ and } R_z = R_\phi = \begin{bmatrix} \cos\phi & \sin\phi & 0 \\ -\sin\phi & \cos\phi & 0 \\ 0 & 0 & 1 \end{bmatrix}. \quad (3.8)$$

The rotation matrix that takes the coordinates from pre-scattering to post-scattering for the nth event is acquired by premultiplying R_θ and R_ϕ to give

$$R_n = R_\theta R_\phi = \begin{bmatrix} \cos\theta\cos\phi & \cos\theta\sin\phi & -\sin\theta \\ -\sin\phi & \cos\phi & 0 \\ \sin\theta\cos\phi & \sin\theta\sin\phi & \cos\theta \end{bmatrix}. \quad (3.9)$$

Tracking the polarization coordinate axes proceeds by calculating the rotation matrix for each event and storing it as the photon propagates. Once the photon escapes the tissue, the matrices are premultiplied and the final rotation matrix, R_f, is found according to

$$R_f = R_n R_{n-1} \dots R_2 R_1. \quad (3.10)$$

The transpose of R_f yields the final orientation of the local coordinate system of the photon at the tissue surface with respect to the global coordinate system in which the detector is represented *via* multiplying by the local unit vectors. The global coordinates of the local unit vectors are therefore given by

$$x\,(X, Y, Z) = [R_n]^T \begin{bmatrix} 1 \\ 0 \\ 0 \end{bmatrix} = \begin{bmatrix} \cos\phi \\ \sin\phi \\ 0 \end{bmatrix},$$

$$y\,(X, Y, Z) = [R_n]^T \begin{bmatrix} 0 \\ 1 \\ 0 \end{bmatrix} = \begin{bmatrix} -\sin\phi\cos\theta \\ \cos\theta\cos\phi \\ \sin\theta \end{bmatrix}, \quad \text{and}$$

$$z\,(X, Y, Z) = [R_n]^T \begin{bmatrix} 0 \\ 0 \\ 1 \end{bmatrix} = \begin{bmatrix} \sin\theta\sin\phi \\ -\cos\phi\sin\theta \\ \cos\theta \end{bmatrix}. \tag{3.11}$$

Passage of light through interfaces

Tracking the polarization as photon packets encounter interfaces such as that at the boundary of coverslip and tissue is performed with the Mueller matrix (M) for passage of light through a tilted, planar, dielectric interface. The Mueller matrices

for reflection (M_r) and transmission (M_t) are given by [11, 26]

$$M_r = \frac{1}{2}\left(\frac{\tan(\theta_i - \theta_t)}{\sin(\theta_i + \theta_t)}\right)^2 \begin{bmatrix} a^2 + b^2 & a^2 - b^2 & 0 & 0 \\ a^2 - b^2 & a^2 + b^2 & 0 & 0 \\ 0 & 0 & -2ab & 0 \\ 0 & 0 & 0 & -2ab \end{bmatrix}, \quad (3.12)$$

and

$$M_t = \frac{1}{2}\frac{\sin 2\theta_i \sin 2\theta_t}{(\sin(\theta_i + \theta_t)\cos(\theta_i - \theta_t))^2} \begin{bmatrix} a^2 + 1 & a^2 - 1 & 0 & 0 \\ a^2 - 1 & a^2 + 1 & 0 & 0 \\ 0 & 0 & 2a & 0 \\ 0 & 0 & 0 & 2a \end{bmatrix}, \quad (3.13)$$

where the coefficients in the matrix elements are

$$a = \cos(\theta_i - \theta_t) \qquad \text{and} \qquad b = \cos(\theta_i + \theta_t). \quad (3.14)$$

In Equations 3.12-3.14, θ_i is the angle of incidence in the first medium and θ_t is the refracted angle in the second medium. There are several Mueller matrices for special cases such as total internal reflection and normal incidence that speed up computation, and the forms of these are shown in Appendix B.

Care must be used when applying the matrices in equations 3.12 and 3.13 to a photon packet. The Mueller matrices are derived directly from the Fresnel coefficients, which require decomposition of the incident light into s and p polarization. Valid application of the matrices therefore relies on the incident Stokes vector

being rotated through an azimuthal angle ϕ using the rotation matrix [23]

$$R\left(\phi\right) = \begin{bmatrix} 1 & 0 & 0 & 0 \\ 0 & \cos 2\phi & \sin 2\phi & 0 \\ 0 & -\sin 2\phi & \cos 2\phi & 0 \\ 0 & 0 & 0 & 1 \end{bmatrix}. \tag{3.15}$$

This ensures that the parallel polarization component of the incident photon packet is rotated to align with the plane of incidence. After final passage through the tissue surface, the same rotation matrices are used to align the Stokes vector with the global detector coordinate system.

3.2.3 Modeling the scattering process

The treatment of scattering in Monte Carlo routines for tissue optics has gradually increased in complexity. Raković *et al.* [27] assumed that the polarization state of scattered light was dependent only on the first element of the scattering matrix, $m_{11}(\theta_s)$, and was therefore independent of the azimuthal angle, ϕ_s. Gan *et al.* implemented a hybrid method involving the Henyey-Greenstein distribution and the scattering matrix [10]. Their scattering angle was chosen by sampling the Henyey-Greenstein distribution,

$$p\left(\theta_s\right) = \frac{1 - g^2}{2\left(1 + g^2 - 2g\cos\theta_s\right)^{3/2}} \sin\theta_s. \tag{3.16}$$

The angle acquired from sampling equation 3.16 was used to determine the exact scattering matrix derived from Mie theory. This approach has the benefit of

being fast, but it is approximate in that it generates θ_s from a phenomenological distribution and uses it as an input to determine the polarization state as if the light had been scattered by a sphere. Recently, two approaches have been put forward that simulate light scattering by sampling both θ_s and ϕ_s directly from Mie theory [11, 12, 28]. These assume that the scattering particles are spherical, but they allow the polarization of the scattered photon packet to be modeled exactly. The only drawback to these methods is that they are computationally demanding and therefore somewhat slower than the aforementioned strategies. FPML treats scattering events with the algorithms developed by Wang *et al.* and Wang & Wang [12, 28].

Immediately prior to a scattering event in FPML, the photon packet is described by its local coordinate system and related Stokes vector. Upon striking a particle, the probability that the light will be scattered in a particular direction is related to the first component of the post-scattering Stokes vector. I depends on both the scattering angle, θ_s, and the azimuthal angle, ϕ_s, through rotation by equation 3.15 and multiplication with the scattering matrix of the particle. The PDF is therefore given by

$$p(\theta_s, \phi_s) = m_{11}(\theta_s) + m_{12}(\theta_s) \frac{[Q_0 \cos(2\phi_s) + U_0 \sin(2\phi_s)]}{I_0}, \qquad (3.17)$$

where Q_0, U_0, and I_0 are the Stokes vectors of the incident photon packet and $m_{11}(\theta_s)$ and $m_{12}(\theta_s)$ are elements of the scattering matrix (see Equation 3.7).
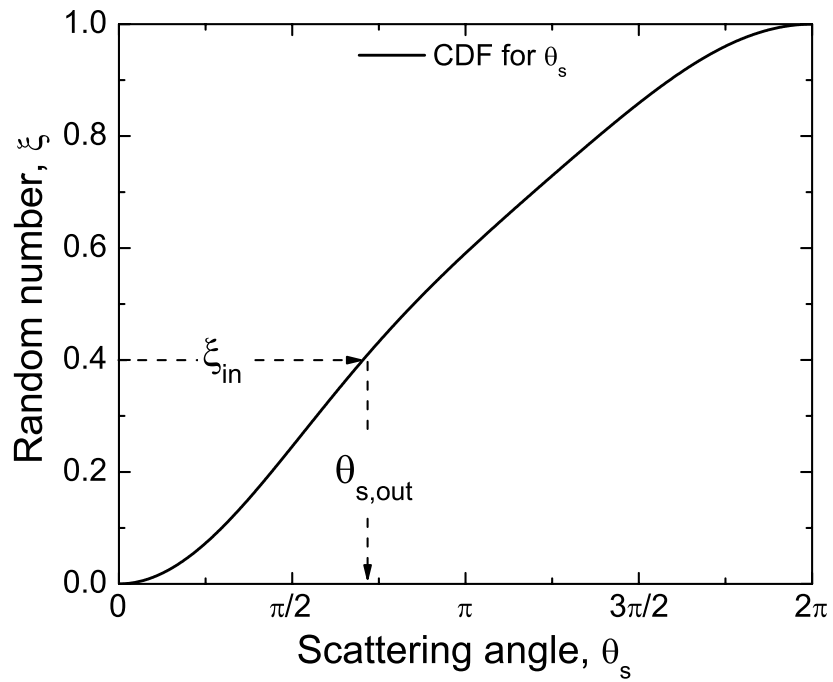
Figure 3.3: Demonstration of sampling angles using a CDF and random number generation. The CDF for the scattering angle generated from Equation 3.19 for a 0.1 μm diameter polystyrene microsphere is displayed. In order to sample the CDF, a random number, ξ_{in}, is generated and the intercept of this with the CDF is found. The azimuthal angle $\theta_{s,out}$ is selected by first finding the θ_s corresponding to the value of the CDF and then selecting the nearest discrete value.

By relying on the normalization of $m_{11}(\theta_s)$ over the interval 0 to π,

$$2\pi \int_0^\pi m_{11}(\theta_s) \sin(\theta_s) \ d\theta_s = 1, \qquad (3.18)$$

θ_s and ϕ_s are decoupled and independent selection of θ_s is possible. The CDF for the scattering angle can then be expressed as

$$P\{0 \leq \vartheta \leq \theta_s\} = 2\pi \int_0^{\theta_s} m_{11}(\vartheta_s) \sin(\vartheta_s) \ d\vartheta_s = \xi, \qquad (3.19)$$

where ξ is a uniformly distributed random number. The first element of the scattering matrix, $m_{11}(\theta_s)$, is an extremely complicated sum of products of Legendre polynomials and Riccati-Bessel functions [23]. The unwieldy construction makes calculation of the CDF at each individual scattering event prohibitively slow. This necessitates generation of a lookup table for discrete values of equation 3.19 at $\pi/1000$ intervals as utilized by Wang & Wang [28]. With this approach a value of the uniformly distributed random number ξ is mapped into a real value of θ_s as illustrated graphically in Figure 3.3.

With θ_s determined from Equation 3.19, the probability distribution function for ϕ_s can be found. Note that we have not explicitly separated equation 3.17 into parts dependent on θ and ϕ because it is not separable, but we have separated them numerically by assigning a value to θ_s and then exploring all possible outcomes of

ϕ_s. The PDF of ϕ_s given θ_s is

$$p(\phi_s|\theta_s) = 1 + \frac{m_{12}(\theta_s)}{m_{11}(\theta_s)} \frac{[Q_0 \cos(2\phi_s) + U_0 \sin(2\phi_s)]}{I_0}. \tag{3.20}$$

Therefore, the CDF for the azimuthal angle is

$$P\{0 \le \varphi \le \phi_s\} = \frac{1}{2\pi} \left\{ \phi_s + \frac{m_{12}(\theta_s)}{m_{11}(\theta_s)} \left[\frac{Q_0 \sin(2\phi_s) + U_0(1 - \cos(2\phi_s))}{2I_0} \right] \right\} = \xi. \tag{3.21}$$

To find ϕ_s, the Stokes vector elements are inserted into equation 3.21 for each scattering event, a lookup table for ϕ_s is made at $\pi/1000$ increments, and a random number is used to select ϕ_s following the method in Figure 3.3.

3.2.4 Polarized fluorescence generation

Generation of polarized fluorescence involves several steps. It requires that the simulations track the polarization of the input beam, generate fluorescence in accordance with the weight of the incoming excitation photon, and generate fluorescence with appropriate polarization.

Absorption of excitation photons

The fluorescence generation process starts with absorption of an incident excitation photon. At a given interaction with a particle in the tissue, the weight of the excitation photon packet is decreased by multiplying its weight by the albedo, α. The packet therefore deposits an amount of weight equal to 1-α in the tissue that is then available for generation of fluorescence. This energy is converted to

fluorescence at an efficiency equal to the quantum efficiency, ϱ, so that the weight of the outgoing fluorescent photon is $[1 - \alpha]\,\varrho$ times the incident photon weight [29].

Excitation photons are elliptically polarized in general, so they can be described by the ellipticity, $\varepsilon = b/a$, and azimuth, γ (Figure 3.4). Ellipticity is extracted from the Stokes parameters through the relation [23]

$$\tan 2\eta = \frac{V}{\sqrt{Q^2 + U^2}}, \tag{3.22}$$

where η is related to the ellipticity, ε, by

$$\varepsilon = \frac{b}{a} = |\tan \eta|. \tag{3.23}$$

By solving for η using equation 3.22, equation 3.23 yields the ratio of the minor to major polarization axes. U and Q can also be used to solve for γ by using

$$\tan 2\gamma = \frac{U}{Q}. \tag{3.24}$$

Solution of equation 3.24 yields the angle of tilt of the polarization ellipse measured in the clockwise sense as viewed by an observer facing the source [23].

Photon absorption occurs in a fashion similar to the approach used for the scattering angle. This requires the PDF for fluorescence excitation as a function of the angle of rotation, ω, measured from the major axis of the intensity polarization function (Figure 3.4). The intensity function is used instead of the polarization
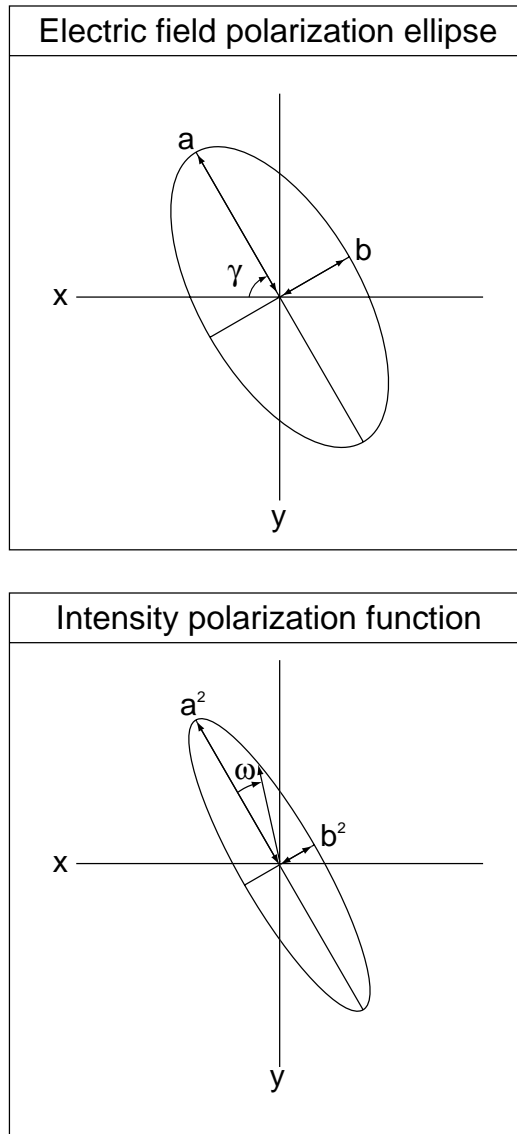
Figure 3.4: Polarization ellipse with major and minor axes defined. γ is the azimuthal angle measured from the Stokes vector parallel direction (in this case the x-axis). It is defined to be positive in the clockwise sense if the observer is facing the source. The angle used for sampling the intensity polarization function, ω, is also shown.

ellipse because the fluorescence generated is directly proportional to the intensity, not the electric field.

The ellipse describing the electric field is given by

$$r(\omega) = \frac{ab}{\sqrt{a^2 \sin^2 \omega + b^2 \cos^2 \omega}}, \tag{3.25}$$

where a and b are the major and minor axes, respectively. The PDF for intensity is

$$r^2(\omega) = p(\omega) = \frac{(ab)^2}{a^2 \sin^2(\omega) + b^2 \cos^2(\omega)}, \tag{3.26}$$

where $r^2(\omega)$ represents the intensity as a function of angle. The CDF is acquired by normalizing the integral over the interval $(0, \pi/2)$,

$$P\{0 \le \omega \le \Omega\} = \frac{\displaystyle\int_0^\Omega \frac{(ab)^2}{a^2 \sin^2(\omega) + b^2 \cos^2(\omega)}\, d\omega}{\displaystyle\int_0^{\pi/2} \frac{(ab)^2}{a^2 \sin^2(\omega) + b^2 \cos^2(\omega)}\, d\omega} = \frac{2}{\pi} \tan^{-1}\left(\frac{a}{b} \tan(\Omega)\right). \tag{3.27}$$

A lookup table for $P\{0 \le \omega \le \Omega\}$ is made for each ratio and at all angles in $\pi/1000$ increments. Sampling proceeds as it did for the scattering angle in Figure 3.3.

Since the CDF is defined over the interval $(0, \pi/2)$, it must be extended to span the range $(-\pi/2, \pi/2)$ so that all emission angles can be sampled. A random number is generated to determine if the angle is positive or negative, and with this the complete range of emission angles is covered while minimizing the size of the lookup table.

Generation of fluorescence

With the weight of the fluorescence photon and the orientation of the excitation light polarization selected, the modeling of the fluorescence generation can proceed. The process can be broken into three components: photoselection, molecular reorientation, and dipole emission.

I. *Photoselection*

In general a molecule excited by the excitation beam will not have its absorption dipole aligned strictly parallel with the incident polarization. As shown in Chapter 1, probability of excitation goes as $\cos^2\psi$, where ψ is the angle between the absorption dipole of the molecule and the incident polarization vector [30]. It is possible to sample a $\cos^2\psi$ distribution statistically to determine the orientation of the excited molecule, but this step can be folded into the molecular reorientation step by proper choice of initial conditions as outlined in section II (equation 3.32).

II. *Molecular reorientation*

After a molecule is excited in a particular direction but before the molecule emits a fluorescence photon, the orientation of the molecule changes. The probability of finding the molecule in a given orientation at a given time can be described by a diffusion equation governing rotational Brownian motion [31, 32].

There are three central assumptions implicit in the following derivation. The molecules are assumed to be spherical, which is a widely used approximation that is especially applicable when considering globular proteins [30]. It is also assumed that the molecules exist in an isotropic equilibrium system in order to

accurately model fluorophores in fluid solution that are randomly oriented without any external force. The final assumption is that the molecular absorption and transition moments are parallel, which is the case for many molecules.

Rotational Brownian motion is described by a diffusion equation [32–34],

$$\frac{dW(\theta_b, \phi_b, t)}{dt} = D_{rot} \nabla^2 W(\theta_b, \phi_b, t), \tag{3.28}$$

where D_{rot} is the rotational diffusion constant and $W(\theta_b, \phi_b, t)$ is the probability that the molecule is oriented at a polar angle θ_b and azimuthal angle ϕ_b at time t. D_{rot} is directly related to the rotational correlation time τ_r as given by

$$D_{rot} = \frac{kT}{6V_h \eta} = \frac{1}{6\tau_r}, \tag{3.29}$$

where k is the Boltzman constant, T is the temperature in kelvins, η is the viscosity, and V_h is the hydrated volume of the molecule. The solution to equation 3.28 is given by [32]

$$W(\theta_b, \phi_b, t) = \int\limits_0^{2\pi} d\phi_{b,0} \int\limits_0^{\pi} \sin\theta_{b,0} \, W(\theta_{b,0}, \phi_{b,0}) \, G(\theta_{b,0}, \phi_{b,0} \mid \theta_b, \phi_b, t) \, d\theta_{b,0}, \tag{3.30}$$

where $W(\theta_{b,0}, \phi_{b,0})$ is the initial probability distribution and $G(\theta_{b,0}, \phi_{b,0} \mid \theta_b, \phi_b, t)$ is the Green's function of equation 3.28. G can be expressed as an expansion of spherical harmonics, $Y_{l,m}$, as

$$G(\theta_{b,0}, \phi_{b,0} \mid \theta_b, \phi_b, t) = \sum_{l=0}^{\infty} \sum_{m=-l}^{l} c_l(t) \, Y_{l,m}^*(\theta_{b,0}, \phi_{b,0}) \, Y_{l,m}(\theta_b, \phi_b), \tag{3.31}$$

where the $c_l(t)$ are the time-dependent weighting coefficients that do not depend on the index, m. Allison & Schurr showed that this is the case in isotropic systems like the one considered here [34]. This is apparent by considering that the l coefficients correspond to functions that vary with the polar angle while the m values correspond to variations in the azimuthal direction. Since the population of molecules is not azimuthally dependent at any time point, it is reasonable to expect that the expansion coefficients would not depend on m.

$W(\theta_{b,0}, \phi_{b,0}, 0)$ acts as the initial condition for the solution and it can be written in terms of $\cos^2 \theta_{b,0}$ or an order 2 Legendre polynomial, $P_2(x)$, as

$$W(\theta_{b,0}, \phi_{b,0}, 0) = \frac{3}{4\pi} \cos^2 \theta_{b,0} = \frac{1}{4\pi} \left[1 + 2P_2 \left(\cos \theta_{b,0} \right) \right]. \tag{3.32}$$

By using this initial condition, the photoselection process is included in the solution to the rotational motion of the molecules [32]. This circumvents a separate computational step for the absorption of the photon.

Tao showed that consideration of boundary conditions, normalization, and orthonormality of spherical harmonics leads to the elimination of all expansion coefficients except for $c_2(t) = e^{-l(l+1)D_{rot}t}$ [32]. With $l = 2$,

$$c_2(t) = e^{-6D_{rot}t} = e^{-t/\tau_r}. \tag{3.33}$$

Integration of equation 3.30 with $c_2(t)$ inserted yields the solution for $W(\theta_b, \phi_b, t)$, namely

$$W(\theta_b, \phi_b, t) = \frac{1}{4\pi} \left[1 + 2e^{-t/\tau_r} P_2 \left(\cos \theta \right) \right]. \tag{3.34}$$

Equation 3.34 yields the probability of finding a molecule in a given orientation as a function of time assuming an initial photoselection at $t = 0$. FPML relies on knowledge of the *excited state* distribution of molecules as a function of time, $\Gamma(\theta_b, \phi_b, t)$. Multiplying the solution given in equation 3.34 by the time-dependent decay in the number of excited state molecules gives [33],

$$\Gamma\left(\theta_b, \phi_b, t\right) = W\left(\theta_b, \phi_b, t\right) e^{-t/\tau} = \frac{1}{4\pi}\left[1 + 2e^{-t/\tau_r} P_2\left(\cos\theta_b\right)\right] e^{-t/\tau}, \qquad (3.35)$$

where τ is the fluorescence lifetime. $\Gamma\left(\theta, \phi, t\right)$ can then be sampled using the approach used to sample the azimuthal and scattering angles.

Selection of ϕ_b proceeds independently of t and θ_b as it does not explicitly appear in Equation 3.35. Since azimuthal symmetry is preserved for all times, it is sampled with $\phi_b = 2\pi\xi$.

The PDF for θ_b and t is

$$p(\theta_b, t) = \frac{1}{4\pi\tau}\left[1 + e^{-t/\tau_r}\left(3\cos^2\theta_b - 1\right)\right] e^{-t/\tau}, \qquad (3.36)$$

where in going from Equation 3.35 to 3.36 the substitution $2P_2\left(\cos\theta_b\right) = 3\cos^2\theta_b - 1$ was made. Since equation 3.36 depends on both t and θ_b, one of these terms must be sampled independently in order to proceed. The PDF for t is given by

$$p(t) = \tau\, e^{-t/\tau}, \qquad (3.37)$$

which is sampled by $t = -\frac{1}{\tau}\log\left(\xi\right)$. The PDF of θ_b given t is therefore

$$p(\theta_b|t) = \frac{1}{2}\left[1 + \mathrm{e}^{-t/\tau_r}\left(3\cos^2\theta_b - 1\right)\right]. \tag{3.38}$$

Integrating the PDF gives the CDF of θ_b as

$$P\left\{0 \leq \vartheta \leq \theta_b\right\} = \frac{1}{2}\left[1 + \left(\frac{\mathrm{e}^{-t/\tau_r}}{4} - 1\right)\cos\theta_b - \frac{\mathrm{e}^{-t/\tau_r}}{4}\cos 3\theta_b\right] = \xi, \tag{3.39}$$

which is sampled using the same approach as that for the CDF for the scattering angle as demonstrated Figure 3.3.

III. *Fluorescence emission*

In 1939 Selényi determined that fluorescent molecules emit light like dipole radiators [35]. FPML therefore uses $\sin^2\theta_d$ as the distribution of fluorescence intensity, where θ_d is the angle between the dipole axis and the direction into which light is emitted [36]. Setting the CDFs for ξ and θ_d equal, the equation used for sampling is

$$\frac{3}{4}\int_0^{\theta_d}\sin^2(\vartheta)\sin(\vartheta)\,d\vartheta = \xi. \tag{3.40}$$

Equation 3.40 is sampled using a lookup table for θ_d in $\pi/1000$ increments with the approach outlined in Figure 3.3. There is no azimuthal dependence to dipole radiation, so sampling proceeds according to $\phi_d = 2\pi\xi$. The outgoing photon is therefore launched with a direction defined by the pair (θ_d, ϕ_d) and Stokes vector [1100].

3.2.5   Determination of the final Stokes vector

In FPML the Stokes vector for each photon passing through the pinhole is recorded separately. Since the Stokes vectors are additive, the polarization of the detected light is found by summing the contribution of all photon packets. Anisotropy can be found directly from the Stokes vectors by noting that $I = I_\parallel + I_\perp$ and $Q = I_\parallel - I_\perp$ (Appendix A). By combining these terms the anisotropy of the nth photon packet is

$$r_n = \frac{2Q_n}{3I_n - Q_n}. \tag{3.41}$$

From this the total anisotropy from all detected photons is given by

$$r_{total} = \sum_n r_n i_n = \sum_n r_n \frac{(3I_n - Q_n)}{2T_i}, \tag{3.42}$$

where i_n is the fractional intensity of the nth photon packet and T_i is the total intensity of all collected light, $T_i = \sum_n \frac{1}{2} (3I_n - Q_n)$.

In this chapter we have presented a Monte Carlo approach to simulate confocal fluorescence polarization imaging in scattering media. It relies on polarization tracking techniques and photon migration routines developed previously, but it adds the additional capabilities of fluorescence polarization generation. This is accomplished through routines that sample elliptical polarization, generate polarized fluorescence through considerations of Brownian motion, and model emission of fluorescence as dipole radiation.

In Chapter 4 the routines outlined here are applied to understanding scattering effects on anisotropy images. We will present results from experiments

performed on fluorescent targets at depth in phantoms consisting of polystyrene microspheres. By running simulations based on routines presented here, we are able to determine the effects of the number of scattering events, depth of target, photon path length, objective numerical aperture and pinhole size on imaging. From this detailed analysis and comparison of experiment to simulation, we determine what modifications to the optical setup can increase the fidelity of anisotropy images at depth.

References

[1] T. Wilson and C. Sheppard, *Theory and Practice of Scanning Optical Microscopy* (Academic Press, London, 1984).

[2] M. Gu, *Principles of Three-Dimensional Imaging in Confocal Microscopes* (World Scientific, London, 1996).

[3] X. Gan and M. Gu, "Effective point-spread function for fast image modeling and processing in microscopic imaging through turbid media," Opt. Lett. **24,** 741–743 (1999).

[4] J. Schmitt, A. Knuttel, and M. Yadlowsky, "Confocal microscopy in turbid media," J. Opt. Soc. Am. A **11,** 2226–2235 (1994).

[5] L. G. Henyey and J. L. Greenstein, "Diffuse radiation in the galaxy," Astrophys. J. **93,** 70–83 (1941).

[6] J. Schmitt and K. Ben-Letaief, "Efficient Monte Carlo simulation of confocal microscopy in biological tissue," J. Opt. Soc. Am. A **13,** 952–961 (1996).

[7] C. Smithpeter, A. Dunn, A. Welch, and R. Richards-Kortum, "Penetration depth limits of *in vivo* confocal reflectance imaging," Appl. Optics **37,** 2749–2754 (1998).

[8] X. Gan, S. Schilders, and M. Gu, "Image formation in turbid media under a microscope," J. Opt. Soc. Am. A **15,** 2052–2058 (1998).

[9] X. Gan, S. Schilders, and M. Gu, "Combination of annular aperture and polarization gating methods for efficient microscopic imaging through a turbid medium: theoretical analysis," Microsc. Microanal. **3,** 495–503 (1997).

[10] X. Gan, S. Schilders, and M. Gu, "Image enhancement through turbid media under a microscope by use of polarization gating methods," J. Opt. Soc. Am. A **16,** 2177–2184 (1999).

[11] F. Jaillon and H. Saint-Jalmes, "Description and time reduction of a Monte Carlo code to simulate propagation of polarized light through scattering media," Appl. Optics **42,** 3290–3296 (2003).

[12] X. Wang, L. V. Wang, C.-W. Sun, and C.-C. Yang, "Polarized light propagation through scattering media: time-resolved Monte Carlo simulations and experiments," J. Biomed. Opt. **8,** 608–617 (2003).

[13] M. Gu, S. Schilders, and X. Gan, "Two-photon fluorescence imaging of microspheres embedded in turbid media," J. Mod. Opt. **47,** 959–965 (2000).

[14] X. Gan and M. Gu, "Fluorescence microscopic imaging through tissue-like turbid media," J. Appl. Phys. **87,** 3214–3221 (2000).

[15] M. Gu, X. Gan, A. Kisteman, and M. G. Xu, "Comparison of penetration depth between two-photon excitation and single-photon excitation in imaging through turbid tissue media," Appl. Phys. Lett. **77,** 1551–1553 (2000).

[16] S. Schilders and M. Gu, "Limiting factors on image quality in imaging through turbid media under single-photon and two-photon excitation," Microsc. Microanal. **6,** 156–160 (2000).

[17] X. Gan and M. Gu, "Spatial distribution of single-photon and two-photon fluorescence light in scattering media: Monte Carlo simulation," Appl. Optics **39,** 1575–1579 (2000).

[18] V. R. Daria, C. Saloma, and S. Kawata, "Excitation with a focused, pulsed optical beam in scattering media: diffraction effects," Appl. Optics **39,** 5244–5255 (2000).

[19] M. H. Kalos and P. A. Whitlock, *Monte Carlo Methods Volume I: Basics* (John Wiley & Sons, New York, 1986).

[20] S. C. Harvey and H. C. Cheung, "Computer simulation of fluorescence depolarization due to Brownian motion," Porc. Nat. Acad. Sci. USA **69,** 3670–3672 (1972).

[21] L. V. Wang, S. L. Jacques, and L. Zheng, "MCML - Monte Carlo modeling of photon transport in multi-layered tissues," Comput. Methods Programs Biomed. **47,** 131–146 (1995).

[22] S. A. Prahl, M. Keijzer, S. L. Jacques, and A. J. Welch, "A Monte Carlo model of light propagation in tissue," SPIE Institute Series **IS 5,** 102–111 (1989).

[23] C. F. Bohren and D. R. Huffman, *Absorption and scattering of light by small particles* (Wiley Interscience, New York, 1983).

[24] S. Bartel and A. H. Hielscher, "Monte Carlo simulations of the diffuse backscattering Mueller matrix for highly scattering media," Appl. Optics **39,** 1580–1588 (2000).

[25] J. H. Ginsberg, *Advanced Engineering Dynamics*, 2nd ed. (Cambridge University Press, New York, 1995).

[26] E. Collett, *Polarized light: Fundamentals and applications* (Marcel Dekker, New York, 1993).

[27] M. J. Raković, G. W. Kattawar, M. Mehrűbeoğlu, B. D. Cameron, L. V. Wang, S. Rastegar, and G. L. Coté, "Light backscattering polarization patterns from turbid media: theory and experiment," Appl. Optics **38,** 3399–3408 (1999).

[28] X. Wang and L. Wang, "Propagation of polarized light in birefringent turbid media: A Monte Carlo study," J. Biomed. Opt. **7,** 279–290 (2002).

[29] J. Wu, M. S. Feld, and R. P. Rava, "Analytical model for extracting intrinsic fluorescence in turbid media," Appl. Optics **32,** 3585–3595 (1993).

[30] J. R. Lakowicz, *Principles of Fluorescence Spectroscopy*, 2nd ed. (Kluwer Academic/Plenum Publishers, New York, 1999).

[31] A. Einstein, "Über die von der molekularkinetischen theorie der wärme geforderte bewegung von in ruhenden flüssigkeiten suspendierten teilchen," Ann. Phys. **17,** 549–560 (1905).

[32] T. Tao, "Time-dependent fluorescence depolarization and Brownian rotational diffusion coefficients of macromolecules," Biopolymers **8,** 609–632 (1969).

[33] C. R. Cantor and P. R. Schimmel, *Biophysical Chemistry Part II: Techniques for the study of biological structure and function* (W.H. Freeman and Company, New York, 1980).

[34] S. A. Allison and J. M. Schurr, "Torsion dynamics and depolarization of fluorescence of linear macromolecules. I. Theory and application to DNA," Chem. Phys. **41,** 35–59 (1979).

[35] P. Selényi, "Wide-angle interferences and the nature of the elementary light sources," Phys. Rev. **56,** 477–479 (1939).

[36] D. J. Griffiths, *Introduction to Electrodynamics*, 2nd ed. (Prentice Hall, Englewood Cliffs, New Jersey, 1989).

Chapter 4

Effects of Light Scattering on Fluorescence Anisotropy

4.1 Introduction

Imaging deep into turbid samples using confocal microscopy presents a number of technical challenges. Ballistic light used for diffraction-limited imaging is exponentially attenuated by the presence of scattering (see equation 1.7), and that inevitably leads to signal-to-noise ratio (SNR) concerns even 1 or 2 scattering lengths into tissue [1]. In single photon imaging, however, the depth to which signal can be acquired with sufficient SNR exceeds that allowed by the ballistic light as scattered photons contribute to the signal [2]. For targets at depth in scattering media, both the excitation photons and fluorescence photons experience scattering. Therefore, photons that would normally be rejected by the pinhole in the absence of scattering contribute to the signal *via* redirection into the acceptance cone of the objective lens. These scattered photons carry less (if any) useful information about the sample of interest, and as a result images constructed with them experience a reduction in resolution [3]. A better understanding of the ef-

fects scattering has on images in turbid media has encompassed three major foci of research relevant to fluorescence polarization imaging: objective lens numerical aperture, pinhole size, and polarization discrimination.

The objective numerical aperture plays a role in image resolution in both the diffraction-limited and scattering regimes. In scattering media at depths shallower than about 1 scattering length, ℓ_s, the NA determines resolution according to the relations in equation 1.5. For images acquired deeper than this, however, the NA affects the amount of scattered light that is collected by the optical system. Gan *et al.* used Monte Carlo simulations to study the effects of numerical aperture alone on the transverse resolution of targets at depth. They found the counterintuitive result that, with the pinhole removed, lower NA objectives yield better transverse resolution than higher NA objectives for imaging at depths $\geq \ell_s$ [4, 5]. They also showed, with the confocal aperture removed, that lower NAs yield better resolution for targets located deeper than ℓ_s for a given number of scattering events. These results show that the lower NA objectives act as an angular gate for scattered photons, meaning that they preferentially reject light scattered into angles deviating from the forward direction.

The pinhole is the most widely used and effective method for discriminating against scattered light. Pinholes are effective because they discriminate against photons that deviate significantly from the path taken by ballistic light. Unscattered light forms a diffraction-limited spot at the pinhole plane, and the pinhole diameter is typically selected to allow these to pass through. Light experiencing scattering, however, is angularly deviated from the path taken by ballistic photons, and this angle change translates into a lateral shift at the pinhole plane.

Therefore scattered light will tend to fall outside the diameter of the pinhole and will be prevented from reaching the detector. Unlike the angle gating effects of numerical aperture, insertion of a pinhole changes the fraction of unscattered *vs.* scattered light that is ultimately detected [4]. The effect is such that decreasing the pinhole radius biases the detected light distribution toward the unscattered photons. This was quantified by Gan & Gu by consideration of an effective point spread function that accounts for the effects of the tissue on image resolution [5, 6].

Polarization gating methods in reflectance are also useful for increasing image quality at depth [7]. The degradation of polarization in turbid media certainly occurs from scattering, but the onset of depolarization is slower than the randomization of the angular distribution of light [8]. This property makes the technique appealing for increasing the efficacy of imaging at depth, and indeed Gan *et al.* and Morgan *et al.* showed that the addition of polarization gating techniques increased lateral resolution at depth [9, 10].

In this chapter we utilize the Monte Carlo code outlined in Chapter 3 to analyze polarization preservation as a function of depth into scattering media. Experimental results are also presented that quantify the loss of fluorescence anisotropy fidelity as images of a fluorophore-embedded polymer bar are acquired to depths up to 600 μm. We explore the advantages and disadvantages of gating techniques involving NA and pinhole size from the standpoint of fluorescence anisotropy preservation.

4.2 Methods

4.2.1 Experimental measurements of depolarization

In order to measure the depth-dependent depolarization of fluorescence due to scattering, we developed an experimental apparatus based on the fluorophore-embedded polymer bar introduced in Chapter 2. The setup consisted of a dish with a coverslip bottom filled with an aqueous suspension of polystyrene microspheres. The face of the bar was imaged in the inverted geometry at depths ranging from 0 μm with the bar resting on the coverslip to 600 μm into the scattering medium in 100 μm increments.

The bar was prepared for imaging by polishing with a 1 μm lapping film followed by a 0.3 μm lapping film (LFG1P & LFG03P, Thorlabs, Inc., Newton, NJ). With this surface prepared, the bar was attached to an optical post, which was, in turn, connected to a vertically oriented translation stage. The stage and associated micrometer allowed precise movement of the location of the bar within approximately $\pm$ 1 μm in the geometry shown in Figure 4.1.

Two scattering phantoms were prepared for experiments. One contained an aqueous suspension of 0.1 μm diameter polystyrene microspheres and the other 0.511 μm spheres (5010A and 5051A, Duke Scientific Corporation, Palo Alto, CA). These two bead sizes were chosen as they are relevant to biological scatterers, and they have very different scattering phase functions. Specifically, the scattering anisotropy, g, is 0.09 for the 0.1 μm beads and 0.84 for the 0.511 μm beads. The microsphere concentration was adjusted to account for the difference in scattering cross section to maintain ℓ_s=100 μm at the fluorescence wavelength. The beads
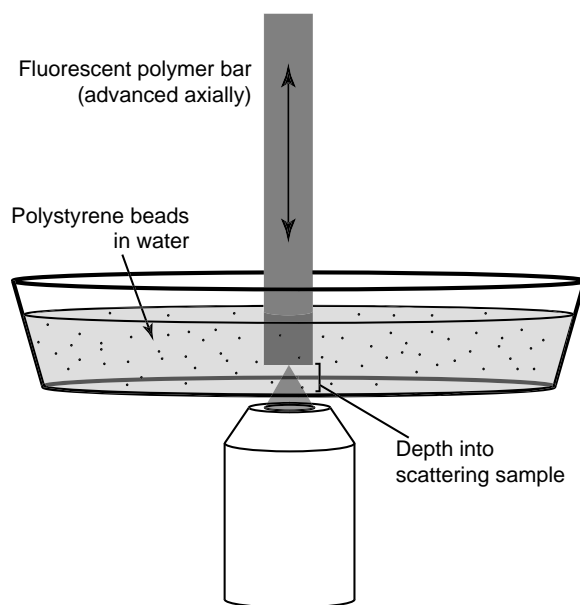
Figure 4.1: Schematic of setup used to quantify the artificial degradation of anisotropy due to scattering at depth in turbid media. The fluorophore-containing bar was attached to a micrometer that enabled vertical translation in 100 μm steps with $\pm$ 1 μm accuracy.

were packaged at 10 % solids by weight in water, and therefore to achieve an $\ell_s=100$ μm, the 0.1 μm and 0.511 μm microspheres were diluted in water by a factor of 1.39 and 26.6, respectively.

Two objectives were used for experiments. We utilized a 10×, 0.45 NA and a 4×, 0.13 NA objective to reveal the effects that the numerical aperture has on anisotropy imaging. A range of pinholes was used with each objective for exploration of the effect of the size of the confocal aperture on anisotropy fidelity at depth in scattering media. The 4× objective was used with four pinhole diameters: 100, 200, 400, and 600 μm. Since the optimal diameter according to the criterion described by equation 1.6 is 100 μm, these pinholes correspond to 1, 2, 4, and 6 times the ideal size. The 10× objective was used with 75, 150, 400, and 600 μm diameter pinholes, which correspond to 1, 2, 5.3, and 8 times the optimal size. The discrete pinhole diameters available commercially limited our choices, so these two sets were matched as closely as possible with regards to multiples of the optimal diameter.

The experiment progressed by first resting the bar on the coverslip in the microsphere suspension to establish the 0 μm depth. An axial scan into the bar was taken by advancing the objective with the focus maintained on axis. Once the maximum signal was reached the 0 μm depth image was acquired. The face of the bar was subsequently advanced in 100 μm increments into the solution to a depth of 600 μm, and an image was acquired at each depth. Note that the position of the objective was only advanced 73 μm between images to account for the axial scaling factor induced by the mismatch in refractive indices between the objective immersion medium (air) and the bar immersion medium (water) [11]. At each

depth a 400×400 μm anisotropy image was acquired, and the mean anisotropy across the entire field of view was reported.

4.2.2 Monte Carlo routines

Monte Carlo simulations were performed using the routines outlined in Chapter 3. The simulation was set up as a two-layer medium with beads in a thin layer either 100 μm or 200 μm thick between the coverslip and the bar, and the bar set to a thickness of 20 cm. Lateral dimensions of the sample were assumed to be infinite, which is a reasonable approximation given the relevant scattering lengths, the 2 mm bar radius, and the close proximity of the bar to the coverslip.

Optical properties were set to closely match experiment, and consequently the layer of beads was set to be purely scattering and the bar purely absorbing. The scattering coefficient, μ_s, was chosen such that the scattering length was approximately 100 μm at the fluorescence wavelength and ℓ_s for the excitation wavelength was allowed to change in response to this requirement. For example, the λ^{-4} wavelength dependence of μ_s from the 0.1 μm beads in the visible spectrum led to a scattering length at the excitation wavelength that was 45 μm, a factor of 2.2 shorter than at the fluorescence wavelength. Absorption coefficients in the bar were set equal to fluorometer absorption values measured from thin slices of the bar. A summary of optical properties utilized in the simulations is given in Table 4.1.

Three simulation runs were performed in order to address conditions that would affect typical imaging in tissue and to conserve computational runtime. Two of the three simulations were performed with the bar at a depth of 100 μm in

Parameters used in Monte Carlo simulations				
Layer	$\mu_{a,ex}$	$\mu_{s,ex}$	$\mu_{a,fl}$	$\mu_{s,fl}$
Beads (0.1 μm)	0 cm^{-1}	224 cm^{-1}	0 cm^{-1}	101 cm^{-1}
Beads (0.5 μm)	0 cm^{-1}	158 cm^{-1}	0 cm^{-1}	101 cm^{-1}
Bar	92 cm^{-1}	0 cm^{-1}	98 cm^{-1}	0 cm^{-1}

Table 4.1: Parameters used in Monte Carlo simulation of the fluorophore-containing rod in an aqueous suspension of polystyrene microspheres. Optical properties are shown for both the excitation wavelength (488 nm) and the fluorescence emission maximum (590 nm) with both bead sizes. Values for scattering coefficients were set to yield a scattering length of approximately 100 μm at the fluorescence wavelength. Absorption coefficients are measured values.

two different scattering media consisting of 0.1 μm and 0.511 μm beads. A third run was done for the bar at 200 μm deep into a suspension of 0.511 μm beads.

Simulations tracked photons through the medium, and upon exiting the tissue the recorded parameters including photon position, photon weight, Stokes vector, and number of scattering events encountered for both excitation and fluorescence photons. These parameters were not assembled into bins like in MCML, as the exact photon positions and weights were necessary to track photons escaping the surface through the confocal arrangement assembled in OSLO (see Figure 3.1). The microscope was equipped with either a 0.13 NA or 0.45 NA lens, and pinhole sizes in the simulation were varied and reported as multiples of the optimal size calculated from equation 1.6.

4.3 Results

4.3.1 Experimental results

Results from experiments performed with the fluorophore-containing bar that examined the effects of objective lens numerical aperture and pinhole size are shown in Figure 4.2. For this set of experiments, 0.1 μm diameter beads were used as was the full complement of pinholes for both the 4× and 10× objectives. Plot A shows results for anisotropy acquired with the 4×, NA 0.13 objective. Anisotropy degrades more severely at depth for larger pinholes, but at shallow depths less than 100 μm, there is no dependence on pinhole size. As would be expected from the role of the pinhole in the rejection of scattered light, the optimal pinhole
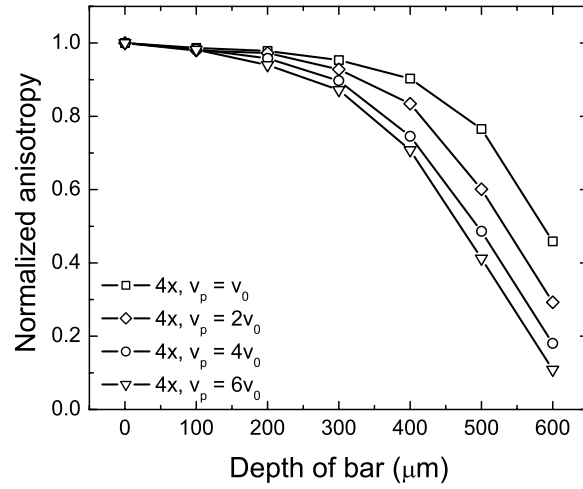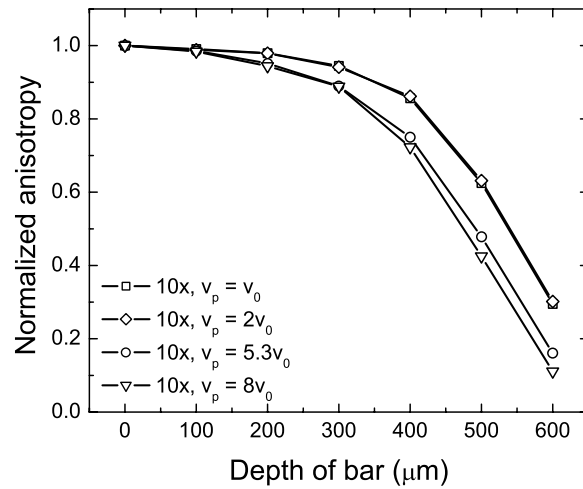
Figure 4.2: Experimental results indicating the effect of NA and pinhole size on the fidelity of anisotropy at depth in scattering media. Both plots contain data acquired with 0.1 μm microspheres, but A is from the $4\times$, NA 0.13 objective and B is from the $10\times$, NA 0.45 objective. Pinhole diameter, v_p, is given relative to the optimal size, v_0.

size yields the most accurate anisotropy at all depths. Plot B shows results from data acquired with the 10× objective. There is a similar trend as that observed with the 4× objective in that larger pinholes yield less accurate anisotropies at depth. There is a noticeable difference between the performance of the two objectives for the optimal pinhole size, however. The 10× and 4× objectives preserve anisotropy equally well at shallow depths, but beyond 5 scattering lengths ($5\ell_s$) at the fluorescence wavelength, the 4× reports more accurate anisotropies. At $6\ell_s$, for example, both objectives experience severe scattering-based anisotropy degradation, but the 4× reports r 50% higher than the corresponding 10× case. The source of this discrepancy is most likely the ability of the lower NA objective to discriminate against scattered light. For the 0.1 μm beads, $g=0.09$ and it is likely that the scattering angle will be large. If it is deflected at an angle greater than the acceptance cone dictated by the NA, then the photon will not be detected. The 10× objective has an NA that is more than 3-fold larger than the 4× objective, and it will therefore necessarily accept more scattered light even with the optimal pinhole diameter. It is important to note, however, that these effects are prominent at scattering depths beyond which useful images can be acquired. At shallow depths where there is appreciable ballistic light available for image formation, the effect is much less apparent and the 10× objective will yield much better axial and in-plane resolution.

Figure 4.3 displays data illustrating the effect of the scattering phase function on measurements of r in scattering media. Both A and B were acquired with the 10×, 0.45 NA objective with the same set of pinholes and at the same depths. The scattering phantom in A consisted of 0.1 μm beads, while that in B was 0.511
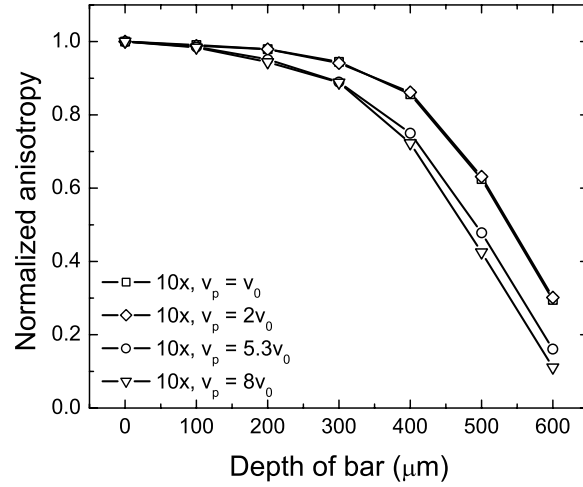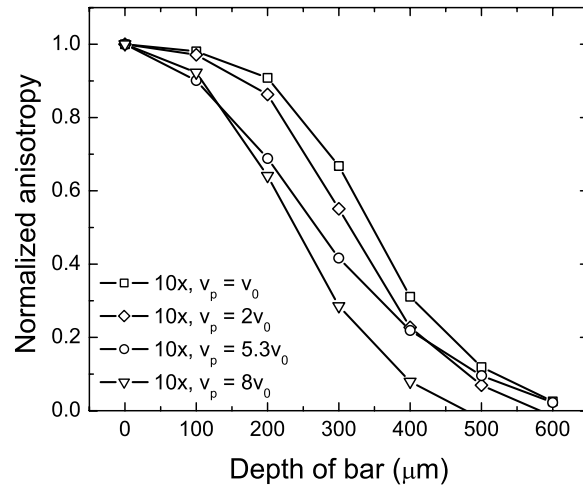
Figure 4.3: Experimental results indicating the effect of the scattering phase function on the fidelity of anisotropy at depth in scattering media. Both plots contain data acquired with the $10\times$, 0.45 NA objective, but measurements in A and B are derived from measurements made in aqueous suspensions of 0.1 μm and 0.511 μm diameter beads with g values of 0.09 and 0.84, respectively. Pinhole radius, v_p, is given relative to the optimal size, v_0.

μm beads, thereby allowing the direct comparison of the effects of particles with g differing by an order of magnitude. The general trend is for larger pinholes to lead to faster degradation of anisotropy at depth. However, the 0.1 μm beads maintain the polarization more effectively at depth than do the 0.511 μm beads. This is likely a complicated combination of scattering effects that will be informed by results of Monte Carlo simulations in section 4.3.2.

These results have practical consequences, as the scattering-induced degradation of anisotropy can be reduced significantly at depths where useful images can be acquired. With an optimal pinhole diameter in media containing the 0.511 μm beads, the anisotropy is degraded by 2% at a depth of 100 μm. This may be observable experimentally with sufficient SNR, but the 9% difference observed at 200 μm will likely be significant in those cases where signal levels permit anisotropy measurements to be made. The effect is much less prominent for the 0.1 μm beads, but these are slightly less relevant biologically from a light scattering standpoint, as shown by fits to data from intact cells in our 2005 *Biophysical Journal* paper [12].

4.3.2   Monte Carlo results

In order to test the ability of our Monte Carlo routine to model the degradation of anisotropy with scattering in our experimental system, we plotted a subset of the experimental data together with results from our fluorescence polarization Monte Carlo routine, FPML. We compared values measured from the bar 100 μm into a scattering suspension of 0.511 μm beads to the same quantity simulated in FPML. The results of this comparison are shown in Figure 4.4. The two sets of data match
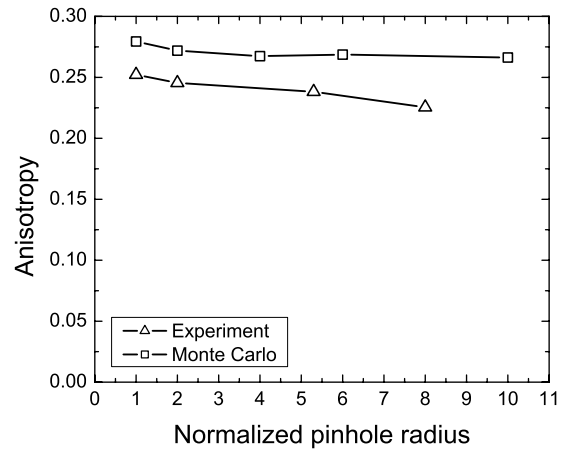
Figure 4.4: Comparison of Monte Carlo routine output to experimental data. Data and simulations were performed for a scattering medium containing 0.511 μm beads with the fluorescent bar located 100 μm from the coverslip.

well qualitatively, but there is a quantitative difference with the Monte Carlo results returning anisotropy values consistently 10% higher than those measured experimentally. This discrepancy is due to experimental variations that appear to originate in the bar itself. The value of 0.275 chosen for the anisotropy of the target was selected based on typical values returned by experiment, but it was a choice within a range of typical values. Indeed, had the Monte Carlo routines been designed using a target anisotropy of 0.25, the data and simulation would have matched quite well, especially for smaller pinholes.

Figure 4.5 contains results from the Monte Carlo run for the bar face at 100 μm deep into a suspension of 0.1 μm scattering beads imaged with a 0.45 NA lens. Figure 4.5A demonstrates the effect of changing pinhole size on the measured anisotropy. Anisotropy is maintained within 11% for pinholes up to 10 times the optimal diameter. Beyond that limit the magnitude of the slope of r *vs.* pinhole size increases until a pinhole of 1000 times optimal leads to an artifactual decrease of r to only 30% of its actual value. Figure 4.5B demonstrates why this decrease occurs. The r data is reproduced here in conjunction with two traces indicating how scattering is affecting the anisotropy. These traces indicate (1) how many scattering events, on average, were experienced by light that excited fluorescence in the bar that was eventually detected and (2) the number of times the fluorescence was scattered after generation, on average, before reaching the pinhole. There is a clear correlation between an increase in the number of scattering events and a decrease in anisotropy. There is also a clear difference between the mean number of scattering events that the excitation and fluorescence experience as a result of the decrease in μ_s at the emission wavelength. This indicates that larger
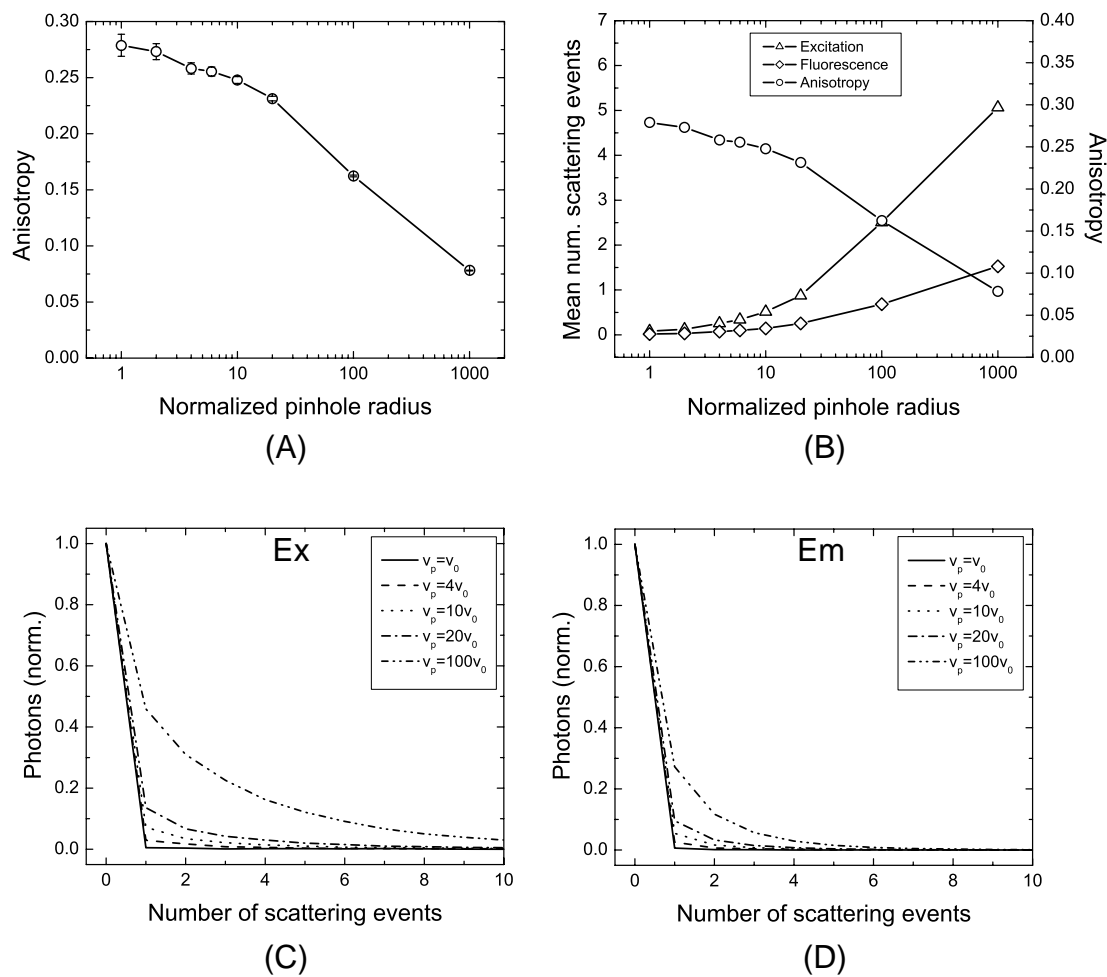
Figure 4.5: Monte Carlo simulations of the anisotropy returned from a planar fluorescent target located 100 μm into an aqueous suspension of 0.1 μm diameter microspheres and imaged with a 0.45 NA objective. Plot A shows the effect on r of increasing the pinhole diameter from 1 to 1000 times the optimal value. B displays the mean value of r from A along with the mean number of scattering events experienced by excitation and fluorescence photons for each pinhole size. C and D are histograms of the number of scattering events for each pinhole size for the excitation (Ex) and fluorescence (Em), respectively. Error bars are standard error of the mean.

pinholes are allowing light that has been scattered more times to be detected, and that the result of this is a decrease in anisotropy. Figure 4.5, C and D, display the histograms for excitation and fluorescence, respectively, from which the mean values in Figure 4.5B were calculated. In both cases for all pinhole sizes there is a very strong ballistic component that appears as a large peak at 0 scattering events. It is this light that is responsible for diffraction-limited imaging, and its dominance over 1 or more scattering events is an indicator that the pinhole is performing well and confocality has been achieved. The effect of different optical properties at the excitation and emission wavelengths can clearly be seen, as the histograms for the excitation light are clearly broader than those for fluorescence.

Results of the Monte Carlo simulations for the 0.511 μm beads and the target located 100 μm deep are shown in Figure 4.6. Figure 4.6A shows the dependence of the mean value of r *vs.* pinhole size to be less severe than in the case of the 0.1 μm beads. With these larger beads, larger pinholes result in much higher measured anisotropies than those shown in Figure 4.5. Figure 4.6B shows the dependence of r on the mean number of scattering events for excitation and emission photons. For this bead size, excitation and fluorescence photons that contribute to the detected signal are only scattered about 40% and 80% as many times as with 0.1 μm beads at $v_p=1000v_0$. The histograms in Figure 4.6, C and D, are quite different than those observed with the smaller microspheres. For pinholes near the optimal size there is still a strong ballistic component, but larger diameters eventually lead to the peak of the distribution for scattered light shifting away from zero, indicating a loss of the dominance of the ballistic component.
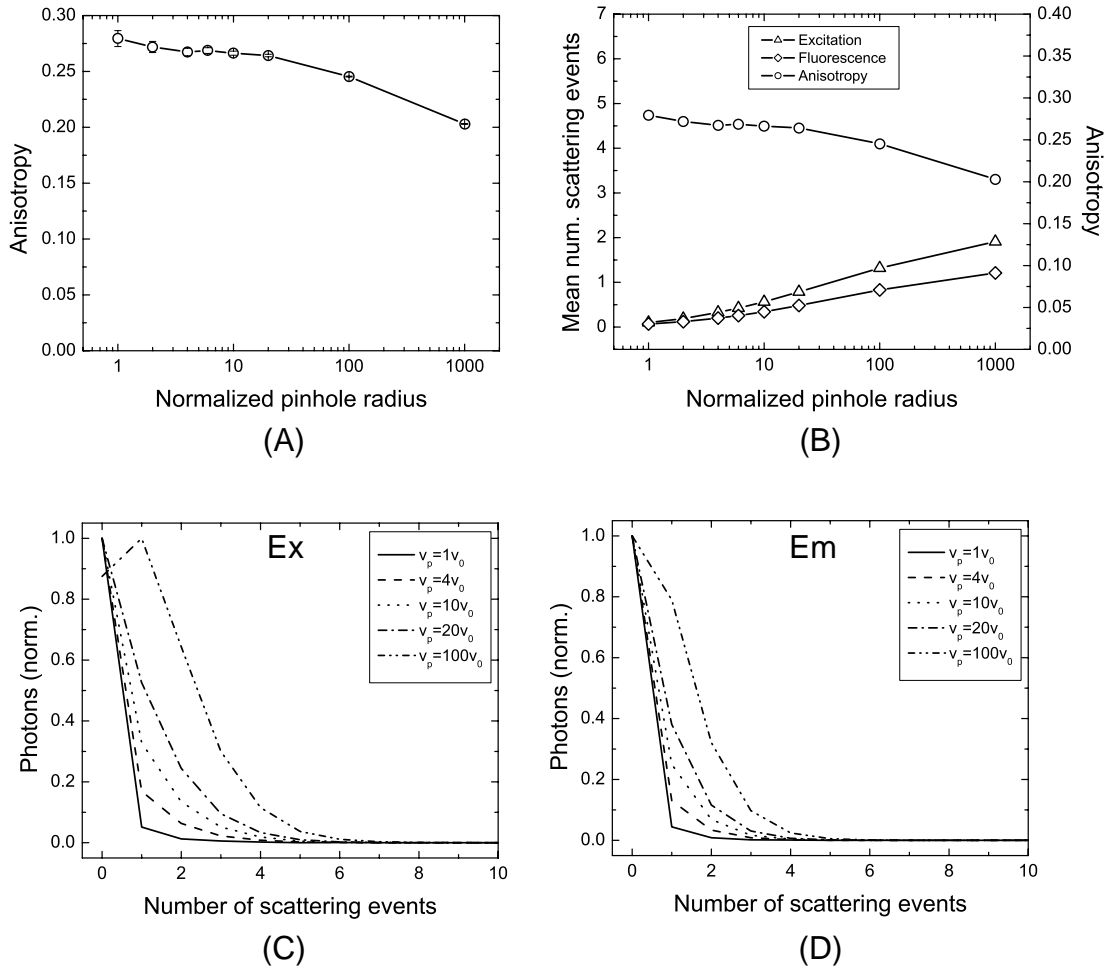
Figure 4.6: Monte Carlo simulations of the anisotropy returned from a planar fluorescent target located 100 μm into an aqueous suspension of 0.511 μm diameter microspheres and imaged with a 0.45 NA objective. Plot A shows the effect on r of increasing the pinhole diameter from 1 to 1000 times the optimal value. B displays the mean value of r from A along with the mean number of scattering events experienced by the excitation light and fluorescence emission for each pinhole size. C and D are histograms of the number of scattering events for each pinhole size for the excitation (Ex) and fluorescence (Em), respectively. Error bars are standard error of the mean.

Figure 4.7: Monte Carlo simulations of the anisotropy returned from a planar fluorescent target located 200 μm into an aqueous suspension of 0.511 μm diameter microspheres and imaged with a 0.45 NA objective. Plot A shows the effect on r of increasing the pinhole diameter from 1 to 1000 times the optimal value. B displays the mean value of r from A along with the mean number of scattering events experienced by the excitation light and fluorescence emission for each pinhole size. C and D are histograms of the number of scattering events for each pinhole size for the excitation (Ex) and fluorescence (Em), respectively. Error bars are standard error of the mean.

The plots shown in Figure 4.7 were produced by running a simulation with the same optical properties as in Figure 4.6 but with the bar located at 200 μm. The mean anisotropy in Figure 4.7A is lower than that found with the bar at 100 μm. The scattering distributions in Figure 4.7B indicate that this is due to the mean number of scattering events being higher, even for the optimal pinhole diameter. For example, with $v_p = v_0$, the mean number of scattering events for excitation and fluorescence photons are both approximately a factor of 3 higher for the target at 200 μm *vs.* 100 μm. The scattering histograms in Figure 4.7, C and D, reflect this as well, as they are broader than those at 100 μm. For excitation photons with $v_p = 100 v_0$, the peak of the distribution shifts to 2 scattering events, and the ballistic component is only 48% of the peak value. The fluorescence photon peak also exhibits a shift for $v_p = 100 v_0$, a feature which was not observed for any pinhole size in Figure 4.5 or 4.6. From a practical standpoint, however, there is still a significant ballistic contribution for optimal pinhole sizes, so some image information remains in the fluorescence.

4.4 Discussion

The experimental and Monte Carlo results presented here demonstrate the utility and limitations of the anisotropy technique as well as the importance of the microscope parameters that determine the fidelity of the measurements.

Effect of varying the objective NA

The objective lens numerical aperture is an essential parameter for determining the diffraction-limited resolution in confocal microscopy (see equation 1.5). Our experimental results show that variation of the NA has some effect on confocal microscopy at depth in turbid media, although it does not appear to affect the anisotropy at depths for which useful images can be acquired in practice. For example, Figure 4.2 shows the effect of changing the NA on the fidelity of the measured anisotropy at depth. The r plots for the $4\times$ objective with $v_p = v_0$ and $v_p = 2v_0$ indicate that there is a loss in the ability to discriminate against scattered light as the pinhole size increases to $2v_0$ for depths $\gtrsim 300\ \mu$m. For shallower depths where the vast majority of imaging occurs in practice, there is no discernible difference between r acquired with the two pinholes. The two corresponding traces for the $10\times$ objective track each other up to 600 μm, however, indicating that a larger pinhole does not lead to an increase in detected scattered light that is sufficient to change the mean value of r. Therefore, there is a significant contribution from scattered light occurring even with optimal pinholes for higher NA objectives. In comparing Figure 4.2, A and B, it is clear that the $4\times$ objective returns a loss of anisotropy of 55% at 600 μm, while the $10\times$ for the same normalized pinhole diameter and depth yields an r decrease of 70%. This indicates that, at large depths, there is some discrimination against multiply scattered light provided by decreasing the NA, but it does not occur until 300 μm into the medium. This makes the option of intentionally degrading the NA to yield more accurate anisotropy values at depth unappealing, because the slight increase in the depth

at which r is recovered accurately occurs at the expense of diffraction-limited resolution.

Effect of varying the pinhole diameter

Given that the pinhole is the source of confocality, it is not surprising that this microscope parameter has the largest effect on the ability to accurately acquire anisotropy images in scattering media. As with any modification made to the imaging setup, there are always tradeoffs that determine what modifications may or may not be useful.

Panels B, C, and D from Figures 4.5-4.7 indicate that a pinhole limits the number of times a photon can be scattered and still be detected. The details of how this is accomplished are revealed by considering differences between excitation light scattering histograms under different conditions. Consider an image obtained at a depth of 100 μm in the presence of scatterers with two different phase functions (Figures 4.5C and 4.6C). Although photons traversing solutions for both bead sizes share the same fluorescence scattering mean free path, the distributions of scattering events in each case differs greatly. As noted previously, this occurs because we are scoring only those fluorescence photons that pass through the pinhole. Scattering histograms from the 0.1 μm beads maintain a sharp ballistic component regardless of pinhole size. With 0.511 μm beads, however, there is a relative decrease in the ballistic component with pinhole radius that ultimately shifts of the maximum likelihood of scattering from 0 to 1 scattering event.

Two measures of the difference between histograms for the two cases are shown in Figure 4.8. Figure 4.8A displays the relative likelihood of detecting fluorescence

excited by photons scattered once *vs.* those excited by ballistic photons. The ratio of the number of photons scattered once to the number of ballistic photons, N_1/N_0, is plotted as a function of pinhole radius for both bead sizes. This ratio is between 1.8 and 10 times higher with 0.511 μm beads compared to 0.1 μm beads. Figure 4.8B details the likelihood of detecting fluorescence excited by a multiply-scattered photon. In this case we report the ratio of photons scattered 10 times to ballistic photons, N_{10}/N_0. In contrast to panel A, the number of fluorescence photons originating from excitation photons scattered 10 or more times is higher in the presence of very small scatterers regardless of pinhole size. Interestingly, the ratio N_{10}/N_0 is a much better predictor of anisotropy degradation than is N_1/N_0.

Figure 4.8C displays the anisotropy as a function of pinhole radius for both scattering particle sizes. From this it is evident that the degradation of anisotropy is strongly tied to the existence of a long tail in the histograms of the number of scattering events. It is apparent why this is the case by considering the phase functions and the influence of particle size on polarization state. The high g exhibited for the 0.511 μm beads indicates that the light scattering is very forward directed. It is therefore likely that a photon scattered by these large particles would experience a small angular deflection. It is more likely that light encountering the smaller beads will scatter into a large angle, however. This explains why the number of photons reaching the detector that result from light scattered only once is much higher for the larger beads. The lower g for the smaller beads makes it more likely that a single scattering event will result in a scattering angle large compared to the acceptance angle of the objective lens.

The question remains as to why the relatively small number of excitation pho-
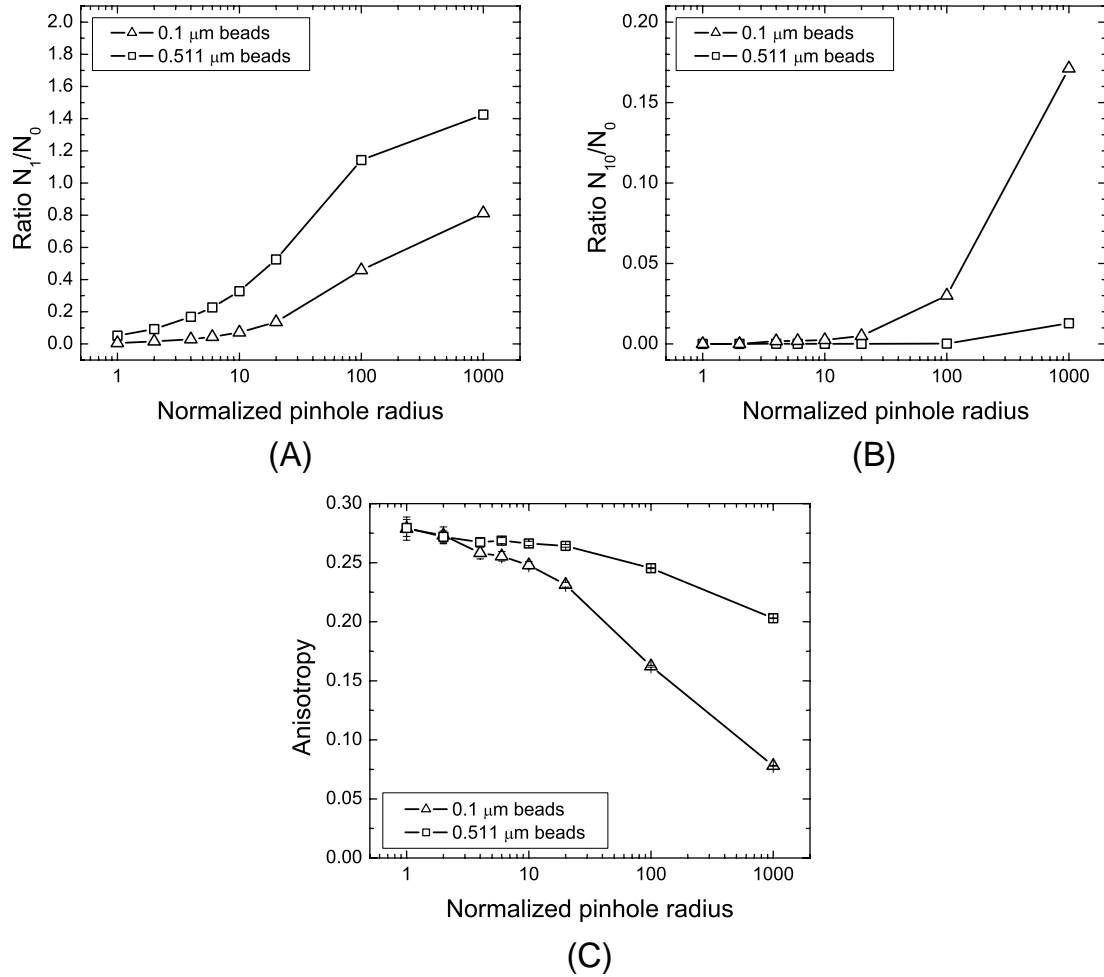
Figure 4.8: Monte Carlo results illustrating the change in the mean number of scattering events experienced by excitation photons that lead to detected fluorescence photons for a given pinhole size. Results are plotted for both 0.1 and 0.511 μm beads with a target located at a depth of 100 μm. A displays the ratio of the number of photons scattered once (N_1) to the number of ballistic (unscattered) photons (N_0). B contains the ratio of the number of photons scattered 10 times, N_{10}, to the number of ballistic photons. Panel C displays the mean anisotropy as a function of pinhole size for suspensions of both bead sizes. Error bars are standard error of the mean.

tons scattered 10 times appears to be the dominant factor in polarization degradation. This is a fact made even more curious given that, for a given scattering angle that is not very close to the forward direction, the 0.511 μm beads tend to alter the photon packet polarization state more than light scattered by smaller beads (data not shown). It would appear that this would result in more depolarization with scattering from the larger beads. However, to fully understand the observed behavior, the effect of depolarization from both one scattering event and multiple scattering events must be taken into account. Light scattered into the extreme forward direction maintains the incident polarization state. Consequently, even though light that is scattered a few number of times is detected more efficiently with the larger beads, the light is preferentially scattered into angles at which the polarization has not been modified. With the smaller beads a different effect comes into play. Even though the polarization tends to be maintained for any individual scattering event, the more uniformly distributed scattering phase function randomizes the light on the basis of direction changes. As a result, even though light that is scattered once is less likely to be detected, the lower g makes it more likely that light scattered many times will make it into the detection path. The geometry of the phantom setup probably contributes to this behavior, however, and had the system been constructed with scattering in the fluorescence layer this result might have been modified. The fluorescent target is purely absorbing, and therefore light that reaches the target cannot be scattered back into the detection acceptance angle. Because of the highly forward directed scattering from the larger beads, it is more likely that these photons will reach the target and will not experience large numbers of scattering events. It therefore appears that, for this

geometry, the number of scattering events experienced by detected light is more important than the depolarization induced by any individual scattering event.

Another important property to consider in anisotropy imaging is the simultaneous effect of pinhole size on SNR and scatter-induced r degradation. Changing the pinhole size alters the signal-to-noise ratio, which in the case of anisotropy imaging translates directly into the uncertainty in the mean value of r. Figure 4.9 is a plot of the mean anisotropy and standard error of the mean as a function of pinhole size for a target located 100 μm into a 0.511 μm bead suspension. For pinholes up to $10v_0$, the uncertainty in r decreases rapidly while there is only a modest 7% decrease in the mean. The relative immunity of r to pinhole size arises from the slow depolarization of light relative to changes in position at the pinhole plane [8]. There is, however, a limit to the increase in pinhole size that can be made before a statistically significant change in anisotropy occurs. In this case, for example, increasing the pinhole radius larger than $2v_0$ is not beneficial, as the degradation in r due to scattering becomes measurably different than that obtained with the optimal pinhole size. Modest increases in pinhole size may be warranted in cases where the signal is very dim and the corresponding reduction in image resolution is acceptable, however.

The depth to which accurate anisotropy images can be acquired is governed by the parameters of the microscope optics as well as the optical properties of the medium in which the target resides. Smaller pinholes and lower NA objectives are most effective at maintaining r at depth, but there are tradeoffs required in signal strength and resolution. Our experimental studies show that we can retrieve anisotropies accurate to within 10% at depths equal to 4-5 ℓ_s at the
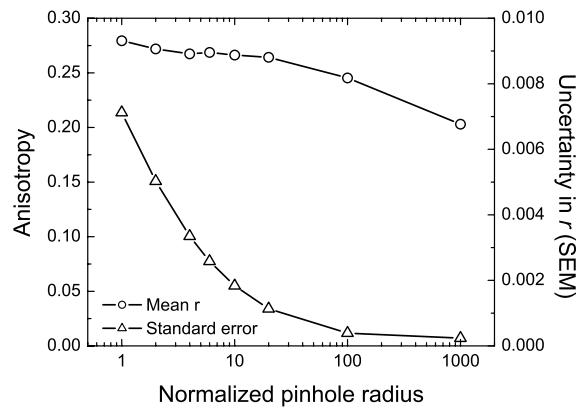
Figure 4.9: Monte Carlo simulations of the uncertainty in r measurements as a function of pinhole size. The mean anisotropy and standard error of the mean are shown for a target 100 μm deep into an aqueous suspension of 0.511 μm diameter polystyrene microspheres.

excitation wavelength and approximately 2 ℓ_s at the fluorescence wavelength with suitable pinholes. Since the scattering coefficient is approximately 2-fold higher at the excitation wavelength, this is the limiting factor in imaging. Scattering histograms in Figures 4.5-4.7 indicate that this is the case, as the scattering of excitation light leading to detected fluorescence photons dominates that of the fluorescence photons. This agrees with earlier studies by Gu *et al.* showing that the scattering of excitation light rather than of the fluorescence is the limiting factor in single-photon imaging [13]. This also appears to be the case for single-photon anisotropy imaging.

In this chapter we have considered the effects that microscope parameters have on anisotropy imaging, but an alternative technique that may prove effective deserves mention. Typically the sample of interest is thought about as a fixed parameter, but the use of red-shifted fluorophores allows imaging to progress in the presence of more advantageous optical properties. We excited the polymer bar at 488 nm and detected a peak wavelength at 590 nm. For the 0.1 μm beads this gave μ_s of 224 cm^{-1} and 101 cm^{-1} at the excitation and fluorescence wavelengths, respectively. If we had used a red-shifted dye such as Alexa 680, the optical properties encountered would have been significantly different. Alexa 680 has an absorption maximum at 655 nm and an emission maximum at 704 nm (Molecular Probes, Eugene, OR). If we had used this dye instead of the fluorophore-containing bar, the 0.1 μm beads would have given μ_s values of 68 cm^{-1} and 56 cm^{-1} at the excitation and emission wavelengths, respectively. This reduction in scattering at both wavelengths would aid in maintaining image quality and accuracy of r to greater depths. Although a slight degradation in the diffraction-limited perfor-

mance of the microscope would occur, it would likely be less important than the increase in scattered light performance.

4.5   Conclusions

We have shown that confocal fluorescence polarization imaging is a robust modality that yields anisotropy information accurate to within 10% to approximately $4\ell_s$ at the excitation wavelength into scattering media. In our experience this encompasses practically all depths at which we can acquire useful intensity images. The fact that the image quality and anisotropy fidelity are acceptable at the same depths is not surprising given that an inability to reject scattered light is the primary source of degradation in both cases.

As is the case with most imaging techniques, tradeoffs can be made in order to maximize any particular aspect of the technique. In the case of anisotropy imaging, the three important parameters available are image resolution, signal level, and the fidelity of the anisotropy. The returned anisotropy appears to be somewhat insensitive to pinhole size to within a few times the optimal size. This property may be exploited to boost signal strength if a particular sample is dim and requires an increase in signal. The increase in power will require resolution sacrifices to be made, but this must be decided on a case-by-case basis. Anisotropy imaging appears to be somewhat sensitive to the objective lens numerical aperture, and it appears that using lower NA objectives may preserve anisotropy information more accurately at depth than high NA lenses. These effects are extremely subtle at depths where quality images can be acquired, however, and any advantages low

NA objectives provide will almost certainly be offset by the loss of both in-plane and axial resolution.

References

[1] C. Smithpeter, A. Dunn, A. Welch, and R. Richards-Kortum, "Penetration depth limits of *in vivo* confocal reflectance imaging," Appl. Optics **37,** 2749–2754 (1998).

[2] J. Schmitt, A. Knuttel, and M. Yadlowsky, "Confocal microscopy in turbid media," J. Opt. Soc. Am. A **11,** 2226–2235 (1994).

[3] S. Schilders and M. Gu, "Limiting factors on image quality in imaging through turbid media under single-photon and two-photon excitation," Microsc. Microanal. **6,** 156–160 (2000).

[4] X. Gan, S. Schilders, and M. Gu, "Image formation in turbid media under a microscope," J. Opt. Soc. Am. A **15,** 2052–2058 (1998).

[5] X. Gan and M. Gu, "Fluorescence microscopic imaging through tissue-like turbid media," J. Appl. Phys. **87,** 3214–3221 (2000).

[6] X. Gan and M. Gu, "Effective point-spread function for fast image modeling and processing in microscopic imaging through turbid media," Opt. Lett. **24,** 741–743 (1999).

[7] X. Gan, S. Schilders, and M. Gu, "Combination of annular aperture and polarization gating methods for efficient microscopic imaging through a turbid medium: theoretical analysis," Microsc. Microanal. **3,** 495–503 (1997).

[8] F. C. MacKintosh, J. X. Zhu, D. J. Pine, and D. A. Weitz, "Polarization memory of multiply scattered light," Phys. Rev. B **40,** 9342–9345 (1989).

[9] X. Gan, S. Schilders, and M. Gu, "Image enhancement through turbid media under a microscope by use of polarization gating methods," J. Opt. Soc. Am. A **16,** 2177–2184 (1999).

[10] S. Morgan, M. Khong, and M. Somekh, "Effects of polarization state and scatterer concentration on optical imaging through scattering media," Appl. Optics **36,** 1560–1565 (1997).

[11] S. Hell, G. Reiner, C. Cremer, and E. Stelzer, "Aberrations in confocal fluorescence microscopy induced by mismatches in refractive index," J. Microsc. **169,** 391–405 (1993).

[12] J. D. Wilson, C. E. Bigelow, D. J. Calkins, and T. H. Foster, "Light scattering from intact cells reports oxidative-stress-induced mitochondrial swelling," Biophys. J. **88** (2005).

[13] M. Gu, S. Schilders, and X. Gan, "Two-photon fluorescence imaging of microspheres embedded in turbid media," J. Mod. Opt. **47,** 959–965 (2000).

Chapter 5

Imaging Enzyme Activity with Polarization-Sensitive Confocal Fluorescence Microscopy

5.1 Introduction

Chapters 3 and 4 were devoted to exploring the properties of confocal fluorescence polarization imaging in turbid media. The limits of the technique were found without regard to any particular application in order to maintain the generality of the results. In this chapter we turn our attention toward the development of a specific technique for imaging enzyme activity that is based on quantifying enzyme-induced anisotropy changes of fluorescently-labeled substrates.

The ability to image enzyme activity noninvasively has obvious broad applicability in biology. A particularly compelling example is that of cancer biology, where proteases play a critical role in cancer progression by participating in microinvasion and angiogenesis and by promoting metastatic growth of tumors at distant sites. A number of different proteases have been implicated in metastasis,

including cathepsin B, urokinase plasminogen-activating enzyme (uPA), and several of the matrix metalloproteinases [1, 2]. The role that each of these enzymes plays is complicated and interdependent on a number of factors, and as such the research into better understanding their contributions is a field of active study [3, 4]. The ability to image the spatial properties of enzyme production is a valuable tool for understanding these processes, and the use of polarization-sensitive fluorescence imaging provides a way to visualize these patterns.

Fluorescence anisotropy imaging techniques have already proven to be powerful and robust, and are widely applicable to a number of biological and biophysical problems. In one of the first papers to evaluate polarization-sensitive imaging, Axelrod studied carbocyanine dye orientation in individual erythrocyte ghosts [5]. Fluorescence polarization imaging has also been exploited for the measurement of local intracellular viscosity [6], imaging calmodulin binding in fibroblasts [7], measuring the orientation of eosin-5-maleimide on band 3 in erythrocyte ghosts [8], visualizing three dimensional order in liquid crystals [9], and for imaging the localization of the photosensitizer mTHPC (meta-tetrahydroxyphenylchlorin) in intact cells (see Chapter 6) [10].

There are currently several approaches available to optically image enzyme activity. These include imaging resonant energy transfer (RET) between enhanced yellow and cyan fluorescent proteins [11], detecting enzyme activity by fluorescence spectral shifts [12], and quenched near-infrared probes made fluorescent by enzyme activity [13]. The most prolific of these is the quenched probe approach wherein quenched near-infrared emitting probes emit fluorescence only after enzymatic cleavage has occurred, and fluorophores on the probe have been spatially

separated a distance sufficient to allow fluorescence emission. This technique has yielded a large family of papers investigating cathepsin D activity [14], matrix metalloproteinase-2 (MMP-2) activity and inhibition [15, 16], and a host of other enzyme probes listed in a minireview by Mahmood and Weissleder [17]. One pitfall of this technique is the possibility that a lack of substrate in the tissue of interest could be interpreted as a lack of enzyme activity, as these two possibilities both lead to no fluorescence signal. This problem has been addressed by recent papers from McIntyre *et al.* [18] and Kircher *et al.* [19], where a secondary reference fluorophore unaffected by enzyme activity has been added to eliminate any potential ambiguity. This approach has the consequence that two spectral regions are necessary to image the activity of one enzyme, and therefore inherently reduces the number of enzymes that can be detected simultaneously.

In this chapter we describe an alternate technique for imaging enzyme activity using steady-state fluorescence anisotropy measurements on a per-pixel basis with a confocal microscope. While anisotropy has been used as a fluorometer-based assay of enzyme activity in homogeneous solution [20–22] and in flow cytometry for quantifying processing of proteins in J774 murine macrophages [23], to the best of our knowledge it has not been implemented in an imaging context to report spatially resolved changes in anisotropy.

With the method presented here, enzyme activity is reported by changes in the fluorescence anisotropy of a fluorescently-labeled substrate (see Figure 5.1). A large molecule is labeled such that it inherently yields a high fluorescence anisotropy, and this construct is introduced into the region of interest. If no enzyme is present, the large molecular weight substrate remains intact and high

anisotropy is preserved (Figure 5.1A). If an enzyme is present for which the fluorescently labeled species is a substrate, however, the enzyme strips the fluorescent molecule from the larger structure resulting in a lower effective molecular weight and smaller τ_r (see equation 1.16). This yields a lower fluorescence anisotropy in regions containing enzyme as indicated in Figure 5.1B. The signature of enzyme activity in these images, therefore, is a region of anisotropy lower than that containing the construct alone.

We have demonstrated the efficacy of this approach by examining changes in anisotropy induced by trypsin and proteinase K with Bodipy-FL-labeled bovine serum albumin (BSA) attached to sepharose beads as the substrate. The beads were exposed to these enzymes, and the anisotropy was recorded in every pixel as a function of time. This procedure led to an image time course that yielded information about the enzyme activity in and around the beads. Measurements are also presented indicating the ability to image the effects of enzyme activity in living cells. For this, we incubated the J774 murine macrophage cell line with Bodipy-BSA and imaged the intercellular and intracellular variation of enzymatic processing of the probe.

5.2 Materials and methods

Cell imaging

J774 murine macrophages were grown in an 8-well chambered coverglass (Number 155411, Nalge Nunc International, Rochester, NY) containing 500 μL Dulbecco's modified eagle medium (D-MEM) with 10% fetal bovine serum supplemented with
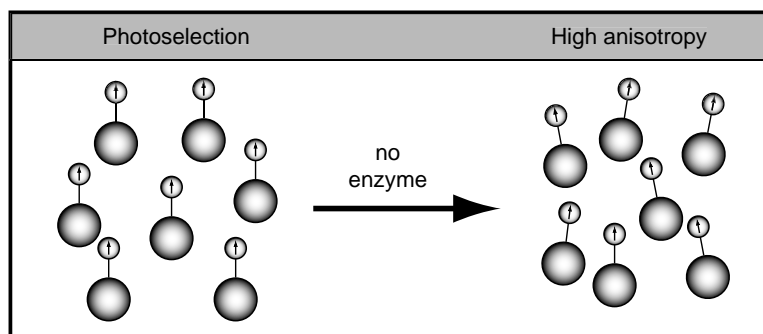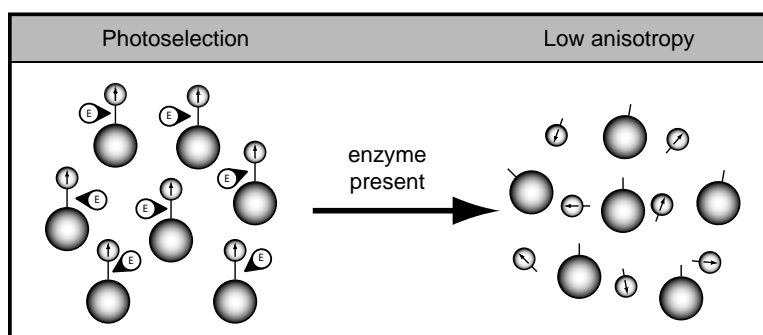
Figure 5.1: The basis of imaging enzyme activity using fluorescence polarization microscopy. (A) If a construct with a high inherent anisotropy is added to a system of interest containing no relevant enzyme, the anisotropy remains high. (B) If the construct in introduced in a region containing an enzyme for which it is a substrate, however, the enzyme cleaves the substrate and small fluorescently labeled fragments result. These smaller fragments can tumble more readily in solution and therefore yield a lower anisotropy.

penicillin-streptomycin. Cells were seeded at a concentration of 1×10^5 cells/well and placed in a 5% CO_2 incubator at 37° C for 48 hours. On the day of the experiment, 100 μg/mL Bodipy-BSA was added to the media and the cells were allowed to incubate for times ranging from 1 to 5 hours. At each time point the cells were rinsed $2\times$ in media, $1\times$ in Hanks' balanced salt solution (HBSS; Gibco, Grand Island, NY, USA), and then imaged in HBSS.

Bodipy-BSA in the cells was excited with 488 nm light from an argon-ion laser (Innova 70, Coherent Inc., Santa Clara, CA), and emission was filtered with a 500 nm long pass filter in the detection arm (HQ500LP, Chroma Technology Corp., Rockingham, VT). Images were acquired with a 10x, 0.45 NA objective every hour starting with the 1 hour time point and going up to 5 hours after introduction of the Bodipy-BSA. Both large (500 μm) and small (100 μm) fields of view were acquired to observe intracellular and intercellular variations in anisotropy.

Immobilization of substrate with sepharose beads

To demonstrate enzyme activity imaging in the bead model system, substrate localization was accomplished by attaching Bodipy-labeled BSA to cyanogen bromide activated sepharose 4B beads (Sigma-Aldrich, Inc., St. Louis, MO). The Bodipy-BSA (Molecular Probes, Eugene OR) was coupled to the beads at 1 mg/mL of swollen gel according to the manufacturer's instructions. The remaining active sites were blocked using 0.1 M ethanolamine (pH 9). The BSA-Bodipy was distributed homogeneously throughout the beads as evidenced by confocal fluorescence images.

Sepharose bead imaging sample preparation

The imaging sample was constructed using 1% agarose gel in HBSS. 200 mg agarose (Amresco Inc., Solon OH, USA) was added to 20 mL HBSS and the solution was heated until boiling. Once the gel had cooled to approximately 60° C, it was poured into a dish with a coverslip bottom to fill to a depth of approximately 4 mm. Prior to setting, a cloning cylinder (Bel-Art Products, Pequannock, NJ, USA) was placed in the gel, and 4 μL of the bead solution was injected in the region immediately adjacent to the cylinder. The agarose immobilized the beads once the gel had set at room temperature and was subsequently placed in a refrigerator at 8° C. Prior to imaging, the cloning cylinder was removed, leaving behind a well in the agarose encircled by immobilized beads.

Image acquisition with sepharose beads

Prior to introduction of enzymes, an initial image was acquired to establish baseline anisotropy and intensity. Subsequently, 100 μL of 15 mg/mL room temperature enzyme solution containing either trypsin (640 μM) or proteinase K (520 μM) was injected into the well. At the same time, a stage-mounted temperature controller (Bioptechs, Butler, PA, USA) was turned on to raise the dish temperature to 37° C, which was maintained for the duration of the experiment. Images were acquired at specified intervals from the time of heater activation up to one hour after enzyme addition.

Images were acquired with a 10×, 0.5 NA microscope objective in our custom built laser scanning confocal fluorescence imaging system described previously in

Chapter 2 [10, 24] and illustrated in Figure 2.1. Images were constructed from a 400×400 array of pixels spanning a $300 \ \mu$m field of view that required 20 seconds per image. An argon-ion laser tuned to 488 nm was the excitation source, and Bodipy fluorescence emission was filtered with a dichroic mirror and a 500 nm long pass filter (HQ500LP). The two orthogonal polarization components of the fluorescence were separated with a polarizing beamsplitting cube and sent to two balanced photomultiplier tubes. From these data it was possible to calculate the fluorescence anisotropy on a per-pixel basis.

Daily imaging calibration

While we were able to quantify the effects of objective lens NA on the measured anisotropy in Chapter 2, the effects of the polarization properties of all elements are not accounted for explicitly in that analysis. Other optical components in the system act to depolarize the beam, and they may be slightly different from day to day. To account for these factors and any daily variation, we performed a daily calibration to balance the throughput of the two polarization channels by imaging a reference sample of 1 μg/mL fluorescein in water with known anisotropy ($r = 0.0076$). From this, a correction factor, G, was calculated according to [25]

$$r_{ref} = \frac{i_\parallel - G i_\perp}{i_\parallel + 2 G i_\perp},$$

(5.1)

where $i_\parallel$ and $i_\perp$ were the raw parallel and perpendicular intensities. G was found for all pixels in the image by solving Equation 5.1 over the entire field of view. The mean value along one projection of this two dimensional correction factor was

fit with a degree 3 polynomial that was used as a noise-free G factor across the entire field of view.

Time-resolved lifetime and anisotropy data

To characterize the effects of enzyme action on the lifetime and anisotropy decays of our substrate-bound fluorophore, we performed time resolved measurements on Bodipy-BSA in fluid solution before and after proteinase K introduction. For the undigested substrate, we made measurements on 100 μL of 0.28 mg/mL Bodipy-FL-BSA in HBSS without any enzyme present. We also made the same measurements on 100 μL of the identical concentration of Bodipy-BSA that had been incubated in the presence of 0.49 mg/mL proteinase K at 37° C for one hour.

Time resolved fluorescence spectra and anisotropy decays using time correlated single photon counting were performed on an apparatus that has been described in detail elsewhere [26]. Briefly, fluorescence decays were measured using magic angle detection and fit with decay fitting software (SPCImage 2.4, Becker & Hickl GmbH, Berlin, Germany). For fitting we used the functional form,

$$F(t) = F_{baseline} + F_0 \sum_{i=1}^{n} a_i \exp(-(t - t_0)/\tau_i), \qquad (5.2)$$

where n is the number of components used, τ_i are the decay time constants, a_i are the amplitudes, $F_{baseline}$ is the baseline fluorescence and F_0 is the peak fluorescence at time t_0, where t_0 is the temporal offset of the fluorescence decay. The fitting routine effectively deconvolved the measured system response function. Amplitudes satisfy the condition that $\sum_{i=1}^{n} a_i = 1$ and the average lifetime $\langle \tau \rangle$ is

given by

$$\langle \tau \rangle = \sum_{i=1}^{n} a_i \tau_i \bigg/ \sum_{i=1}^{n} a_i. \tag{5.3}$$

For time-resolved fluorescence anisotropy, parallel $\big(I_\parallel(t)\big)$ and perpendicular $(I_\perp(t))$ fluorescence decays were measured for equal acquisition times during which there was no significant fluctuation in the signal level. The measured anisotropy decays were fit using [25, 27]

$$r(t) = \left(\frac{I_\parallel(t) - GI_\perp(t)}{I_\parallel(t) + 2GI_\perp(t)} \right) = r_\infty + \sum_{i=1}^{m} r_{0i} \exp(-t/\tau_{ri}), \tag{5.4}$$

with τ_{ri} the rotational correlation times, r_{0i} the initial anisotropies and r_∞ the initial anisotropies for the rotationally immobile fraction ($\tau_{ri} = \infty$). The average rotational correlation time for the mobile fraction is defined analogously to average lifetime in the form

$$\langle \tau_r \rangle = \sum_{i=1}^{m} r_{0i} \tau_{ri} \bigg/ \sum_{i=1}^{m} r_{0i}, \tag{5.5}$$

where the sum is over only the rotationally mobile components. The G-factor describes the sensitivity of detection to polarization and was determined experimentally using tail-matching for free fluorescein decays. Under our experimental conditions, the optical depolarization due to the microscope objective ($40\times$, 1.15 NA, with an underfilled back aperture) was negligible [5, 28].

5.3 Results

Enzyme activity imaging with sepharose beads

Demonstration of the imaging modality necessitated spatial confinement of the enzyme or the substrate. We chose to isolate the substrate in sepharose beads and allow the freely diffusing enzyme in fluid solution to permeate the entire field of view. After introducing the enzyme to the sample, a series of images acquired with a confocal microscope was taken, and the fluorescence anisotropy was calculated on a per-pixel basis. The two enzymes, trypsin and proteinase K, were chosen for their different specificities. Trypsin has greater substrate specificity, cleaving peptide bonds at the carboxyl side of lysine and arginine residues [29], whereas proteinase K has a broader specificity in that it cleaves at the carboxyl side of aliphatic and aromatic amino acids [30].

The results of the experiments in which BSA-Bodipy-labeled beads were exposed to proteinase K and trypsin are summarized in Figure 5.2. Figure 5.2, A and B, show anisotropy images taken 10 minutes after introduction of 640 μM trypsin and 520 μM proteinase K, respectively. The 45 μm regions of interest from which the plots in Figure 5.2, C–F, were derived are indicated on each image. It is clear from the images that the anisotropy inside the bead is lower after 10 minutes of exposure to proteinase K than after a similar exposure to trypsin, and this is confirmed by analysis presented in Figure 5.2, C and D.

Fig. 5.2, C and D, display analysis of data acquired from regions inside the beads. Here, the anisotropy is seen to fall much more rapidly initially with proteinase K than with trypsin, consistent with their different activities. Both

enzymes demonstrate a progressive decrease in r with time as the substrate is digested, although the magnitude is greater with proteinase K. The general intensity trend inside the beads is as expected. At early times, the intensity is high indicating a high concentration of fluorophore. As the enzymes act, the cleaved fragments are no longer attached to the bead and can therefore diffuse into the surrounding medium. The net effect of this release of fluorescent fragments is a loss in fluorescence inside the bead with time, and, as expected, the magnitude and rate of the intensity decrease with proteinase K is larger than that with trypsin.

The anisotropy changes inside the beads are larger in magnitude than those seen outside, but the percent changes induced by enzyme action are smaller inside the bead. This can be attributed to the presence of two distinct populations of labeled BSA inside the bead. A significant fraction of the measured fluorescence anisotropy arises from labeled BSA that remains attached to the bead. This subset provides a high anisotropy that remains constant if not slightly increasing for all times. Fragments that have already been cleaved and are no longer attached make up the other fraction of the signal inside the bead. These fragments contribute a lower anisotropy and are comprised of a distribution of fragment sizes.

The presence of at least two distinct fluorescent fragment populations inside the bead as well as a high degree of labeling lead to some complicated behavior. With both enzymes there is an initial decrease in the anisotropy that corresponds exactly with an increase in intensity (Figure 5.2, C and D). This sharp drop in anisotropy is probably a result of the first cleaved fragments coming off of the bead, while the increase in intensity is most likely due to a reduction in quenching of the fluorophore at high concentrations in the bead. Bodipy dyes are known to form
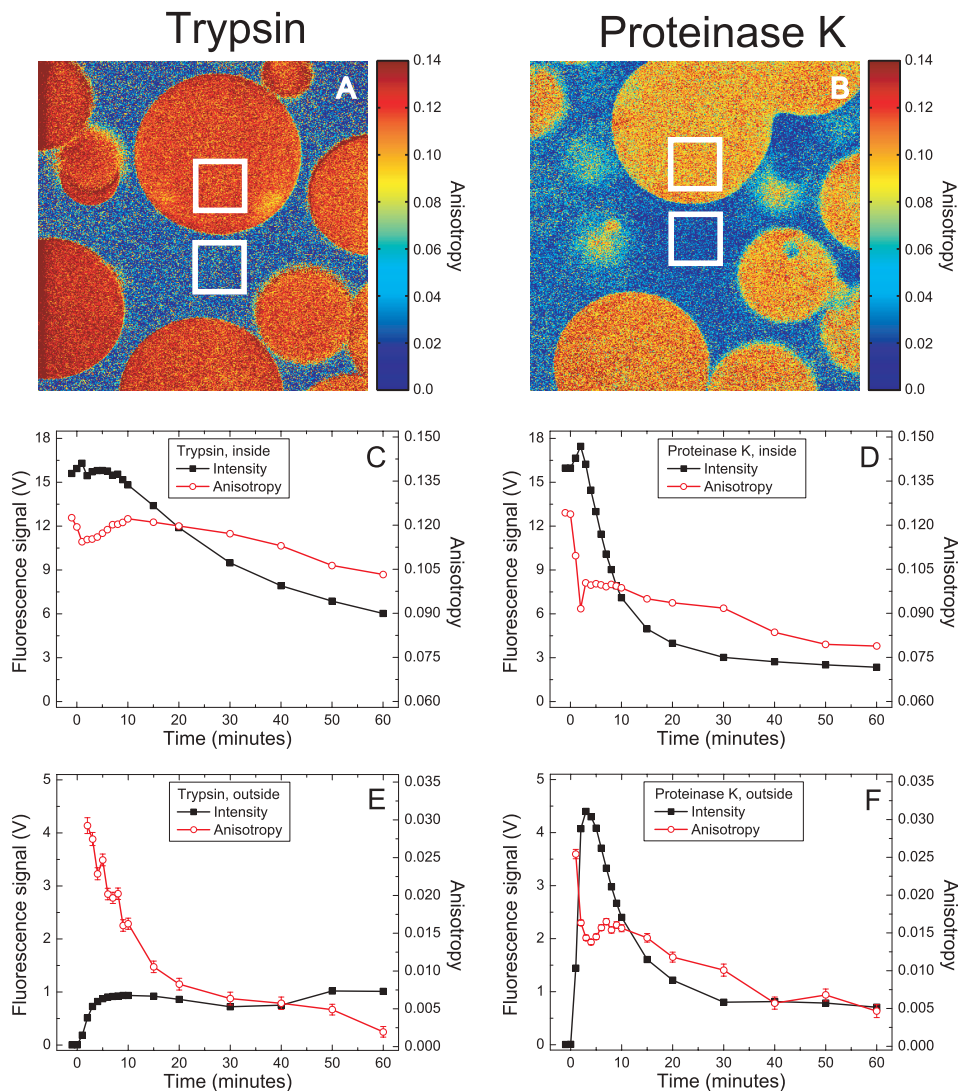
Figure 5.2: Results of fluorescence anisotropy images for BSA-Bodipy labeled beads after the addition of 15 mg/mL proteinase K and trypsin. The top images (A and B) show the 300 μm square anisotropy maps acquired 10 minutes after addition of the enzymes. The 45 μm square regions of interest inside and outside the beads are shown for each case. Results for the intensity and fluorescence anisotropy inside (C) and outside (E) the bead for trypsin are shown at left. The corresponding plots for proteinase K are shown in D and F. Data is presented from $t = -1$ minute (before enzyme was added) to $t = 60$ minutes after enzyme addition. Where omitted, error bars are smaller than the symbol. Anisotropy data is shown only for time points where fluorescence signal was sufficient for analysis.

nonfluorescent dimers at high concentrations [31], and cleavage of the BSA into smaller peptide chains would presumably separate some of these dimers and give rise to an increase in intensity. Near the 2 minute time point with both enzymes there is a decrease in total intensity that corresponds to an increase in anisotropy. These changes are more rapid with proteinase K than with trypsin, consistent with the differences in the activities of the two enzymes. The source of this transient increase in anisotropy in the bead interior is most likely explained by a reduction in resonance energy transfer (RET) occurring between adjacent Bodipy fluorophores [32]. Because an acceptor's emission dipole moment will in general not be collinear with that of the RET donor, as RET decreases it becomes less likely that the relative orientations of a donor-acceptor pair will rotate the polarization of the emitted fluorescence and therefore decrease the anisotropy. An earlier onset of the reduction in quenching as compared to reduction in homo-RET is expected as the distances of action of the two are quite different. Whereas dimer formation requires a separation of just a few angstroms, the Förster radius of Bodipy is 57Å [33]. Consequently, the effects of reduced quenching are observed first as increased fluorescence intensity as the fluorophores are separated by cleavage. As the separation between fragments grows larger, the reduction in RET is observed as a transient increase in anisotropy. After the effects of quenching and RET disappear, the intensity and anisotropy both decrease as the fragments diffuse out of the beads.

Figure 5.2, E and F, displays data acquired from regions outside the beads. Here, the anisotropy decreases much more rapidly initially with proteinase K than with trypsin. Initial anisotropy values are also lower for proteinase K as a result

of its more aggressive nature. In the time required to obtain the first anisotropy map, the fluorescence anisotropy has already decreased more with the less specific enzyme. Both enzymes demonstrate a decrease in r with time.

The trends observed with anisotropy in the medium outside the beads are validated by the corresponding intensity measurements. At the time of enzyme addition, the intensity in both cases is zero, with all of the Bodipy-BSA bound to the bead. An increase in intensity follows as the fluorescently-labeled fragments separate from the bead via enzymatic cleavage and diffuse into the surrounding medium. The magnitude of the fluorescence intensity and the rate of intensity increase with proteinase K are larger than that seen with trypsin. In the proteinase K case, after the three minute time point the intensity outside of the beads falls as fluorescent fragments cleaved from the beads diffuse out of the field of view into the much greater volume of the surrounding agarose. This rapid diffusion of the small fragments out of the region of interest probably leads to an underestimation of the magnitude of the true change in anisotropy. The decrease in intensity outside of the beads is not seen with trypsin, potentially because the slower rate of cleavage from the bead tends to balance the effects of diffusion to yield a nearly constant intensity after the 5 minute time point. The disparity in specificity between the enzymes is consistent with these outcomes, as a larger source term inside the bead would necessarily give rise to more product diffusing per given time outside the bead and an earlier onset of depletion of fluorescence inside the bead.

It is important to note that the actual anisotropy outside the bead does not depend on intensity as predicted from equation 1.12. The proteinase K image yields an anisotropy that falls in conjunction with the intensity after the 8 minute

time point. The trypsin case exhibits opposite behavior in that the anisotropy decreases while the intensity makes positive and negative deviations from the value observed at 10 minutes. It is clear, therefore, that we observe real changes in anisotropy arising from enzyme activity.

Time-resolved lifetime and anisotropy

Since the effects of the fluorescence lifetime and rotational correlation time share equal importance in determining the measured steady state anisotropy (equation 1.17), the effects of enzyme activity on both of these quantities must be understood to properly interpret the results. Enzymatic cleavage of a labeled substrate may lead to changes in the environment of the fluorophore to which it is attached in addition to decreasing the size of the labeled fragments. Thus, it is possible that a decrease in the fluorescence lifetime coupled with a decrease in rotational correlation time could act together in such a way as to leave the measured steady state anisotropy unchanged after digestion of the substrate. Conversely, an increase in τ coupled with a decrease in τ_r could magnify the enzyme-induced steady state anisotropy change and therefore make the technique more sensitive. Testing of both of these effects independently is done effectively by making time-dependent measurements of the fluorescence anisotropy and lifetime pre- and post-digestion. By fitting the intensity and anisotropy decay curves, the fluorescence lifetime and rotational correlation times pre- and post-digestion are determined.

Magic angle time-dependent fluorescence results are displayed in Figure 5.3A with and without proteinase K. The fluorescence lifetime of the bound Bodipy-FL shows a clear dependence on the state of the serum albumin. The lifetime of the
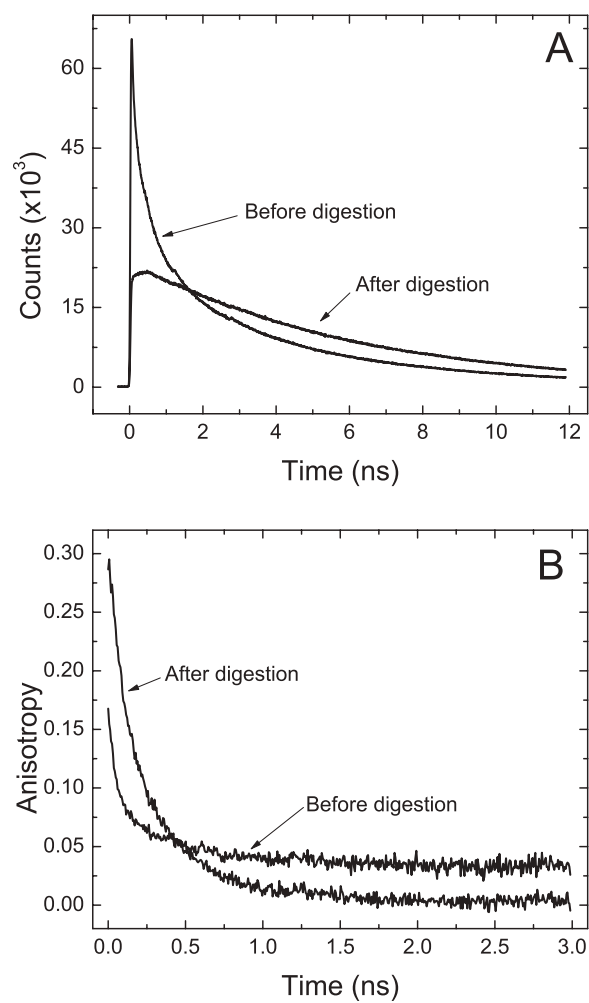
Figure 5.3: Results of fluorescence lifetime and time resolved anisotropy measurements. (A) Magic angle measurements of fluorescence lifetime in 0.28 mg/mL BSA-Bodipy before addition of proteinase K and after one hour in the presence of 0.49 mg/mL proteinase K at 37° C. (B) Anisotropy decay data acquired in the same sample is shown before and after enzymatic digestion.

Bodipy-BSA without enzyme present is fit best with a three term exponential decay with an average lifetime of 1.34 ns. After one hour of enzyme action, the observed average fluorescence lifetime increases more than four-fold to 5.98 ns with a mono-exponential decay. These effects are presumably due to alteration of nonradiative paths available to the Bodipy as the proteinase K acts, and are similar to effects observed with FITC-labeled BSA [34]. Interestingly, the lifetime increase drives the anisotropy lower than it would have been with rotational correlation changes alone.

Figure 5.3B shows the time resolved anisotropy decay data associated with the enzyme activity. Before enzyme addition, $r(t)$ is fit with a three-term exponential that yields $\langle \tau_r \rangle = 1.13$ ns. After digestion, the anisotropy decay becomes simpler and more than a factor of four times more rapid with a bi-exponential decay that yields $\langle \tau_r \rangle = 0.27$ ns, indicating digestion of the substrate. The presence of the multi-exponential decay indicates that there is segmental motion of the fluorophore in addition to larger scale rotation governed by the size of the polypeptide to which it is bound.

Images of J774 BSA processing

Demonstration of enzyme activity imaging in a relevant biological system was accomplished with enzymatic digestion of Bodipy-BSA by J774 murine macrophages. Images of a given field of view at any time point from 1 to 5 hours after incubation with Bodipy-BSA-containing media display appreciable anisotropy variations. Both inter- and intracellular variations are observed at all time points, and in extreme cases cells that are adjacent to one another display mean anisotropies

differing by factors of 2 to 3. A representative image acquired at the 5 hour time point is shown in Figure 5.4 that clearly indicates this heterogeneity.

Weaver *et al.* performed Western blot analyses and showed that anisotropy changes observed in J774 cells using flow cytometry were attributable to proteolytic degradation of FTIC-labeled BSA [23]. The anisotropy differences we observe are therefore also likely attributable to proteolytic processing of the BSA. Other information acquired from the images also indicates that this is the case. In any given field of view we observe intercellular brightness differences that can vary by factors of 3 or more. Weaver *et al.* attributed these intercellular brightness variations to differences in the stage of BSA processing in the cells. They used a FITC-labeled BSA as their probe, and they noted that there was an appreciable increase in brightness upon digestion. We also observe an increase in brightness of our Bodipy-BSA probe with enzymatic action, so we may be imaging the same effect that Weaver *et al.* found in their flow cytometry measurements.

Analysis of the mean anisotropy across the entire population of cells at each time point, however, does not yield any statistically significant anisotropy changes in the J774 cells. Weaver *et al.* found an approximately 20% decrease in anisotropy from 1 hour to 5 hours, so we had anticipated a similar change [23]. The nature of imaging yields additional information about the intracellular processing of proteins, but it is restricted to relatively small fields of view. It is therefore more labor intensive to analyze the same number of cells with our imaging technique compared to flow cytometry, an effect that was also mentioned by French *et al.* in an imaging study of enzyme-induced fluorescence lifetime changes [34]. We had approximately 2 orders of magnitude fewer cells in our imaging analysis than did
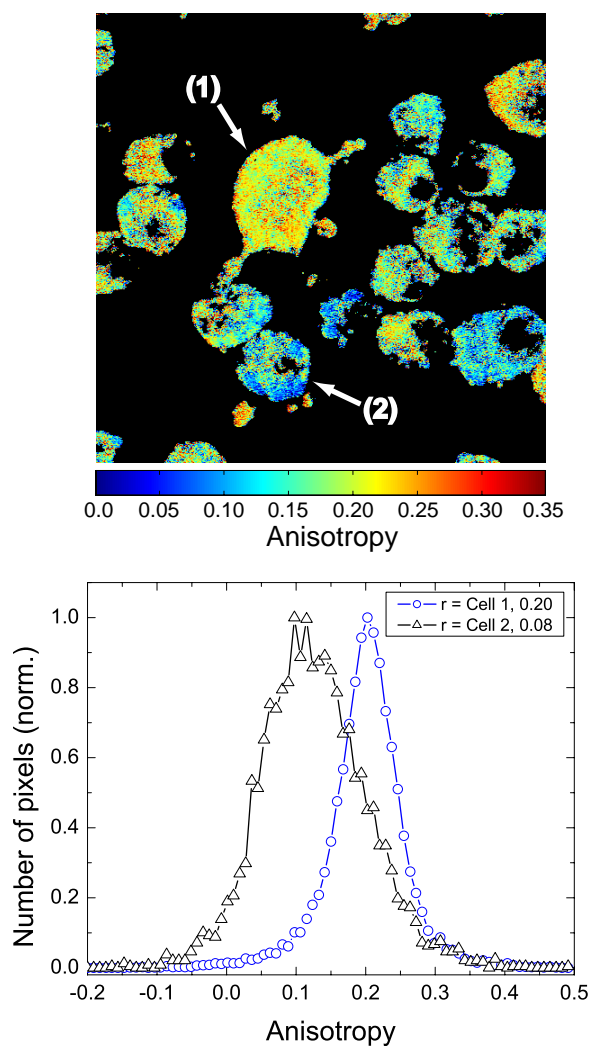
Figure 5.4: Fluorescence anisotropy image and histograms from J774 cells incubated in media containing Bodipy-BSA. The image was acquired over a 100 μm field of view with a 10×, 0.45 NA objective 5 hours after removal from the Bodipy-BSA-containing media. The plot displays a histogram of the anisotropy in all pixels within cells 1 and 2 (indicated in the image). The difference in anisotropy reflected by the color map in the image is unambiguously shown in the plot, where the histograms indicate that the mean anisotropies for cell 1 and 2 were 0.20 and 0.08, respectively.

Weaver *et al.* using flow cytometry, and given that their errors were significant even for that quantity, the fact that we did not see an appreciable effect is not surprising. Repeating the experiment with more cells would enable a more rigorous comparison between the two sets of results.

5.4   Discussion

We have demonstrated the efficacy of confocal fluorescence polarization microscopy as a tool for imaging enzyme activity. The technique is robust for a wide range of objective numerical apertures both on- and off-axis across reasonable fields of view as shown in Chapter 2. At sufficiently high SNR, relative changes in r less than 0.4% can be resolved, which is much smaller than differences we observe in sepharose beads and in J774 cells.

Although the BSA-Bodipy construct served as an appropriate test substrate for the experiments presented here, it was obviously not designed to measure the activities of these particular enzymes. Interestingly however, this construct did possess properties that contributed to its effectiveness. Specifically, the time-resolved experiments showed that enzymatic digestion led to the anticipated reduction in τ_r with a simultaneous increase in τ. This increase resulted in a nearly four-fold additional decrease in r than would have been observed had the lifetime not changed and the r measurements relied solely on changes in τ_r. One could therefore consider designing a specific probe utilizing the same basic principles as exhibited by the BSA construct but tailored to optimize the technique. Ideally these optimized probes would consist of a fluorescent portion attached to a

fluorescently silent large molecule with a linker cleavable only by the particular enzyme of interest. This approach increases the sensitivity of the measurement, as there would be a single-valued large change in anisotropy for the fluorescent products in contrast to the distribution of fragment sizes encountered with BSA.

There are a number of challenges associated with the use of fluorescence anisotropy to image enzyme activity. Measuring anisotropy is particularly sensitive to signal-to-noise issues, as expected from the operation involved in its calculation (see equation 1.12). It is therefore necessary to be especially vigilant in reducing instrumental noise when adopting this technique. With an appreciable signal-to-noise ratio, however, the relative errors in anisotropy can be reduced to under 0.4% as shown in Figure 2.4. A related challenge is the dilution of the anisotropy change in a pixel that results from the diffusion of the small, cleaved fluorescent fragments. With cleavage of the substrate, the smaller products tend to diffuse away faster than the larger, intact fragments, yielding a higher measured anisotropy than would be reported in the absence of diffusion. It is interesting to consider alternative constructs that would allow changes in anisotropy to occur without the creation of a freely diffusible fluorescent moiety. Finally, it is important in practical use to consider effects of highly labeled substrates for use as a probe. As demonstrated in Figure 5.2, C and D, substrates which have a high degree of labeling can yield complicated results that could obscure anisotropy changes due to enzyme activity. Specifically, a high degree of labeling could produce an initial increase in fluorescence anisotropy with enzyme activity rather than the anticipated decrease. At longer times the anisotropy will likely drop as shown in Figure 5.2, however. If it is suspected that these effects are occurring,

there may be corresponding intensity changes indicating that the substrate is too highly labeled, as observed in the complicated behavior at early times displayed in Figure 5.2. It will therefore be important in practice to use constructs with appropriate labeling to circumvent the confounding effects of RET and/or quenching, depending on the fluorophore utilized.

As discussed in Chapter 2, the artificial lowering of observed anisotropy by high NA objectives places limits on spatial resolution when accurate anisotropy values are required for enzyme activity imaging. However, even numerical apertures that cause depolarization could in principle be used in situations where detecting only relative anisotropy differences is important. The absolute anisotropy changes will not be as large as with a lower numerical aperture lens, but the optical resolution will of course be increased. As with any measurement, these trade offs between accuracy in the anisotropy determination and image resolution must be resolved on a case-by-case basis.

Experiments performed with J774 cells indicate that the imaging technique can readily image cellular variations in anisotropy due to proteolytic processing of enzyme constructs. Our results are similar to those of Weaver *et al.* in flow cytometry, which leads us to believe our imaging technique is performing well. The analysis presented here indicates that analyzing protein processing by macrophages is effectively performed on a per-cell basis in flow cytometry, as intercellular anisotropy variations are more significant that intracellular variations. The efficacy of the imaging technique is a promising result, because the ultimate use will be in excised tissue or *in vivo* where microscopic variations in enzyme activity may be important. It is the hope that such images will yield very early

information about the nature of a particular lesion and what treatment strategies are most appropriate.

With technical challenges met and constraints appreciated, steady-state fluorescence anisotropy as an enzyme imaging modality has many attractive features. Modifications to a conventional confocal microscope that are necessary to implement the technique are relatively straightforward and involve few additional components. We were able to upgrade our confocal fluorescence microscope to perform polarization imaging with the incorporation of a linear polarizer, polarizing beamsplitter and one additional photomultiplier tube. Second, unlike the quenched probes of enzyme activity that are optically silent until the enzyme acts, probes based on anisotropy are always fluorescent, enabling the distribution of the probe in a complex sample to be determined with no additional measurements. This feature, which is also addressed by the two-color quenched probe constructs introduced recently by McIntyre *et al.* [18], removes an important potential ambiguity in cases where no signal is detected from a quenched probe of enzyme activity. A related point is that the determination of the mean r is inherently insensitive to fluorescence intensity, subject to the constraint that there is abundant signal available. As a result, a measurement of enzyme activity based on anisotropy is insensitive to inhomogeneities in construct distribution within the sample, even though these will be apparent through the inherently fluorescent nature of the substrate. Finally, as a result of the simultaneous two-channel detection scheme, the anisotropy images require the same acquisition time as a single intensity image. Rapid image acquisition on the order of seconds enables time-dependent processes to be sampled several times per minute. The most obvious

benefit, however, is that this assay of enzyme activity is an imaging technique. This allows spatiotemporal sequences to be assembled that not only positively identify the presence of an enzyme, but that can ideally map the influence of an enzyme on a subcellular length scale.

References

[1] A. F. Chambers and L. M. Matrisian, "Changing views of the role of matrix metalloproteinases in metastasis," J. Natl. Cancer Inst. **89,** 1260–1270 (1997).

[2] M. Lee, R. Fridman, and S. Mobashery, "Extracellular proteases as targets for treatment of cancer metastases," Chem. Soc. Rev. **33,** 401–409 (2004).

[3] L. Coussens, B. Fingleton, and L. Matrisian, "Matrix metalloproteinase inhibitors and cancer: Trials and tribulations," Science **295,** 2387–2392 (2002).

[4] J. Rao, "Molecular mechanisms of glioma invasiveness: the role of proteases," Nat. Rev. Cancer **3,** 489–501 (2003).

[5] D. Axelrod, "Carbocyanine dye orientation in red cell membrane studied by microscopic fluorescence polarization," Biophys. J. **26,** 557–573 (1979).

[6] J. Dix and A. Verkman, "Mapping of fluorescence anisotropy in living cells by ratio imaging. Application to cytoplasmic viscosity," Biophys. J. **57,** 231–240 (1990).

[7] A. Gough and D. Taylor, "Fluorescence anisotropy imaging microscopy maps calmodulin binding during cellular contraction and locomotion," J. Cell Biol. **121,** 1095–1107 (1993).

[8] S. Blackman, C. Cobb, A. Beth, and D. Piston, "The orientation of eosin-5-maleimide on human erythrocyte band 3 measured by fluorescence polarization microscopy," Biophys. J. **71,** 194–208 (1996).

[9] I. Smalyukh, S. Shiyanovskii, and O. Lavrentovich, "Three-dimensional imaging of orientational order by fluorescence confocal polarizing microscopy," Chem. Phys. Lett. **336,** 88–96 (2001).

[10] C. E. Bigelow, D. L. Conover, and T. H. Foster, "Confocal fluorescence spectroscopy and anisotropy imaging system," Opt. Lett. **28,** 695–697 (2003).

[11] P. W. Vanderklish, L. A. Krushel, B. H. Holst, J. A. Gally, K. L. Crossin, and G. M. Edelman, "Marking synaptic activity in dendritic spines with a calpain substrate exhibiting fluorescence resonance energy transfer," Proc. Natl. Acad. Sci. USA **97,** 2253–2258 (2000).

[12] C.-H. Tung, Q. Zeng, K. Shah, D.-E. Kim, D. Schellingerhout, and R. Weissleder, "*In vivo* imaging of *β-galactosidase* activity using far red fluorescent switch," Cancer Res. **64,** 1579–1583 (2004).

[13] R. Weissleder, C.-H. Tung, U. Mahmood, and A. Bogdanov, "*In vivo* imaging of tumors with protease-activated near-infrared fluorescent probes," Nat. Biotechnol. **17,** 375–378 (1999).

[14] C. Tung, U. Mahmood, S. Bredow, and R. Weissleder, "*In vivo* imaging of proteolytic enzyme activity using a novel molecular reporter," Cancer Res. **60,** 4953–4958 (2000).

[15] C. Bremer, S. Bredow, U. Mahmood, R. Weissleder, and C. Tung, "Optical imaging of matrix metalloproteinase-2 activity in tumors: Feasibility study in a mouse model," Radiology **221,** 523–529 (2001).

[16] C. Bremer, C.-H. Tung, and R. Weissleder, "*In vivo* molecular target assessment of matrix metalloproteinase inhibition," Nature Med. **7,** 743–748 (2001).

[17] U. Mahmood and R. Weissleder, "Near-infrared optical imaging of proteases in cancer," Mol. Cancer Ther. **2,** 489–496 (2003).

[18] J. McIntyre, B. Fingleton, K. Wells, D. Piston, C. Lynch, S. Guatam, and L. Matrisian, "Development of a novel fluorogenic proteolytic beacon for *in vivo* detection and imaging of tumor-associated matrix metalloproteinase-7 activity," Biochem. J. **377,** 617–628 (2004).

[19] M. F. Kircher, R. Weissleder, and L. Josephson, "A dual fluorochrome probe for imaging proteases," Bioconjugate Chem. **15,** 242–248 (2004).

[20] H. Maeda, "Assay of Proteolytic-Enzymes by the Fluorescence Polarization Technique," Anal.Biochem. **92,** 222–227 (1979).

[21] R. Bolger and W. Checovich, "A New Protease Activity Assay Using Fluorescence Polarization," Biotechniques **17,** 585–589 (1994).

[22] S. Schade, M. Jolley, B. Sarauer, and L. Simonson, "BODIPY-alpha-casein, a pH-independent protein substrate for protease assays using fluorescence polarization," Anal. Biochem. **243,** 1–7 (1996).

[23] D. Weaver, G. Durack, and E. Voss, "Analysis of the intracellular processing of proteins: application of fluorescence polarization and a novel fluorescent probe," Cytometry **28,** 25–35 (1997).

[24] C. E. Bigelow, C. J. Harkrider, D. L. Conover, T. H. Foster, I. Georgakoudi, S. Mitra, M. G. Nichols, and M. Rajadhyaksha, "Retrofitted confocal laser scanner for a commercial inverted fluorescence microscope," Rev. Sci. Instrum. **72,** 3407–3410 (2001).

[25] J. R. Lakowicz, *Principles of Fluorescence Spectroscopy*, 2nd ed. (Kluwer Academic/Plenum Publishers, New York, 1999).

[26] A. Heikal, S. Hess, and W. Webb, "Multiphoton molecular spectroscopy and excited state dynamics of enhanced green fluorescent protein (EGFP): acid-base specificity," Chem. Phys. **274,** 37–55 (2001).

[27] D. O'Connor and D. Phillips, *Time-Correlated Single Photon Counting* (Academic Press, London, 1984).

[28] D. Axelrod, "Fluorescence polarization microscopy," Methods Cell Biol. **30,** 333–352 (1989).

[29] D. Voet and J. Voet, *Biochemistry* (John Wiley & Sons, New York, 1995).

[30] W. Ebeling, N. Hennrich, M. Klockow, H. Metz, H. Orth, and H. Lang, "Proteinase K from *Tritirachium album* Limber," Eur. J. Biochem. **47,** 91–97 (1974).

[31] F. Bergström, I. Mikhalyov, Hägglöf, R. Wortmann, T. Ny, and L. B. Å. Johansson, "Dimers of dipyrrometheneboron difluoride (BODIPY) with light spectroscopic applications in chemistry and biology," J. Am. Chem. Soc. **124,** 196–204 (2002).

[32] I. D. Johnson, H. C. Kang, and R. P. Haugland, "Fluorescence and absorption spectroscopic properties of dipyrrometheneboron difluoride (BODIPY) derivatives in liquids, lipid membranes, and proteins," Anal. Biochem. **198,** 228–237 (1991).

[33] I. Mikhalyov, N. Gretskaya, F. Bergström, and L. B. Å. Johansson, "Electronic ground and excited state properties of dipyrrometheneboron difluoride (BODIPY): Dimers with application to biosciences," Phys. Chem. Chem. Phys. **4,** 5663–5670 (2002).

[34] T. French, P. So, D. Weaver, T. Coelho-Sampaio, E. Gratton, E. Voss, and J. Carrero, "Two-photon fluorescence lifetime imaging microscopy of macrophage-mediated antigen processing," J. Microsc. **185,** 339–353 (1997).

Chapter 6

Future Directions and Other Applications

Previous chapters have been devoted to exploring the limits of confocal fluorescence polarization microscopy in scattering media and to introducing a new technique for imaging enzyme activity with fluorescence anisotropy. In this chapter we discuss our work on other promising applications for anisotropy imaging that have the potential to add significantly to fields in which they apply. First we discuss a technique for discriminating contaminating cellular autofluorescence from signals of interest by exploiting differences in anisotropy. We also describe work our group has undertaken to image the polarization of fluorescence emitted from photodynamic therapy (PDT) agents in cells. Application of polarization to this regime has proven to yield information not accessible to conventional fluorescence imaging. Finally, we revisit the application of anisotropy imaging to enzyme activity by exploring two areas of future investigation. The first is the design of new exogenously applied anisotropy constructs that are specific in their response to a particular enzyme. We also propose a potentially powerful method for imaging enzyme activity that is based on images of bright autofluorescence.

In the future this may be a useful tool in understanding the roles enzymes play in cancer progression.

6.1   Discriminating against autofluorescence

Under ideal conditions in fluorescence imaging of exogenous labels, autofluorescence is sufficiently dim compared with targets of interest that it is possible to ignore the autofluorescence altogether. In certain tissue types and especially when exciting with shorter excitation wavelengths, however, autofluorescence can be comparable in intensity to the signal of interest and yield compromised images. There are various strategies for coping with this problem, including shifting the excitation wavelength to excite autofluorescence less efficiently, increasing the brightness of the target, or switching to longer wavelength emitters that do not spectrally overlap with the autofluorescence. Often switching excitation wavelengths is not possible as filter cubes and laser sources are somewhat inflexible, and increasing the labeling on targets is not always feasible. Utilizing fluorophores with red-shifted peaks is effective, but this often requires sacrificing the highly valuable green spectral region that encompasses emission from such widely used fluorophores as green fluorescent protein (GFP) and fluorescein.

Fluorescence polarization imaging offers a potential solution to this problem for cases in which the target and autofluorescence have much different anisotropies. This approach avoids the spectral overlap issue, as anisotropy relies only on differences in the ratio of fluorescence lifetime to rotational correlation time (see equation 1.17). There are two particularly compelling fluorescence labeling schemes for which exploiting differences in r is appealing: GFP and fluorescently-labeled

antibodies. The fluorescence lifetime and rotational correlation time of GFP yield a high value for r in the range 0.275-0.325 [1–3]. For cases in which r for the background is low, this approach has been shown to be effective in discriminating GFP from autofluorescence in the context of microplate readers by Knight *et al.* [2]. For fluorescently-labeled antibodies a high anisotropy is also expected, the magnitude of which depends on the fluorescence lifetime of the fluorophore and molecular weight of the antibody. As an example, consider immunoglobulin G (IgG) labeled with fluorescein. IgG has a molecular weight of 150 kDa [4], and fluorescein has a fluorescence lifetime of approximately 4 ns [5], so equation 1.17 predicts that IgG labeled with fluorescein should yield $r \approx 0.36$. In cases where the background autofluorescence anisotropy is low, this high number will be readily apparent in anisotropy maps.

In order to demonstrate the promise of the technique in the context of confocal imaging, we used the approach to discriminate GFP from fluorescein. EMT6 cells were transfected with DNA for GFP under the control of the cytomegalovirus (CMV) promoter, which results in high levels of GFP throughout most of the cell. Fluorescein, whose absorption and emission spectra are similar to those of GFP but with an anisotropy of approximately 0.008, was dissolved into the extracellular medium. A conventional confocal fluorescence image of the cell monolayer is shown in Figure 6.1A. Intense fluorescence from the fluorescein solution obscures the intracellular GFP fluorescence, but an image exploiting the difference in anisotropies should separate the contributions of these two species. Such an image is shown in Figure 6.1B, which is computed from the subtraction $I_{\parallel} - I_{\perp}$. Since fluorescein has a low anisotropy, $I_{\parallel}$ and $I_{\perp}$ are approximately equal and
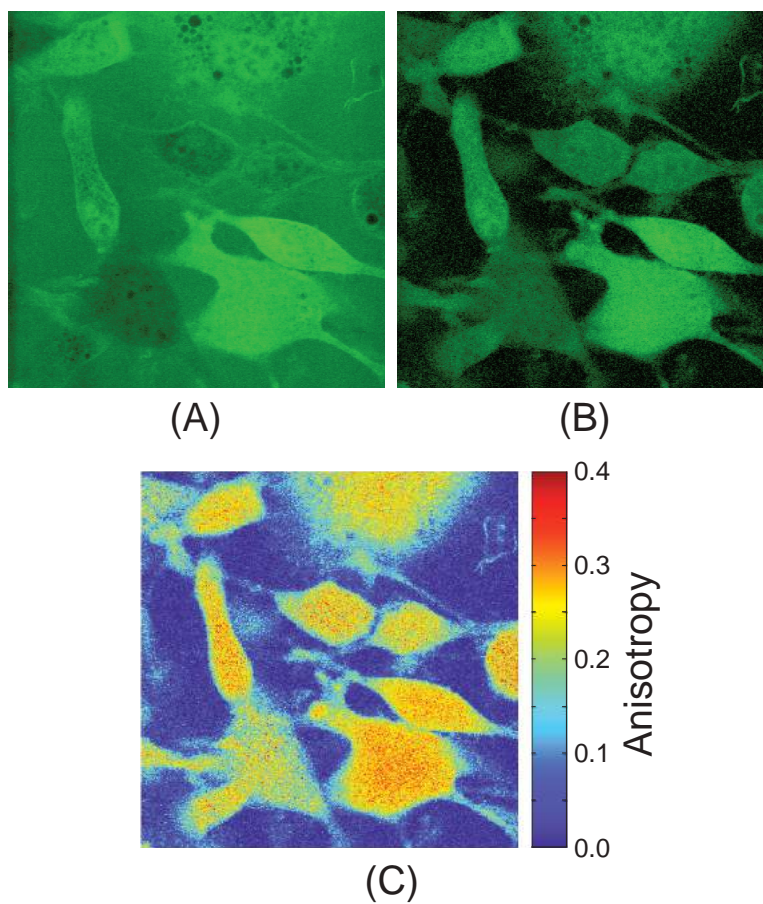
Figure 6.1: Polarization-sensitive imaging discriminates between two fluorophores with similar emission spectra but different anisotropies. GFP-expressing EMT6 cells were immersed in media containing 0.4 μg/mL fluorescein. The conventional confocal fluorescence image is shown in A. Subtraction of $I_\parallel - I_\perp$ yields the image shown in B, where we exploit the large difference in anisotropy between GFP and fluorescein to discriminate against the fluorescein signal. The anisotropy map derived from the polarization-sensitive images is shown in C. Images are 100 $\times$ 100 μm.

extracellular pixels containing fluorescein are near zero after subtraction. This is not true for pixels containing GFP, as $I_{\parallel} > I_{\perp}$, and appreciable signal is left after subtraction. The anisotropy map in Figure 6.1C demonstrates regions of high intracellular anisotropy ($r \approx 0.3$), and extracellular anisotropies close to zero as anticipated for fluorescein.

6.2 Photosensitizer anisotropy imaging

The efficacy of PDT sensitizers is dependent on a number of factors including the intracellular localization of the drug [6]. Since anisotropy imaging reveals information about the drug distribution and its local environment, we applied the technique to investigate the distribution of meta-tetrahydroxyphenylchlorin (mTHPC), a potent PDT agent.

Confocal fluorescence images of EMT6 cells incubated with 5 μg/mL mTHPC for 24 hours are shown in Figure 6.2. The conventional confocal image ($\lambda_{ex} = 514$ nm) shows localization of the bright photosensitizer fluorescence in the region surrounding the cell nucleus, which is dark due to dye exclusion (Figure 6.2A). This distribution is consistent with earlier studies indicating that mTHPC localizes in the golgi apparatus and endoplasmic reticulum [7, 8]. Figure 6.2B contains an anisotropy map computed from the two polarizations that exhibits a pattern of high negative to high positive anisotropy as the nuclear envelope is traversed. This pattern is the signature of restricted rotational motion of fluorophores oriented in membranes, and it is very similar to images acquired by Axelrod and Blackman *et al.* in erythrocyte ghosts [9, 10]. We interpret this pattern as originating from
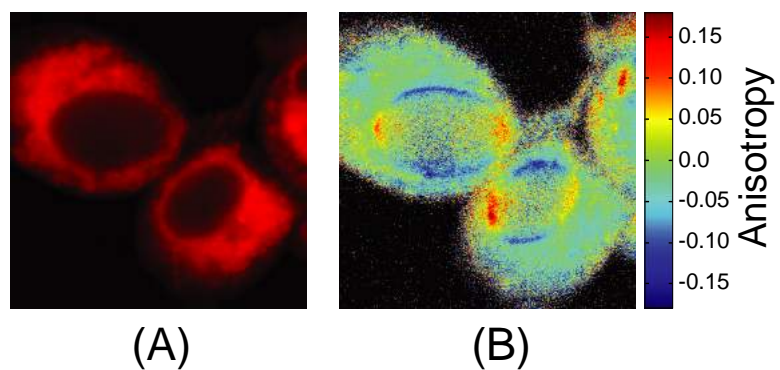
Figure 6.2: Anisotropy image of an EMT6 cell monolayer incubated with 5 μg/ml mTHPC for 24 hours. A conventional confocal fluorescence image of the drug localization in viable cells is shown in A. The anisotropy map computed from the polarization-sensitive images shown in B is consistent with the orientation of dye in the nuclear envelope. Images are 40×40 μm.

mTHPC molecules orienting in the nuclear envelope, a conclusion that could not be drawn from the intensity image alone.

Future studies are necessary to determine if this property is unique to mTHPC or if it occurs in other sensitizers as well. It will also be interesting to determine if other properties of PDT agents are accessible from the magnitude of the measured anisotropy.

6.3 Enzyme activity imaging: future directions

Specific construct design

In Chapter 5 proof-of-principle experiments were shown demonstrating the ability of confocal fluorescence polarization microscopy to image enzyme activity through the use of fluorescently-labeled constructs. Bodipy labeled bovine serum albumin (BSA) was used as the substrate in these studies because of the commercial availability of Bodipy-BSA and the fact that Bodipy is particularly insensitive to environmental changes that complicate polarization measurements [11]. BSA is not a particularly compelling substrate for general use, however, as it is cleaved by a host of enzymes at numerous locations. It is therefore advantageous to have a probe that is specific for a particular enzyme of interest.

We have undertaken the task of developing specific constructs in collaboration with Dr. Samuel Achilefu at Washington University. The first such construct is based upon the amino acid sequence that is the substrate for prostate specific antigen (PSA), namely Ala-His-Ser-Lys-Leu-Gln-Gly [12]. The current implementation of the construct design attaches Bodipy-FL to a polyamidoamine (PAMAM)

generation 5 dendrimer (Part number 53,670-9, Sigma-Aldrich, St. Louis, MO) with a linker that is the aforementioned sequence for PSA.

We anticipate that the action of PSA will yield a large decrease in anisotropy as the relatively small Bodipy-FL molecule (mol. wt. 292) is cleaved from the dendrimer (mol. wt. 28,825). From experiments with Bodipy-BSA in Chapter 5, we estimate the fundamental anisotropy of Bodipy-FL to be r_0=0.3 and τ_r for the free Bodipy to be approximately 200 ps. A rule of thumb for rotational correlation time of globular proteins is 1 ns for every 2,400 daltons of molecular weight [13]. Applying this approximation to our dendrimer construct yields τ_r=12 ns for our spherical generation 5 dendrimer. Through application of equation 1.17 we can estimate that the activity of PSA will yield a 20-fold decrease in anisotropy from 0.2 to 0.01. This assumes that the fluorescence lifetime of Bodipy does not change upon binding to the dendrimer, but our experience with BSA leads us to believe that a change may occur. If the lifetime of Bodipy decreases in the bound state, the pre-enzyme anisotropy will tend toward the r_0 value of 0.3 and will result in an amplification of the enzyme-induced anisotropy change.

Initial experiments will proceed in fluid solution in a fluorometer, and subsequent studies will be performed with images of cell monolayers. Eventually we anticipate implementing anisotropy imaging *in vivo* if the *in vitro* experiments are promising. Dendrimers have been shown to have many potential biological applications including drug delivery, as anti-viral and anti-bacterial agents, gene therapy, and PDT among others [14–16]. It is therefore possible that this dendrimer-based construct could be used in the future for *in vivo* studies.

It is also interesting to consider alternative methods for attaching the flu-

orophore to the dendrimer. The approach proposed above results in Bodipy molecules that are free to diffuse away from the dendrimer after the amino acid linker is cleaved. This can lead to problems acquiring sufficient signal in images as the cleaved product carrying information about the enzyme is rapidly lost to diffusion. A solution to this problem is to attach the fluorophore at two locations to the dendrimer. One of these linkers is a substrate for a particular enzyme, and the other linker is unaffected by the presence of enzyme. After the enzyme-specific linker is cleaved, the fluorophore is therefore still tethered to the large molecule but it yields a lower anisotropy as it experiences segmental motion about the remaining bond.

Anisotropy imaging of autofluorescence

The previous section and Chapter 5 were both devoted to enzyme imaging *via* application of exogenous enzyme-sensitive probes. This approach is very valuable and allows probing of specific enzyme activity, but there is an alternative strategy available to fluorescence polarization imaging that is not available with other techniques.

As discussed in section 5.1, metastasis involves classes of enzymes that act on the extracellular matrix, and molecular targets that yield information about their action are therefore potentially very powerful early diagnostic tools. Approaches taken thus far have concentrated on observing changes in exogenous probes as acted on by enzymes. Anisotropy imaging offers a potentially more powerful approach based on imaging the endogenous fluorescent substrates (extracellular matrix) targeted by these enzymes. Degradation of the extracellular matrix may

be visible in anisotropy images if the autofluorescence of the matrix is bright enough to yield useful images, and this therefore avoids the exogenous approach altogether.

Along these lines, we imaged a field from a freshly excised naïve mouse lung that was selected due to its inherently bright autofluorescence. The image acquired on our confocal microscope with 488 nm excitation light and a 500 nm long-pass filter is shown in Figure 6.3. It is apparent from the intensity and anisotropy images that the signal from fresh lung is bright and appears to follow the pattern expected from collagen in the extracellular matrix (Patricia Sime, personal communication). More importantly, the anisotropy in this matrix is quite high and is readily imaged. It is therefore possible that degradation of extracellular matrix components will lead to lower fluorescence anisotropies and this could therefore be an early reporter of metastasis. Further work to determine the feasibility of this approach is required, but it holds promise as a technique for mapping enzyme activity on the native substrate *in vivo*.
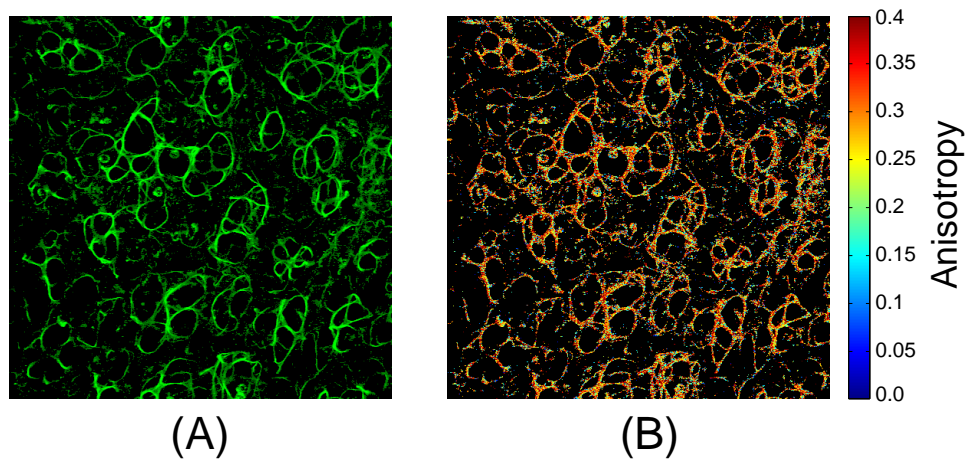
Figure 6.3: Conventional fluorescence image (A) and anisotropy image (B) of freshly excised mouse lung without any exogenous labeling. The fluorescence intensity is abundant with 488 nm excitation, and the fluorescence anisotropy in the bright extracellular matrix structures is quite high. Images are 500×500 μm fields of view acquired with the $10\times$, 0.45 NA objective and 488 nm excitation.

References

[1] A. Knight, N. Goddard, P. Fielden, M. Barker, N. Billinton, and R. Walmsley, "Fluorescence polarisation of green fluorescent protein (GFP). A strategy for improved wavelength discrimination for GFP determinations," Anal. Commun. **36,** 113–117 (1999).

[2] A. Knight, N. Goddard, N. Billinton, P. Cahill, and R. Walmsley, "Fluorescence polarization discriminates green fluorescent protein from interfering autofluorescence in a microplate assay for genotoxicity," J. Biochem. Biophys. Methods **51,** 165–177 (2002).

[3] R. Swaminathan, C. Hoang, and A. Verkman, "Photobleaching recovery and anisotropy decay of green fluorescent protein GFP-S65T in solution and cells: cytoplasmic viscosity probed by green fluorescent protein translational and rotational diffusion," Biophys. J. **72,** 1900–1907 (1997).

[4] L. Stryer, *Biochemistry*, 3rd ed. (W. H. Freeman and Company, New York, 1988).

[5] J. R. Lakowicz, I. Gryczynski, Z. Gryczynski, and J. D. Dattelbaum, "Anisotropy-based sensing with reference fluorophores," Anal. Biochem. **267,** 397–405 (1999).

[6] D. Kessel, "Correlation between subcellular localization and photodynamic efficacy," J. Photochem. Photobiol. B: Biol. (*in press*).

[7] V. O. Melnikova, L. N. Bezdetnaya, C. Bour, E. Festor, M.-P. Gramain, J.-L. Merlin, A. Y. Potapenko, and F. Guillemin, "Subcellular localization of meta-tetra(hydroxyphenyl) chlorin in human tumor cells subjected to photodynamic treatment," J. Photochem. Photobiol. B: Biol. **49,** 96–103 (1999).

[8] M.-H. Teiten, L. Bezdetnaya, P. Morlière, R. Santus, and F. Guillemin, "Endoplasmic reticulum and Golgi apparatus are the preferential sites of Foscan® localisation in cultured tumour cells," Br. J. Cancer **88,** 146–152 (2003).

[9] D. Axelrod, "Carbocyanine dye orientation in red cell membrane studied by microscopic fluorescence polarization," Biophys. J. **26,** 557–573 (1979).

[10] S. Blackman, C. Cobb, A. Beth, and D. Piston, "The orientation of eosin-5-maleimide on human erythrocyte band 3 measured by fluorescence polarization microscopy," Biophys. J. **71,** 194–208 (1996).

[11] I. Johnson, H. Kang, and R. Haugland, "Fluorescent membrane probes incorporating dipyrrometheneboron difluoride fluorophores," Anal.Biochem. **198,** 228–237 (1991).

[12] D. Patel, J. Frelinger, J. Goudsmit, and B. Kim, "*In vitro* assay for site-specific proteases using bead-attached GFP substrate," Biotechniques **31,** 1194–1203 (2001).

[13] C. R. Cantor and P. R. Schimmel, *Biophysical Chemistry Part II: Techniques for the study of biological structure and function* (W.H. Freeman and Company, New York, 1980).

[14] R. Esfand and D. A. Tomalia, "Poly(amidoamine) (PAMAM) dendrimers: from biomimicry to drug delivery and biomedical applications," Drug Discov. Today **6,** 427–436 (2001).

[15] M. J. Cloninger, "Biological applications of dendrimers," Curr. Opin. Chem. Biol. **6,** 742–748 (2002).

[16] U. Boas and P. M. H. Heegaard, "Dendrimers in drug research," Chem. Soc. Rev. **33,** 43–63 (2004).

Appendix A

Stokes Vectors

A.1   Stokes vector parameters

Stokes vectors are an effective approach to describing unpolarized, partially polarized, or completely polarized light. They are valuable because they can describe properties of unmeasurable electric fields in terms of experimentally accessible intensities. The Stokes vector, S, consists of four parameters, I, Q, U, and V arranged into a column such that

$$S = \begin{bmatrix} I \\ Q \\ U \\ V \end{bmatrix}. \tag{A.1}$$

In practice, the Stokes parameters can be determined with four measurements involving a linear polarizer and a quarter wave plate [1].

The explicit form of each parameter in equation A.1 is found from considering a plane wave incident on a detector. The electric field of the plane wave can be written as a superposition of two fields polarized along two orthogonal directions $\mathbf{e}_\parallel$ and $\mathbf{e}_\perp$ according to [2, section 2.11.1]

$$E\left(t\right) = E_\parallel \, \mathrm{e}^{-i(\omega t - kz)} \, \mathbf{e}_\parallel + E_\perp \mathrm{e}^{-i(\omega t - kz)} \, \mathbf{e}_\perp, \tag{A.2}$$

where

$$E_\parallel = a_\parallel e^{-i\delta_\parallel} \qquad \text{and} \qquad E_\perp = a_\perp e^{-i\delta_\perp}. \tag{A.3}$$

In equation A.3 the δ variables represent the phase of each component and the a values are electric field amplitudes.

I and Q are determined by measuring two intensities through a linear polarizer oriented along the basis vectors $\mathbf{e}_\parallel$ and $\mathbf{e}_\perp$. I is the total intensity of the wave given by

$$I = E_\parallel E_\parallel^* + E_\perp E_\perp^* = I_\parallel + I_\perp = a_\parallel^2 + a_\perp^2, \tag{A.4}$$

where $I_\parallel$ and $I_\perp$ are the intensities measured with the polarizer oriented along $\mathbf{e}_\parallel$ and $\mathbf{e}_\perp$, respectively. Q derives from the same measurements as I, but it is determined by the difference between the two intensities, namely

$$Q = E_\parallel E_\parallel^* - E_\perp E_\perp^* = I_\parallel - I_\perp = a_\parallel^2 - a_\perp^2, \tag{A.5}$$

U also arises from linear polarization measurements, but in this case the polarizer is oriented along axes rotated $+45°$ ($\mathbf{e}_+$) or $-45°$ ($\mathbf{e}_-$) with respect to $\mathbf{e}_\parallel$.

From these two measurements, U is calculated with

$$U = E_\parallel E_\perp^* + E_\perp E_\parallel^* = I_+ - I_- = 2a_\parallel a_\perp \cos \delta, \qquad \text{(A.6)}$$

where $\delta = \delta_\parallel - \delta_\perp$ and I_+ and I_- are the intensities measured along $\mathbf{e}_+$ and $\mathbf{e}_-$.

Determination of V differs from the other parameters in that it relies on decomposing the plane wave into left and right circularly polarized light rather than two orthogonal linear polarizations. The corresponding right and left basis vectors are $\mathbf{e}_R$ and $\mathbf{e}_L$, respectively, and with these V is calculated according to

$$V = i \left(E_\parallel E_\perp^* + E_\perp E_\parallel^* \right) = I_R - I_L = 2a_\parallel a_\perp \sin \delta. \qquad \text{(A.7)}$$

Table A.1 contains Stokes vectors for several of the most basic polarization states derived from equations A.4-A.7.

S	Linear polarization				Circular polarization	
	$\rightarrow$ (0°)	$\uparrow$ (90°)	$\searrow$ (+45°)	$\nearrow$ (−45°)	$\circlearrowright$ (right)	$\circlearrowleft$ (left)
I	1	1	1	1	1	1
Q	1	-1	0	0	0	0
U	0	0	1	-1	0	0
V	0	0	0	0	1	-1

Table A.1: Stokes vectors for selected polarization states.

References

[1] E. Collett, *Polarized light: Fundamentals and applications* (Marcel Dekker, New York, 1993).

[2] C. F. Bohren and D. R. Huffman, *Absorption and scattering of light by small particles* (Wiley Interscience, New York, 1983).

Appendix B

Special Cases for Mueller Matrices at Interfaces

Equations 3.12-3.14 represent the general case for light incident on a dielectric interface. Normal incidence and total internal reflection are two special cases for which simplifications can be made that speed up computation.

B.1   Normal incidence

For normal incidence, small angle approximations for the terms in M_r and M_t as well as Snell's law yield [1]

$$
M_r = \left(\frac{n_t - n_i}{n_t + n_i} \right)^2
\begin{bmatrix}
1 & 0 & 0 & 0 \\
0 & 1 & 0 & 0 \\
0 & 0 & -1 & 0 \\
0 & 0 & 0 & -1
\end{bmatrix}
\tag{B.1}
$$

and

$$M_t = \frac{n_t}{n_i} \frac{4}{\left(\frac{n_t}{n_i} + 1\right)^2} \begin{bmatrix} 1 & 0 & 0 & 0 \\ 0 & 1 & 0 & 0 \\ 0 & 0 & 1 & 0 \\ 0 & 0 & 0 & 1 \end{bmatrix}. \tag{B.2}$$

B.2   Total internal reflection

In cases where the incident angle exceeds the critical angle, a Mueller matrix for total internal reflection (TIR) must be applied. This situation occurs most often at the glass-air interface for the coverslip, but it also occurs in other regions where the refractive index increases across a boundary (in the fluorescent bar of Chapters 2 and 4, for example). The Mueller matrix for total internal reflection is [1]

$$M_{TIR} = \begin{bmatrix} 1 & 0 & 0 & 0 \\ 0 & 1 & 0 & 0 \\ 0 & 0 & \cos\delta & -\sin\delta \\ 0 & 0 & \sin\delta & \cos\delta \end{bmatrix}, \tag{B.3}$$

where δ is given by

$$\delta = 2\tan^{-1}\left(-\frac{\eta\cos\theta_i\sqrt{\frac{\sin^2\theta_i}{\eta^2} - 1}}{\sin^2\theta_i}\right). \tag{B.4}$$

References

[1] E. Collett, *Polarized light: Fundamentals and applications* (Marcel Dekker, New York, 1993).